


2012

High Speed Flow Simulation in Fuel Injector Nozzles

Sukanta Rakshit

University of Massachusetts Amherst, sukanta.svnit@gmail.com

Follow this and additional works at: <http://scholarworks.umass.edu/theses>

 Part of the [Aerodynamics and Fluid Mechanics Commons](#), [Computational Engineering Commons](#), [Heat Transfer, Combustion Commons](#), [Petroleum Engineering Commons](#), [Propulsion and Power Commons](#), and the [Thermodynamics Commons](#)

Rakshit, Sukanta, "High Speed Flow Simulation in Fuel Injector Nozzles" (2012). *Masters Theses 1911 - February 2014*. 942.
<http://scholarworks.umass.edu/theses/942>

This thesis is brought to you for free and open access by the Dissertations and Theses at ScholarWorks@UMass Amherst. It has been accepted for inclusion in Masters Theses 1911 - February 2014 by an authorized administrator of ScholarWorks@UMass Amherst. For more information, please contact scholarworks@library.umass.edu.

**HIGH SPEED FLOW SIMULATION IN FUEL INJECTOR
NOZZLES**

A Thesis Presented

By

Sukanta Rakshit

Submitted to the Graduate School of the
University of Massachusetts Amherst in partial fulfillment
of the requirements for the degree of
MASTER OF SCIENCE IN MECHANICAL ENGINEERING

September 2012

Mechanical and Industrial Engineering

© Copyright by Sukanta Rakshit 2012

All Rights Reserved

HIGH SPEED FLOW SIMULATION IN FUEL INJECTOR

NOZZLES

A thesis presented

By

Sukanta Rakshit

Approved as to style and content by:

David P. Schmidt, Chair

Blair Perot, Member

Surita Bhatia, Member

David P. Schmidt, Graduate Program Director

Mechanical & Industrial Engineering

ACKNOWLEDGEMENTS

I would never have been able to finish my thesis without the guidance of my committee members, help from friends, and support from my family and wife.

I would like to express my deepest gratitude to my advisor, Dr. David P. Schmidt, for his excellent guidance, caring, patience, and providing me with an excellent atmosphere for doing research. His knowledge in fuel injector nozzles and cavitation has been extremely beneficial for me. I would also like to thank to Dr. Blair Perot and Dr. Surita Bhatia for serving on all my committees from thesis proposal to my final defense.

I would also like to thank to my parents, my elder sister, Snigdha and my fiancé, Molika. They were always supporting and encouraging me with their best wishes throughout my education. Special thanks to Shiva and Kshitij for their guidance and support as mentors. I would also thanks to my colleges Mike, Mihir, Kyle, Sandeep, Tom, Colarossi, Nat, Brad, Maija and Raghu for their help and support.

ABSTRACT

HIGH SPEED FLOW SIMULATION IN FUEL INJECTOR NOZZLES

SEPTEMBER 2012

SUKANTA RAKSHIT

B. TECH., SV NATIONAL INSTITUTE OF TECHNOLOGY, SURAT

M.S., UNIVERSTIY OF MASSACHUSETTS AMHERST

Directed by : Dr. David P. Schmidt

Atomization of fuel is essential in controlling combustion inside a direct injection engine. Controlling combustion helps in reducing emissions and boosting efficiency. Cavitation is one of the factors that significantly affect the nature of spray in a combustion chamber. Typical fuel injector nozzles are small and operate at a very high pressure, which limit the study of internal nozzle behavior. The time and length scales further limit the experimental study of a fuel injector nozzle. Simulating cavitation in a fuel injector will help in understanding the phenomenon and will assist in further development.

The construction of any simulation of cavitating injector nozzles begins with the fundamental assumptions of which phenomena will be included and which will be neglected. To date, there has been no consensus about whether it is acceptable to assume that small, high-speed cavitating nozzles are in thermal or inertial equilibrium. This diversity of opinions leads to a variety of modeling approaches. If one assumes that the nozzle is in thermal equilibrium, then there is presumably no significant delay

in bubble growth or collapse due to heat transfer. Heat transfer is infinitely fast and inertial effects limit phase change. The assumption of inertial equilibrium means that the two phases have negligible slip velocity. Alternatively, on the sub-grid scale level, one may also consider the possibility of small bubbles whose size responds to changes in pressure. Schmidt et al. [1,2] developed a two dimensional transient homogeneous equilibrium model which was intended for simulating a small, high speed nozzle flows. The HEM uses the assumption of thermal equilibrium to simulate cavitation. It assumes the two-phase flow inside a nozzle in homogeneous mixture of vapor and liquid. This work presents the simulation of high-speed nozzle, using the HEM for cavitation, in a multidimensional and parallel framework. The model is extended to simulate the non-linear effects of the pure phase in the flow and the numerical approach is modified to achieve stable result in multidimensional framework.

Two-dimensional validations have been presented with simulation of a venturi nozzle, a sharp nozzle and a throttle from Winklhofer et al. [3]. Three-dimensional validations have been presented with simulation of ‘spray A’ and ‘spray H’ injectors from the Engine Combustion Network [4]. The simulated results show that equilibrium assumptions are sufficient to predict the mass flow rate and cavitation incidence in small, high-speed nozzle flows.

TABLE OF CONTENTS

	Page
ACKNOWLEDGEMENTS	iv
ABSTRACT.....	v
TABLE OF CONTENTS.....	vii
LIST OF TABLES	ix
LIST OF FIGURES	x
LIST OF SYMBOLS	xiv
CHAPTER	
1. INTRODUCTION	1
Cavitation and its role in a fuel injector nozzle	2
Motivation.....	6
2. LITERATURE REVIEW	9
Cavitation in fuel injector nozzles	9
Cavitation number.....	14
Past Modeling Approaches	18
3. NUMERICAL METHODOLOGY.....	22
Governing equations	22
Cavitation model.....	22
Numerical approach	26
Boundary conditions	32

4. VALIDATION AND RESULTS: 2D INJECTORS	35
Flow through a venturi nozzle	36
Simulation of flow in high speed nozzles	42
Winklhofer experiments.....	56
5. VALIDATIONS AND RESULTS : ECN INJECTORS	64
Spray A Injector simulation	64
Spray H Injector simulation	75
6. CONCLUSIONS.....	83
Suggestions for future work.....	84
REFERENCES	86

LIST OF TABLES

	Page
Table 3-1 List of typical values of N	25
Table 3-2 Characteristics based on nature of the flow	34
Table 4-1 Properties of water at 308 K	38
Table 4-2 comparisons of the venturi results	41
Table 4-3 Properties of diesel used for the simulations	57
Table 5-1 Properties of n-dodecane at 363K used for simulation [73]	71
Table 5-2 Comparison of simulation result with experiments	73
Table 5-3 The fluid properties of n-Heptane at 373K [73]	78
Table 5-4 Mass flow rate and momentum flux for the simulated results.	81

LIST OF FIGURES

	Page
Figure 1-1 Streamlines at the inlet of a nozzle as shown by Payri et al [6].....	3
Figure 1-2 Boiling and cavitation explained in P-T diagram shown by Brenen et al.[7].	4
Figure 1-3 The schematic of fuel injector nozzles used by Kashiwaya et al.[8].	5
Figure 1-4 Schematic of a common rail fuel delivery system from Sato et al [10].	6
Figure 1-5 Jet breakup explained by Hiroyasu [11].....	7
Figure 2-1 Variations in velocity with pressure difference (solid line represents $C_d=1$, dotted line represents $C_d=0.7$) observed by Chaves et al[15].	10
Figure 2-2 Spray angles at various pressure difference observed by Chaves et al[16].	11
Figure 2-3 Schematic of a cavitating nozzle from Schmidt et al [22].	15
Figure 2-4 Cavitation numbers against the coefficient of discharge	16
Figure 2-5 Comparison of experimental result with Nurick’s theory	17
Figure 3-1 Flowchart for the MasCavFoam solver.....	31
Figure 4-1 The schematic of the 2-D axisymmetric venturi nozzle.....	37
Figure 4-2 The meshed geometry with around 25K cells	37
Figure 4-3 Velocity contour at 100 MPa exit pressure for the axisymmetric venturi with Minmod convective scheme.	39
Figure 4-4 Pressure and density variation for the axisymmetric venturi at 100 MPa downstream pressure with Minmod convective scheme	39

Figure 4-5 Compressibility variation for the axisymmetric venturi at 100 MPa downstream pressure with Minmod convective scheme.	40
Figure 4-6 Compressible pressure waves exiting the domain at 100 MPa downstream pressure.....	40
Figure 4-7 Velocity comparisons with the theoretical velocity at various pressure differences.....	41
Figure 4-8 Schematic of the 2-D axisymmetric nozzle	42
Figure 4-9 Meshed geometry of the 2-D axisymmetric nozzle.	43
Figure 4-10 Pressure plotted against density in the two phase regions for water	44
Figure 4-11 Variation of the acoustic speed in water using HEM.....	45
Figure 4-12 Velocity streamlines for $K = 1.05$ at the sharp inlet for the axisymmetric nozzles with Minmod convective scheme and k- turbulence model.....	46
Figure 4-13 Velocity streamlines for $K = 1.05$ at the exit for the axisymmetric nozzles with Minmod convective scheme and k- turbulence model.....	47
Figure 4-14 pressure and density contours at $K=1.05$ for the axisymmetric nozzle with Minmod convective scheme and k- turbulence model.	48
Figure 4-15 Turbulent kinetic energy and void fraction contours at $K = 1.05$ for the axisymmetric nozzle with Minmod convective scheme and k- turbulence model.....	49
Figure 4-16 Velocity and compressibility at $K=1.05$ for the axisymmetric nozzles with Minmod convective scheme and k- turbulence model.....	49
Figure 4-17 densities and void fraction at $K=1.25$ for the axisymmetric nozzle with Minmod convective scheme and k- turbulence model.....	50

Figure 4-18 Streamlines for non-cavitating nozzle flow at $K = 2$ showing no separation at near the wall.....	51
Figure 4-19 Pressure and density contour at $K=2$ for the axisymmetric nozzles with Minmod convective scheme and $k-$ turbulence model.....	52
Figure 4-20 The turbulence kinetic energy for the cavitating ($K=1.1$) and non-cavitating nozzle ($K=2$) for the axisymmetric nozzles with Minmod convective scheme and $k-$ turbulence model.....	52
Figure 4-21 Cavitation number (K) vs. discharge coefficient (C_d).....	54
Figure 4-22 Velocity streamlines superimposed over the void fraction	55
Figure 4-23 Void fraction vs. radial distance at $K=1.1$ for the axisymmetric nozzle with Minmod convective scheme and $k-$ turbulence model.at $x=50 \mu\text{m}$	56
Figure 4-24 Experimental Geometry from Winklhofer et al. [55].....	58
Figure 4-25 The meshed geometry with 76000 quad cells.	58
Figure 4-26 Comparison of numerical mass flow rate with experiments	59
Figure 4-27 Comparison of vapor generation at 8.5 MPa	60
Figure 4-28 Cavitation prediction at the critical cavitation pressure	61
Figure 4-29 Comparison of velocity at 53 μm from the nozzle inlet.....	62
Figure 4-30 Comparison of pressure contour at 3.1 MPa (top) and 4.2 MPa (bottom) downstream pressure.....	63
Figure 5-1 Exit profile of the Injector 210675 matched with the measurement from ECN [4]	65
Figure 5-2 X-ray tomography image of Injector 210675 obtained from the ECN website [4].....	66

Figure 5-3 Internal shape of the nozzle has been extracted through silicone molds and SEM imaging from Macian et al [77].....	68
Figure 5-4 Sectional view of the inlet of the nozzle in the YZ plane	68
Figure 5-5 Sectional view of the CAD model generated in the YZ Plane.....	69
Figure 5-6 Sectional view of the nozzle in XY Plane.....	70
Figure 5-7 Velocity and pressure contour for spray A simulation with Minmod convective scheme and k- turbulence model.....	72
Figure 5-8 Density and compressibility contours at spray A condition with Minmod convective scheme and k- turbulence model.....	74
Figure 5-9 Geometry of the nozzle for spray H case from ECN Website [81]	75
Figure 5-10 Variation of diameter along the length of the nozzle shown by Pickett et al [81].	76
Figure 5-11 Outline of the spray H nozzle with boundaries	77
Figure 5-12 Sectional view of the inlet of the nozzle in the YZ plane	77
Figure 5-13 Streamlines showing the formation of separation at the inlet.....	79
Figure 5-14 Sectional view of the velocity and the density contour for spray H nozzle with Minmod convective scheme and k- turbulence model.	80
Figure 5-15 The pressure and the compressibility contour for spray H nozzle with Minmod convective scheme and k- turbulence model.....	80
Figure 5-16 Comparison of the density contour with $r = 20 \mu\text{m}$ on left half and r $=10 \mu\text{m}$ on the right half of the axisymmetric analysis.	82

LIST OF SYMBOLS

Symbol		
...	=	Density
P	=	Pressure
U_b	=	Bernoulli velocity
C_d	=	Coefficient of discharge
C_a	=	Area coefficient
C_v	=	Velocity coefficient
K, K_2, K_3	=	Cavitation number
Re	=	Reynolds number
P_1	=	Upstream pressure
P_2	=	Downstream pressure
P_v	=	Vapor pressure
U	=	Velocity
C_c	=	Contraction coefficient
A	=	Nozzle cross sectional area
A_c	=	Cross-sectional area at the vena contracta
A_{eff}	=	Effective area for flow after cavitation
	=	Constant with value 3.14159265
t	=	Time scale
μ	=	Dynamic viscosity
a	=	Velocity of sound

a_l	=	Velocity of sound in liquid
a_g	=	Velocity of sound in vapor
ρ_l	=	Saturated liquid density
ρ_g	=	Saturated vapor density
α	=	Void fraction
P_l^{sat}	=	Saturated liquid pressure
$\{v$	=	Volumetric flux
$\{$	=	Mass flux
$\tilde{\nu}_v$	=	Dynamic viscosity of vapor
$\tilde{\nu}_l$	=	Dynamic viscosity of liquid
	=	Compressibility
ν	=	Compressibility of vapor
ν_l	=	Compressibility of liquid
\dot{m}	=	Mass flow rate
\dot{M}	=	Momentum flux
D	=	Diameter of the nozzle
R	=	Radius of the nozzle
L	=	Length of the nozzle
r	=	Inlet radius of the nozzle

CHAPTER 1

INTRODUCTION

Combustion of gasoline and diesel fuel emits harmful gases and particles. The harmful gases and particles emitted from the combustion of these fuels are nitrogen oxide (NO_x), carbon monoxide (CO), hydrocarbons (HC) and particulate matter (PM). Administrations all over the world, through more stringent emission standards, are keeping check on the emission parameters. Many emission standards are in use worldwide (for example, Euro V in European nations (EU) and many Asian countries). The United States government also mandated a Tier 4 standard on all on-highway diesel engines, which limit emissions to a threshold of 0.2 g/kWh NO_x , 0.01 g/kWh PM and 0.14 g/kWh non-methane hydrocarbons (NHMC) [5] for 2007 and later models. In the future, introduction of a stricter standard is probable, and to meet the current and future demand, lowering of engine emissions will be required. Combustion of fuel is one of the factors affecting the emissions and developing more efficient fuel injection and engine control system can be beneficial in lowering the engine emissions.

One of the emission control strategy is to reduce the production of in-cylinder pollutants. One of the ways to reduce the production of pollutants in the cylinder is improving the combustion process. The combustion process in the cylinder can be linked with the internal nozzle flow and the atomization. In a fuel injector nozzle, atomization of fuel takes place downstream of the nozzle. The atomized spray disintegrates the liquid fuel into tiny droplets, providing more surface area of fuel per unit volume. This process helps in the rapid mixing of the fuel with the air. Moreover, controlling atomization can maintain an optimum level of fuel/air mixture needed for

the combustion. For example, when the quantity of air is less than the required amount, incomplete combustion takes place. This increases the amount of carbon monoxide and unused hydrocarbons after the process. Conversely, when the quantity of air is more than the required amount, nitrogen present in the air reacts with the excess oxygen. This reaction due to excess air increases the amount of NO_x in the emissions. Hence, controlling the mixture of injected fuel and air in the cylinder is essential to optimize the process. In addition, the time scale of combustion inside the internal combustion engine is very small. Mixing of the fuel with air must be very fast for efficient combustion. Proper control in atomization can optimize this mixing process and aid in better combustion of fuel. Optimized injection process benefits the engine with reduced emissions and increased efficiency. Various characteristics affect the flow downstream of the nozzle such as injection properties, geometry of the nozzle and the fuel properties. Further study of the internal nozzle flow characteristics will be helpful in understanding atomization and controlling the combustion process.

Cavitation and its role in a fuel injector nozzle

Cavitation is a phenomenon that occurs when the pressure inside a nozzle falls below the saturated vapor pressure of a liquid. This transition from liquid to vapor occurs at a constant temperature. A similar transition from liquid to vapor occurs at a constant pressure and termed as boiling (See Figure 1-2).

In a fuel injector nozzle, cavitation is generally induced by an abrupt change in the geometry inside the nozzle that makes the pressure fall below the saturated pressure. Typical fuel injectors are small, and their primary role is to inject the fuel in the combustion chamber in a controlled manner. Due to a sudden contraction at the inlet of the nozzle, a boundary layer tends to separate and a re-circulation appears

with a fall in pressure (see Figure 1-1). When the pressure in this region falls below the saturated pressure of the fuel, the phase transition is termed cavitation. Due to the separation at the inlet, a vena contracta is formed. This reduces the area available for the flow. The reduction in area leads to an increase in velocity at the inlet. The increase in velocity inside the fuel injector nozzle benefits the downstream atomization, which enhances the quality of the fuel/air mixture available for combustion inside the cylinder. Cavitation in a fuel injector nozzle improves the atomization through primary break up, and subsequently improves the combustion of fuel, which reduces emissions. Better atomization facilitates reduction of hydrocarbon emissions and improves the engine efficiency.

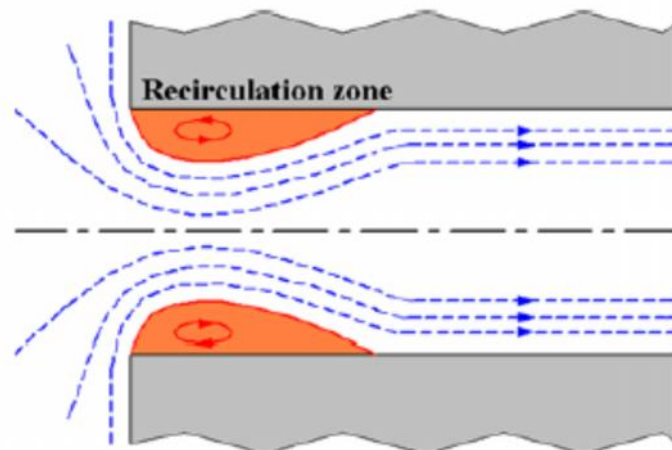


Figure 1-1 Streamlines at the inlet of a nozzle as shown by Payri et al [6].

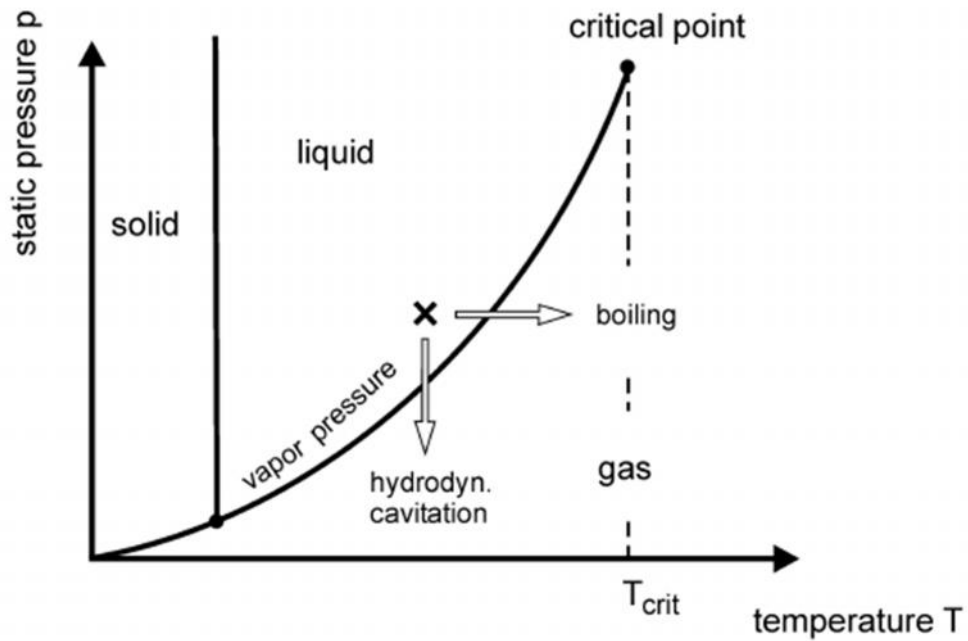


Figure 1-2 Boiling and cavitation explained in P-T diagram shown by Brennen et al.[7].

Many studies were conducted on the atomization of fuel and its effect on emissions and efficiency of engines. Among these, Kashiwaya et al. [8] performed a study on effects of atomization in a fuel injection system on the engine performance. In their work, they compared the atomization in swirl type injector with the conventional pintle type injector shown in the Figure 1-3. They used gasoline for their study and showed an improvement in atomization in swirl type injectors and also showed an 8% decrease in the fuel consumption rate in comparison with the conventional fuel injector.

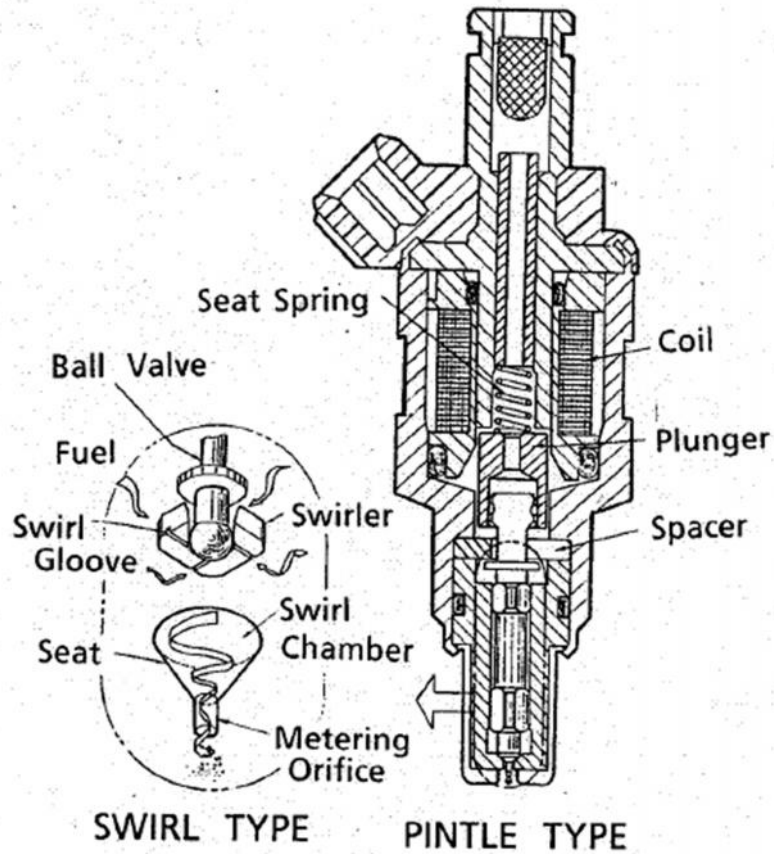


Figure 1-3 The schematic of fuel injector nozzles used by Kashiwaya et al.[8].

Another study in 1996 by Montgomery et al. [9] describes the relation between emissions and the spray characteristics. They also explored the effects of number of holes and hole size on the emissions and the performance of a direct injection diesel engine. In their work, they illustrated that the spray characteristics of a small size nozzle with fewer holes gave the best emissions performance and the second best brake specific fuel consumption for their configuration.

Direct injection fuel systems are very commonly used for diesel and gasoline engines. The direct injection fuel system works at a very high pressure and delivers the fuel at high velocity. In late 90's, Kato et al. [10] studied the behavior of a common rail diesel fuel injection system and the effects of high-pressure injection system on the emissions. The Figure 1-4 describes the schema of a common rail

injection system. In their study, they achieved a lower fuel consumption and smoke with a reduction in nozzle size. This configuration works well, but increases the injection period. Hence, it is necessary to increase the injection pressure to improve the performance of an engine.

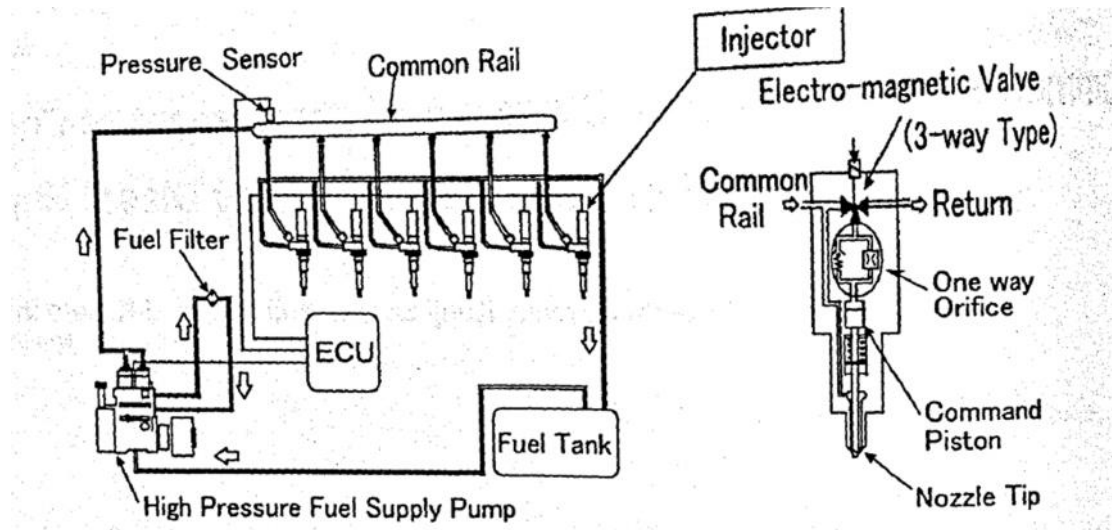


Figure 1-4 Schematic of a common rail fuel delivery system from Sato et al [10].

Motivation

The experimental works by Kashiwaya et al. [8] and Montgomery et al. [9] showed the effect of atomization and small nozzle size on the performance of engines. Kato et al. [10] showed the effect of injection pressure in common rail injection system and its effects on the performance of engines. At high injection pressures, the downstream jet velocity is very high. The studies performed by Hiroyasu [11] also explained the jet break up associated with the high jet velocity. The Figure 1-5 explains the spray behavior at varying velocities.

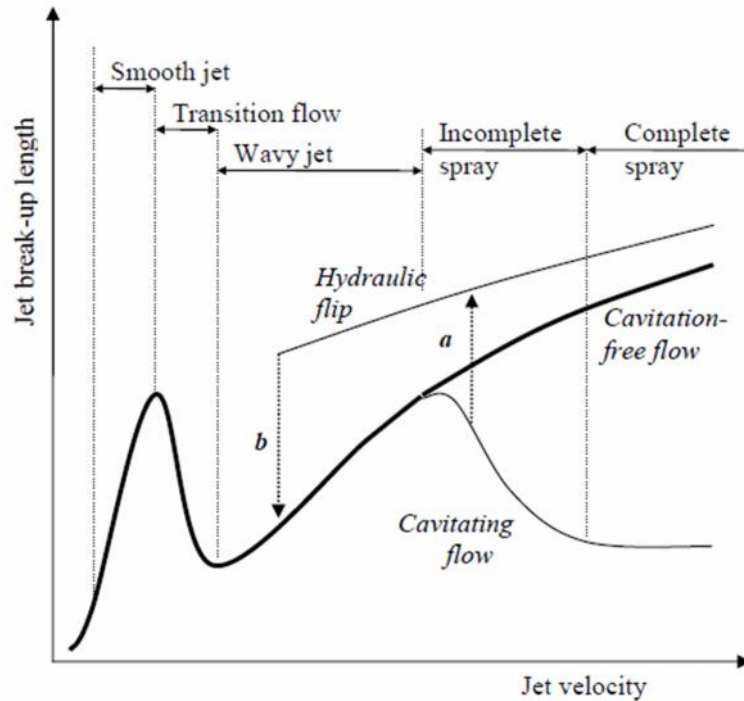


Figure 1-5 Jet breakup explained by Hiroyasu [11].

The small size, high speed and a limited time scale makes it very difficult to study the behavior experimentally. Modeling cavitation can be helpful in simulating flow in real size injector nozzles and studying the internal nozzle characteristics, which affect the flow inside a nozzle.

The construction of any simulation of cavitating injector nozzles begins with the fundamental assumptions of which phenomenon to include and which will be neglected [12]. To date, there has been no consensus about whether it is acceptable to assume that small, high-speed cavitating nozzles are in thermal or inertial equilibrium. If one assumes that the nozzle is in thermal equilibrium, then there is presumably no significant delay in bubble growth or collapse due to heat transfer. Heat transfer is infinitely fast and inertial effects limit phase change. The assumption of inertial equilibrium means that the two phases have negligible slip velocity. Alternatively, on the sub-grid scale level, one may also consider the possibility of small bubbles whose

size respond to changes in pressure. This diversity of opinions leads to a variety of modeling approaches. Simulations of cavitating atomizer nozzles invariably require simplifying assumptions. These assumptions should be sufficient to render the problem tractable without producing unacceptable errors. The objective of this work is to construct a three-dimensional CFD solver to simulate flow in a small, high-speed cavitating nozzle using the homogeneous equilibrium model (HEM). The HEM used in this work extends the model described by Schmidt et al. [1,2] in a multidimensional and parallelized framework. The model is extended to simulate the non-linear effects of the pure phase in the flow and the numerical approach differs from the work by Schmidt et al.

CHAPTER 2

LITERATURE REVIEW

Cavitation in fuel injector nozzles

There are various experimental studies related to cavitation in fuel injector. In 1959, Bergwerk [13] performed one of the early observations of cavitation in fuel injector nozzle. He studied the flow in a spray hole similar in size to a real fuel injector. In his work, he related the flow through the spray hole with the influence of cavitation number, Reynolds number, upstream edge sharpness and the length to diameter ratio (L/D) and demonstrated the presence of cavitation inside the nozzle. He further mentioned flow sensitivity due to imperfections in the nozzle geometry. Decades later, Bode et al. [14] performed another study on flow through a real size transparent nozzle. Although the pressure conditions were less than real injector conditions, they observed a cavitation film appearing at the inlet corner as they increased the pressure difference. They observed bubbles collapsing outside the nozzle, as at high velocities the bubble transit time through the nozzle is smaller than the bubble collapse time. They further observed a change in cavitation inception with the change in upstream pressure. Chaves et al. [15,16] later extended this work. They used a steady flow rig with the inlet pressure varying up to 100 MPa, and the back pressure was kept at 0.1 MPa (atmospheric pressure). Parameters used by them were similar to the actual fuel injector nozzles. In their work, they showed the closeness of flow velocity and the Bernoulli velocity represented by the Equation 2.1. The Figure 2-1 demonstrates the centerline velocity plotted against the difference between upstream and downstream pressure. The dotted line represents the discharge coefficient (C_d) = 0.7 and the solid line represents $C_d=1$ (or U_b) [15]. The circle in the

figure represents the correlation measurement value and the triangle represents the discharge measurement.

$$U_b = \sqrt{\frac{2\Delta P}{\dots}} \quad 2.1$$

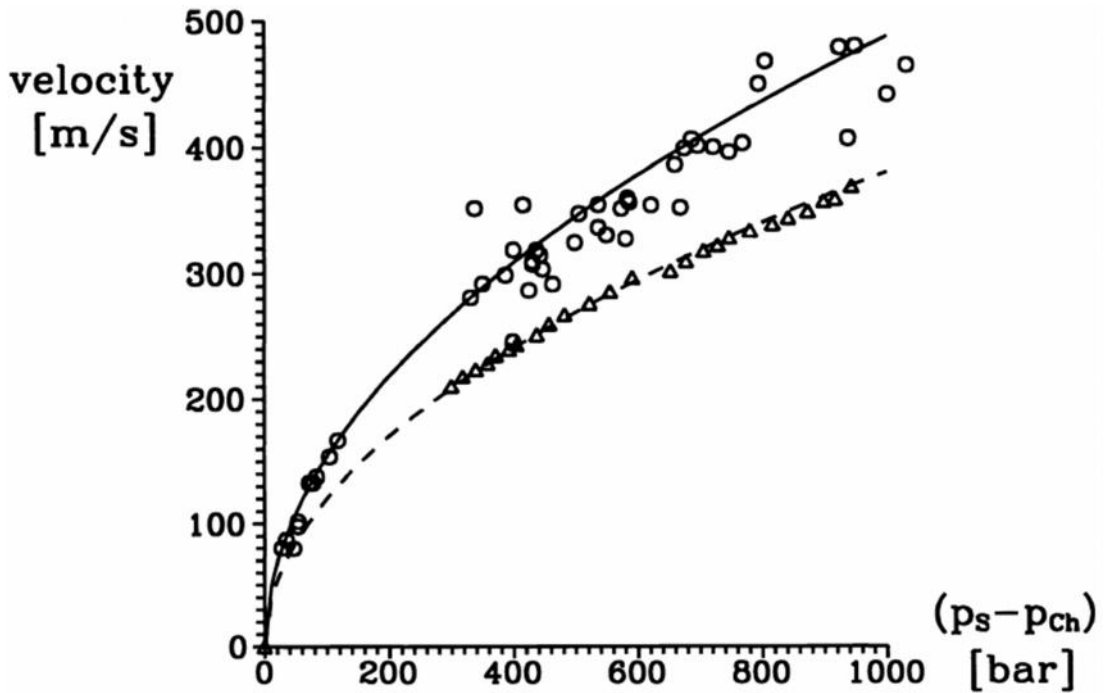


Figure 2-1 Variations in velocity with pressure difference (solid line represents $C_d=1$, dotted line represents $C_d=0.7$) observed by Chaves et al[15].

In their study, they described the phenomenon of cavities moving past the exit of the nozzle as “supercavitation”. After this condition, the discharge coefficient and the spray angle become independent of any further increase in injection pressure. Surprisingly the coefficient remains same for both short and long nozzles, although they observed a low velocity and lesser spray angle for the long nozzles [16]. The Figure 2-2 explains the increase in spray angle with the increase in pressure difference. However, after transition to the supercavitation phase, the increase in spray angle is small. In their work, they further concluded that the actual nozzle area

of the flow is not the geometric area. Their finding leads to a higher velocity and momentum prediction, which should be accounted for spray momentum and its effect on spray penetration.

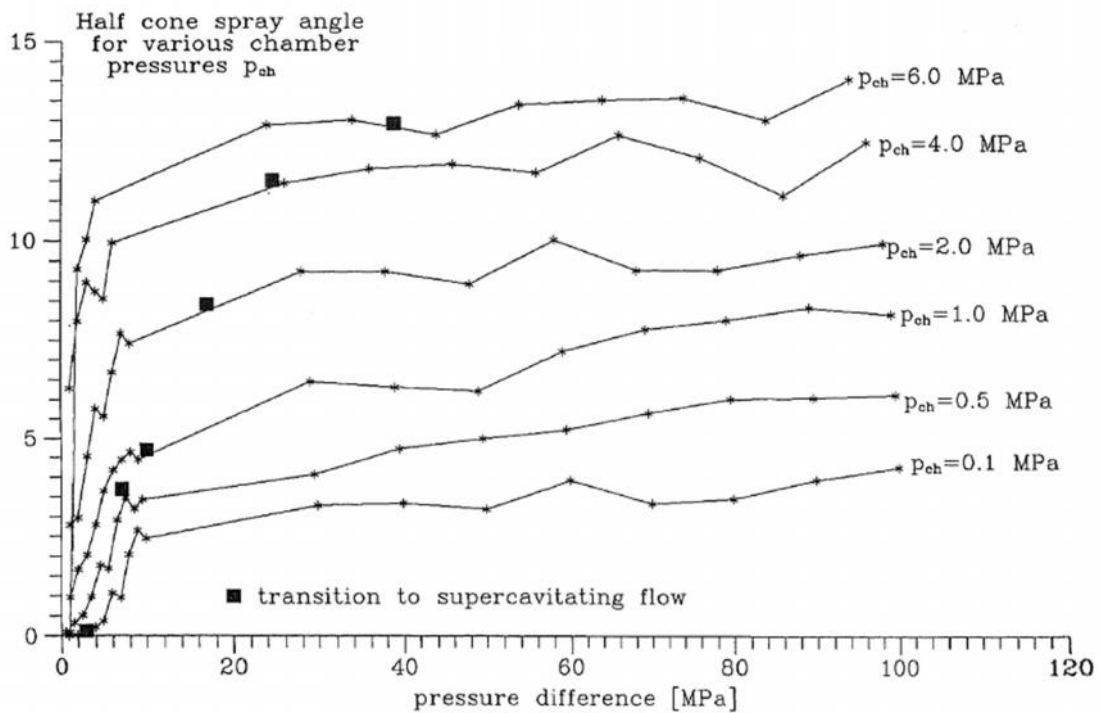


Figure 2-2 Spray angles at various pressure difference observed by Chaves et al[16].

Soteriou et al. [17-19] investigated the flow through a direct injection nozzle using a large-scale acrylic model. They showed the formation of cavitation bubbles in the nozzle in the form of a cloud. They also observed that under the influence of cavitation, coefficient of discharge was independent of Reynolds number but varied with the cavitation number. The trend of the variation remains the same even though the geometry or the size was changed. Soteriou et al. also observed hydraulic flip in the real and large-scale injector nozzle. Hydraulic flip occurs when the recirculation zone extends downstream of the orifice. When this recirculation zone reaches the

downstream corner, it merges with the entrained flow outside of the orifice, causing the air to enter and fill the recirculating region. However, in the real size injectors they observed what they called ‘imperfect hydraulic flip’. They related the upstream geometry with the hydraulic flip. They observed that the absence of a needle in the injector resulted in hydraulic flip, as the absence of turbulence caused by the needle would lead to a flow path more streamlined upstream of the nozzle. Interestingly, they also mentioned that the spray produced by a single hole in sac-type nozzles, where they observed hydraulic flip, doesn’t represent those from a multi hole nozzle and using them to investigate a spray could produce misleading results.

Chaves et al. compared their own work with Soteriou et al.’s work on the large-scale nozzles. According to Chaves et al., it is unlikely to scale up the bubble collapse time to the transit time of the bubble through a nozzle. Bubble size is a small fraction compared to the nozzle size and scaling them for real injector is not possible. They also mentioned that the influence of cavitation on internal nozzle flow is quite different in real and scaled nozzle. With all these differences, the coefficient of discharge obtained by Soteriou et al. is independent of the scale of the model.

Badock et al. [20] performed a similar study on the real injector nozzle. In their work, they used a Bosch common rail system with the injector made up of Perspex. They applied a maximum rail pressure of 60 MPa, though most of the measurements were taken at 25 MPa to avoid damage to the acrylic injector. They observed the nozzle filled with liquid surrounded by a cavitating film. This observation was similar to the one made by Chaves et al., and they did not observe bubbles or foam as noted by Soteriou et al. in their study.

Another experimental study with a scaled-up fuel injector nozzle was performed by Arcoumanis et al. [21-23], in which a vortex formation was observed in a multi-hole nozzle inlet and a string like film (which they termed as ‘string cavitation’) appeared inside the nozzle sac. They observed the appearance of the string like film before the development of the cavitation inside the nozzle. They observed this phenomenon more frequently in the flow with a low nozzle lift. They also used laser Doppler velocimetry to measure the local mean velocity and the turbulent kinetic energy inside the nozzle. Once the flow was developed, separation of fluid flow was observed and the cavitation film appeared near the wall. Injection conditions used by them were scaled down as compared to the real injector conditions, but they had correlated them with the cavitation number and the Reynolds number. Later, Chaves et al. [24,25] also demonstrated the string cavitation inside the inlet chamber at a low needle lift and with an injection pressure around 5-6 MPa using a real size injector nozzle. Condition used in these nozzles were very low compared to the actual diesel injector, where the inlet pressure is over the range of 100-200 MPa.

As we have seen, Bergwerk, Chaves et al. and Badock et al.’s work showed film cavitation in the real size injector whereas results from Soteriou et al. reflect bubbles inside the scaled injector model and Arcoumanis et al. demonstrated string cavitation inside the enlarged nozzle. Though these experimental results provide substantial information toward understanding the cavitation inception in the injector nozzle, yet most of them were performed either on enlarged models or under pressure conditions much lower than the actual injector conditions. Visualizing high-speed flow inside a real injector nozzle remains a challenge for experimental. In addition to the ambiguity associated with the scaling, it is important to correlate all the result with either the Reynolds number or the cavitation number. Using these terms will be

helpful to relate these results more clearly to the actual conditions and beneficial in predicting the flow inside a real injector nozzle to improve the atomization. Bergwerk used the Reynolds number and the cavitation number for his correlation. Soteriou et al. demonstrated cavitation number a better way to understand the cavitation phenomenon inside the nozzle. Arcoumanis et al. also used the cavitation number for their result to relate it with the cavitation. The following section will provide more insight to relate these results with the cavitation number.

Cavitation number

It is important to correlate the results and develop an effective means to predict cavitation inception inside an injector. Under cavitating condition, the cavitation number proves to be a more useful tool than Reynolds number in relating the phenomenon with the discharge coefficient of a nozzle. The flow is more closely associate with the Reynolds number under non-cavitating conditions. Over the years, various cavitation numbers were used to correlate cavitation behavior. Nurick [26] developed a very useful relation, which explains the cavitation characteristic in terms of coefficient of discharge of the nozzle. He performed numerous experiments on circular and rectangular orifices with a varying length to diameter ratio, upstream and downstream conditions. His model collapsed the experimental data and produced an interesting conceptual view of the nozzle flow. The fundamental assumptions of his model are:

1. The flow of liquid separates off the corner and contracts to an area that is a fixed fraction of the nozzle cross-sectional area.
2. The liquid experiences no head losses between the upstream stagnation state and the contraction.

- The pressure at the contraction is equal to the vapor pressure of the fluid.

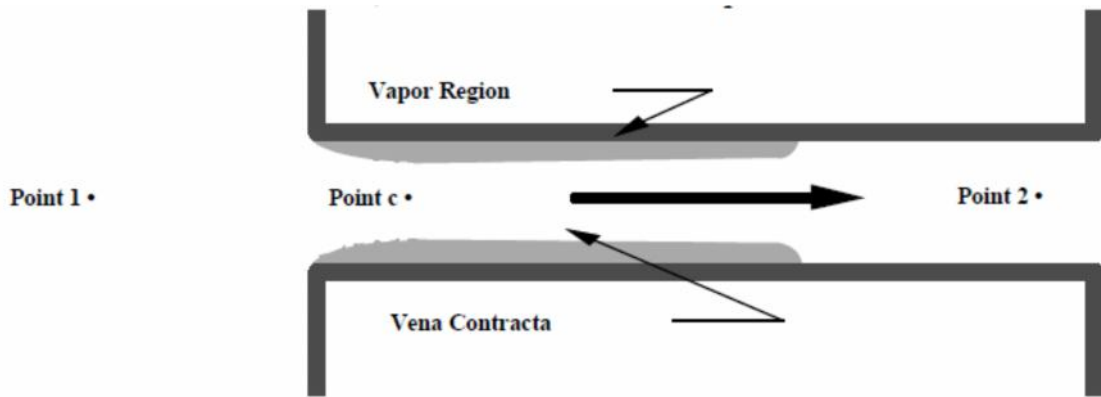


Figure 2-3 Schematic of a cavitating nozzle from Schmidt et al [22].

Cavitation number (K) suggested by Nurick is given by the Equation 2.2. Point 1 is the far upstream condition, point 2 denotes the downstream of the nozzle and point c denotes the narrowest point of contraction. P_v is the vapor pressure of the fluid. The cavitation number given by Nurick was later used by Lichtarowicz et al. [27], Payri et al. [6] and Stanley et al. [28]. Another variant, defined by the Equation 2.3 was used by Bergwerk [13], Soteriou et al. [17], Chaves et al. [24] and Baz et al. [29]. Another form of cavitation number (given by Equation 2.4), also used for cavitation in pumps and turbine, was used by Kobayashi et al. [30], Hiroyasu et al. [31], Sou et al. [32], Lee et al. [33] and Kim et al. [34].

$$K = \frac{P_1 - P_v}{P_1 - P_2} \quad 2.2$$

$$K_2 = \frac{P_1 - P_2}{P_2 - P_v} \quad 2.3$$

$$K_3 = \frac{P_2 - P_v}{\frac{1}{2} \rho U^2} \quad 2.4$$

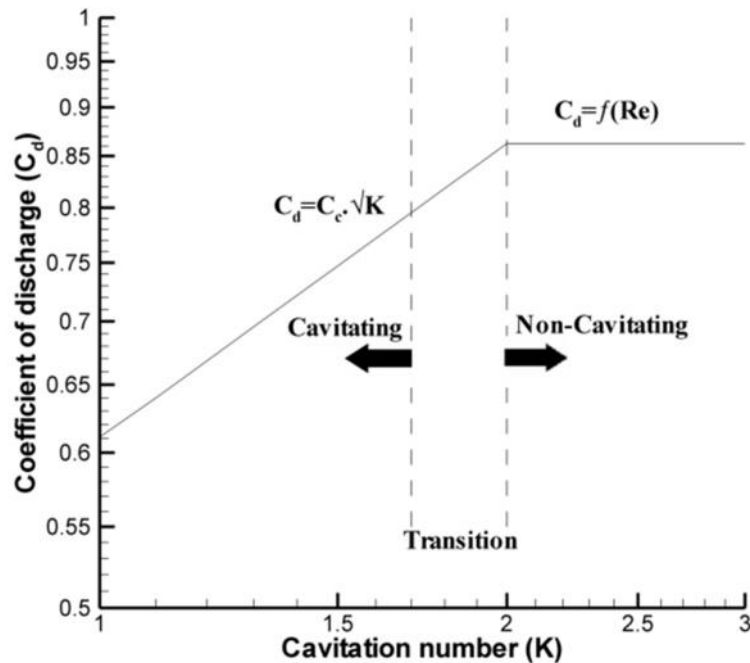


Figure 2-4 Cavitation numbers against the coefficient of discharge

In the Figure 2-4, the cavitation numbers are plotted against the discharge coefficient. The cavitating region is correlated by the Nurick's theory whereas the non-cavitating region is a function of Reynolds number. The transition of cavitating to non-cavitating phase varies with different nozzle sizes and different fluid properties. The transition of cavitating to non-cavitating regime occurs at lower cavitation number for the low temperature fluid than the higher. According to Nurick's study, the coefficient of discharge of a cavitating nozzle is directly proportional to the square root of the cavitation number (K) and is shown by the Equation 2.5. Here, C_c is the contraction coefficient of the nozzle at a point c which is calculated to be $1/(\sqrt{2} + 2)$ for

sharp nozzles. In the Figure 2-5, experimental data from various authors [13,18,21-23,33,35-38] were compared with the theory given by Nurick.

$$C_d = C_c \cdot \sqrt{K} \quad 2.5$$

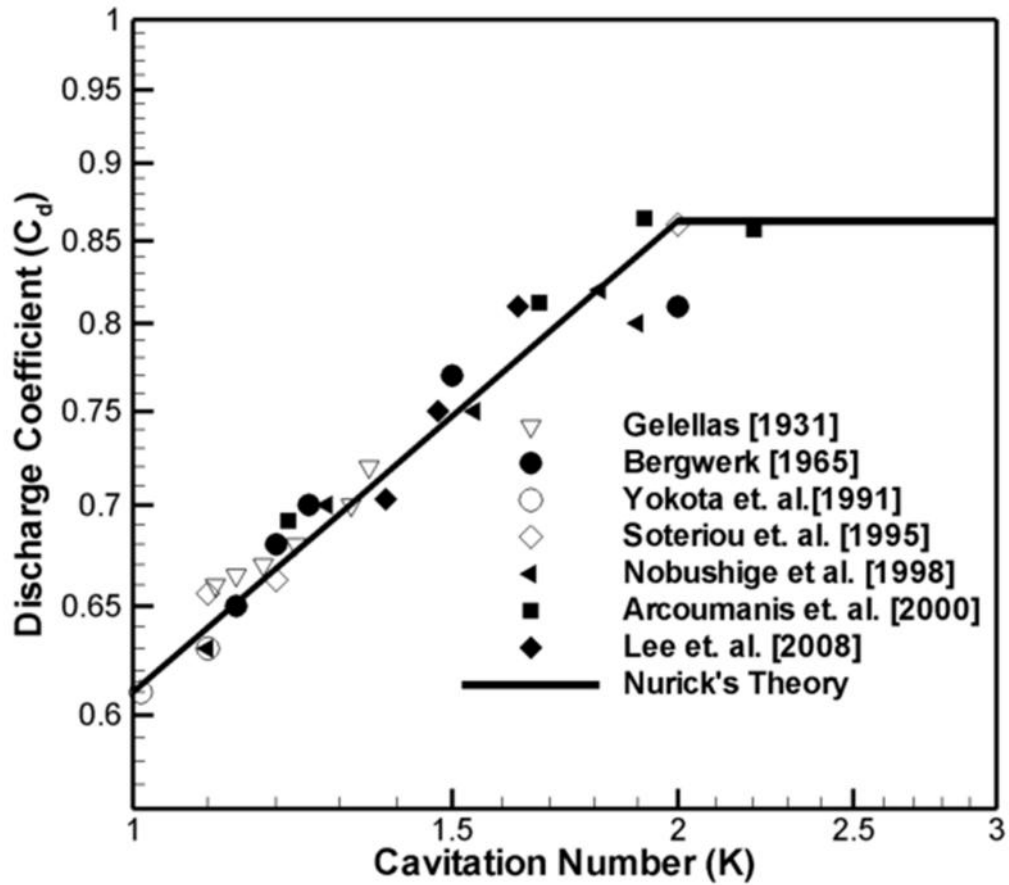


Figure 2-5 Comparison of experimental result with Nurick's theory

Past Modeling Approaches

Past efforts to model cavitating nozzles have taken different approaches with differing assumptions. One of the earliest approaches was to use the bubble dynamics equation. This was done by solving the Rayleigh-Plesset equation to get the necessary information for the growth and the destruction of the bubble. Kubota et al. [39] in their cavitation Bubble Two-phase fluid (BTF) Model assumed that the inside and outside of the cavity were a continuum. They also considered the cavity as a compressible viscous fluid whose density varied extremely. They illustrated the cavitating flow across the hydrofoil and explained the interactions between the vorticity shed at downstream and the bubbles. Using the model, the authors expressed the unsteady characteristics of cavitation and complicated interactions, particularly between the large-scale vortices and bubble dynamics.

Chen and Heister [40] used a similar kind of approach, where hydrodynamic non-equilibrium and bubble dynamics were the primary concern. Using their approach, they showed that earlier approach was valid only when the bubble radius is very small. When the bubble radius is comparable to the distance between the two bubbles, one cannot assume the local pressure as the far field pressure. Chen and Heister averaged the local pressure and solved the Rayleigh-Plesset equation for a finite domain. From this approach, they related the pseudo-density to the average pressure and void fraction from mass balance considerations.

Later Gavaises and Arcoumanis [41,42] in their work employed a Lagrangian model to represent the bubble growth. They extended the transport model to include the bubble breakup and related events. Alebjecvic [43] introduced cavitating flow using a two fluid model approach, with a continuous liquid and a dispersed vapor

phase. This model was based on the linearized Rayleigh-Plesset equation that was driven by the difference between hydrodynamic and vapor pressures. In his model, he also used an additional corrector term to account for turbulence pressure fluctuations. With this model, he evaluated important spray characteristics and cavitation flow in nozzles. Singhal et al. [44] later combined the Rayleigh-Plesset equation and the basic transport equation into a simplified mathematical equation. They referred to this as the reduced bubble dynamic formulation. They used this model to simulate cavitation on hydrofoils, submerged cylindrical bodies and the cavitation flow through an orifice.

Chen and Heister [45] also worked out a model where they treated mixtures of cavitation as two-phase mixtures, which they used for two-phase modeling. They solved the continuity equation postulating that the change in density must be related to the pressure difference $P - P_v$.

Schnerr et al. [46] also used the assumption of bubble growth as a closure to the basic governing equations to simulate cavitation in the fuel injector nozzle. They used a volume of fluid approach in combination with an additional model for growth and collapse of bubbles.

Avva et al. [47] introduced an enthalpy-based model for two-phase cavitation modeling which minimizes the need for empiricism. In this model, they assumed local thermodynamic equilibrium between the liquid and vapor phases, but allowed mechanical non-equilibrium such as unequal velocities or velocity. They formulated a single energy equation for a homogeneous mixture of gases, which compute the enthalpy as the dependent variable. The volume fraction and other thermodynamic properties were computed using the enthalpy.

In a third kind of approach, Delannoy and Kueny [48] employed a two phase modeling, where an equation of state is derived based on a barotropic model between pressure and density to predict the flow in a venturi. This model assumed thermodynamic as well as mechanical equilibrium between the two phases. They successfully demonstrated the qualitative behavior of the venturi but failed to predict the frequency of bubbles or the cavitation length. Schmidt et al.[1,2] later developed a two dimensional transient model which was intended for small, high speed nozzle flows, such as in diesel fuel injectors. This model also used a barotropic equation of state but included the compressibility of both the liquid and the vapor phase. The pressure-density relationship was derived by integrating the result of the Homogenous Equilibrium Model for the speed of sound. Habchi and Dumont [49,50] also used HEM to simulate the cavitating flow inside a diesel multi-hole injector. In their work, they successfully simulated a viscous, unsteady cavitating flow inside a diesel fuel injector. Lee and Reitz [51] applied the model from Schmidt et al. [1,2] in the KIVA-3V code to simulate the flow in a diesel injector nozzle. They also incorporated an injector needle movement using an arbitrary Lagrangian-Eulerian (ALE) approach. Karrholm et al. [52,53] used a similar approach to simulate the flow in a diesel fuel injector. Their assumptions are similar to the one made by Schmidt et al. but differ in the calculation of pressure. The latter used an implicit approach to solve the pressure equation rather than using an explicit equation derived by integrating the isentropic energy equation as in the former's approach. Catania et al. [54] later developed a barotropic model with a comprehensive thermodynamic approach.

Neroorker et al [55] worked out a fourth kind of approach with a non-equilibrium model to simulate the cavitation. They modeled the cavitation as flash boiling with rapid heat transfer between the liquid and the vapor phase. For a closure

to the basic conservation laws, the homogeneous relaxation model was used. This model describes the rate at which instantaneous quality tends towards the equilibrium quality. They used this approach to successfully simulate the flow in a fuel injector nozzle.

The main objective of this work is to simulate a high-speed fuel injector nozzle considering assumptions of hydrodynamic and thermal equilibrium. The two-dimensional HEM model (developed by Schmidt et al.) is applied in a multidimensional and a fully parallelized CFD code. The presence of a sharp gradient and high velocity inside the domain are challenges to constructing a stable coupling between the model and the basic conservative laws. Numerical methodology to deal with these sharp gradients plays an important role in the stability of the code. The numerical methodology used for implementing the model is explained in the following chapter.

CHAPTER 3

NUMERICAL METHODOLOGY

Governing equations

The homogeneous equilibrium model used in the current study works on the basic conservation laws. A single fluid approach is used by this model, which is governed by the conservation of mass and momentum. The Equation 3.1 represents the conservation of mass and the conservation of momentum is given by the Navier-Stokes equation (Equation 3.2). Only a second coefficient of viscosity is used for the simulations.

$$\frac{\partial \dots}{\partial t} + \nabla \dots \vec{U} = 0 \quad 3.1$$

$$\frac{\partial \dots \vec{U}}{\partial t} + \nabla \cdot (\dots \vec{U} \vec{U}) = -\nabla p + \vec{\nabla} \ddagger \quad 3.2$$

As a closure to these conservative laws, an equation of state for pressure is solved. The fluid inside the domain is assumed to be in a thermodynamic equilibrium and the effect of heat transfer due to bubble formation and collapse is neglected within the flow.

Cavitation model

Cavitation inside a fuel injector nozzle is a very fast and transient phenomenon. The heat transfer due to bubble growth and collapse can be neglected and the flow is assumed to be in thermal equilibrium. In this model, the two-phase flow inside the nozzle is assumed homogeneous mixture of vapor and liquid. The

barotropic equation of state used in the model, which is used to solve the pressure, includes the compressibility of both the liquid and the vapor phase. In this work, the pure phase flow is modeled with non-linear isentropic equations, instead of the one used by Schmidt et al and other researchers, to include the non-linear effect of the flow when phase change is not dominating. In a compressible flow, the isentropic speed of sound is represented by the following equation

$$Dp = a^2 D\rho \quad 3.3$$

where, a represents the velocity of sound for two phase flow and is provided by the equation given by Wallis[56] as

$$a = \sqrt{\frac{1}{\left(r \dots_g + (1-r) \dots_l \right) \left(\frac{r}{\dots_g a_g^2} + \frac{(1-r)}{\dots_l a_l^2} \right)}} \quad 3.4$$

where, a_l and a_g represents the speed of sound in liquid and vapor phase respectively. The void fraction is represented with r and given by the Equation 3.5.

$$r = \frac{\dots_g - \dots_l}{\dots_g - \dots_l} \quad 3.5$$

Considering a constant speed of sound for the saturated liquid and the saturated vapor phase, the pressure is analytically integrated using the Equation 3.3 as a function of void fraction. The two-phase pressure equation from the integration is represented as

$$p = p_l^{sat} + p_{gl} \log \left[\frac{\dots_g a_g^2 (\dots_l + r (\dots_g - \dots_l))}{\dots_l (\dots_g a_g^2 - r (\dots_g a_g^2 - \dots_l a_l^2))} \right] \quad 3.6$$

where, p_l^{sat} is the saturated pressure and p_{gl} is a function of the constant fluid parameters which are represented by the Equation 3.7.

$$p_{gl} = \frac{\dots_g a_g^2 \dots_l a_l^2 (\dots_g - \dots_l)}{\dots_g^2 a_g^2 - \dots_l^2 a_l^2} \quad 3.7$$

This means that no partial differential equation is required for the pressure. Instead, it is calculated using an analytical equation given by the Equation 3.6, 3.8 and 3.10. The equation 3.8 represents the Tait-Kirkwood [57] equation for isentropic flows which is used for modeling underwater explosions [57].

$$p = p_l^{sat} + \frac{B}{N} \left[\left(\frac{\dots}{\dots_l} \right)^N - 1 \right] \quad 3.8$$

where, B represents the isentropic bulk modulus and given by the Equation 3.9 and N represents the constant isentropic parameter of liquid.

$$B = \dots_l^{sat} a_l^2 \quad 3.9$$

The equation 3.9 represents the ideal gas law [58] for isentropic flows. In the Equation 3.9, \dots represents the ratio of specific heats for gas phase.

$$p = p_{vap} \left(\frac{\dots}{\dots_g} \right)^x \quad 3.10$$

where, the Equation 3.8 is valid for $\dots > \dots_l$, the Equation 3.10 is for $\dots < \dots_g$ and the Equation 3.6 is valid for $\dots_g > \dots < \dots_l$.

$$p_l^{sat} = p_{vap} - p_{gl} \log \left[\frac{\dots_g^2 a_g^2}{\dots_l^2 a_l^2} \right] \quad 3.11$$

Table 3-1 List of typical values of N

Liquid	N
Water	7
Diesel	11.1
Heptane	11.0
Dodecane	11.1

The saturated liquid pressure is calculated from simplifying the Equation 3.6 at the saturated vapor pressure. The Equation 3.11 represents the saturated liquid pressure. Using this equation, the value of saturated liquid pressure may yield a value higher than the atmospheric pressure. Since, the application of this model is to simulate the flow in fuel injector nozzles, where the injection and the exit pressure is more than 1000 times the atmospheric pressure, and this difference in saturated liquid pressure is very small compared to the operating pressure of the system. However, this makes it difficult to use for simulating the flow with the nozzle exiting into the atmosphere. Using the explicit approach for pressure reduces the computational time as well as the cost. However, to achieve a time step convergence for pressure, a density corrector equation is solved implicitly after the momentum equation and pressure is updated analytically again. This portion is explained in the coming sections.

The Equations 3.12 and 3.13 for liquid and gas phase respectively represent the speed of sound for pure phase. These equations are used to model the non-linear effects of compressibility in the solver for pure phase.

$$a = \sqrt{N \frac{(B/N) - p_i^{sat} + p}{\dots}} \quad 3.12$$

$$a = \sqrt{x \frac{p}{\dots}} \quad 3.13$$

Numerical approach

A single fluid approach is used in this model. The phase change is defined by an equation of state given by the Equation 3.6, 3.7 and 3.8. This means that the basic transport equations used are the same as for the compressible single phase flow. The continuity equation given in the Equation 3.1 is transformed in terms of a volumetric flux (and represented by the Equation 3.14). The volumetric flux used in the equation is based on the velocity field from the previous time step. The continuity equation is discretized and solved for predicting the density and the mass flux () for the current time step. The Euler implicit method is used for the time derivative whereas for the spatial derivative, Minmod TVD scheme is used.

$$\frac{\partial \dots}{\partial t} + \nabla \cdot (\{ \dots \}) = 0 \quad 3.14$$

Using the new density, void fraction is calculated using the Equation 3.5. Void fraction is used in calculating the viscosity using the Equation 3.15, which forms a density-weighted average. The pressure is also predicted using the density by solving the explicit Equations 3.6, 3.8 and 3.10.

$$\sim = \sim_v r + \sim_l (1 - r) \quad 3.15$$

Solving the Navier-Stokes equations requires a close coupling between velocity and pressure. To establish this coupling, various approaches are in existence such as SIMPLE, SIMPLER, SIMPLEC and PISO. These approaches are used to minimize the non-linearity in the momentum equation to establish stable coupling between pressure and velocity. The velocity is predicted without adding the pressure gradient as shown in the Equation 3.16.

$$\frac{\partial \vec{U}}{\partial t} + \nabla \cdot (\rho \vec{U} \vec{U}) = \nabla^2 \vec{U} \quad 3.16$$

The density and the mass flux, calculated in the current time step, are used to obtain the solution for the momentum equation. The time derivative is discretized using the Euler implicit method (the same as the continuity equation), whereas the spatial derivative is discretized using the Minmod convective scheme. A new volumetric flux is obtained from the velocity field, which is lagged with pressure. To calculate the fluxes, the dot product of the interpolated velocity to the faces is taken with the face normal. To make the volumetric flux independent of t , a temporal correction is added. This term accounts for the divergence of the face velocity field by taking out the difference between the interpolated velocity and the flux. In an ideal system, this difference should be equal to zero, but this is not true in the actual numerical calculation due to presence of discretization and time step errors. To minimize this error, the temporal correction is applied. This is shown in the Equation 3.17, where $\{\dot{v}_v^*\}$ refers to the volumetric flux with the lagged pressure and $n-1$ refers to the value from the previous time step [59].

$$\{\dot{v}_v^*\} = \overline{U}^{n+1} \cdot S_f + \frac{1}{\Delta t} \{Coeff\} \left(\frac{1}{a_p} \overline{\{\dot{v}_v\}}^{n-1} - \frac{1}{a_p} \overline{\{U\}}^{n-1} \cdot S_f \right) \quad 3.17$$

Where, coeff is defined by the Equation 3.18.

$$\{_{Coeff} = \left(1 - \min \left(\frac{\text{mag}(\{_{v} - \overline{U^{n-1}} \cdot S_f)}{\text{mag}(\{_{v})}, 1 \right) \right) \quad 3.18$$

The speed of sound is calculated analytically from the equation of state represented by the equation 3.4, 3.12 and 3.13. The compressibility is calculated from the reciprocal of the square of the speed of sound, which can be correlated from the Equation 3.3 and 3.20.

In the HEM, the pressure is calculated as a direct function of the density. In cavitating flow, the gradients for pressure and density are very high. This may lead to a production of numerical noise inside the physical domain, which are non-physical and must be removed. Solving the density equation coupled with the pressure can be useful in eliminating these numerical disturbances. To do this, the spatial derivative in the density equation, consisting of the volumetric flux and the density, is split into a convective term and a diffusive term as shown in the Equation 3.20. The split in volumetric flux is obtained from the Equation 3.19, which is the combination of volumetric flux without pressure and the gradient pressure term.

$$\{_{v} = \{_{v}^* - \frac{\nabla P}{a_p} \quad 3.19$$

In partial differential equations, a convective term helps to propagate a solution and diffusive terms dissipates the fluctuations. In this equation, the convective term consists of density and volumetric flux (which is lagged with pressure). The lagged pressure term is added back in the equation as diffusion term. The term a_p is the diagonal term of the momentum equation. The subscript p denotes

the point of interest, which was used by Ferziger and Peric [60]. Since the gradient of pressure has to be added explicitly, it forms a weak diagonally dominant matrix. To add stability to the solution, a deferred correction term is applied. In this term, the pressure is replaced by density multiplied by compressibility (which is a linear approximation of the pressure for small time step as obtained from the Equation 3.19).

$$\mathbb{E} = \frac{\partial p}{\partial \dots} \quad 3.20$$

The actual pressure term is added to the equation explicitly after these operations as shown in the Equation 3.21.

$$\left(\frac{\partial \dots}{\partial t} + \nabla \cdot (\xi_v \dots) - \nabla \cdot \left(\frac{1}{a_p} \nabla (\dots \mathbb{E}) \right) \right)_I = - \left(\nabla \cdot \left(\frac{1}{a_p} \nabla (\dots \mathbb{E}) \right) - \nabla \cdot \left(\frac{1}{a_p} \nabla p \right) \right)_E \quad 3.21$$

where, the left hand side of the equation is solved implicitly, represented by the subscript I, and the right hand side of the equation is solved explicitly, represented by the subscript E.

The discretization procedure for the density corrector equation is same as for the continuity equation. The Laplacian term in the equation is solved using a linear scheme, which is a second order central difference scheme. Non-orthogonal parts of the Laplacian term are handled with a deferred orthogonal correction. After correcting the density, the mass flux, the pressure, the void fraction, and the diagonal terms of the velocity equation are also updated. Iterations are performed for the density corrector equation. These iterations are required to minimize the error in using the deferred correction. In these iterations, the pressure equation is based on an analytical equation, which is solved explicitly. In actual PISO iterations, the pressure is solved implicitly. Solving the pressure implicitly uses a large amount of computational

resources, which increases the computational cost. Also, the pressure calculated from PISO creates an incompatibility with density. The explicit pressure equation makes the solver more efficient by decreasing the computational time and use of resources.

After solving the pressure, the gradient is added to the momentum equation as well as to the volumetric flux. This is done by adding the cell centered pressure gradient to the velocity as shown in the Equation 3.20. For the volumetric flux, the surface normal gradient of pressure was computed and added to the flux.

$$U = U^* - \frac{\nabla p}{a_p} \quad 3.20$$

where, U^* is the velocity without pressure gradient calculated from Equation 3.14.

To solve the set of discretized algebraic equations, a diagonal incomplete LU preconditioned bi-conjugate gradient solver is used. A TVD scheme, Minmod is used for the convective terms. For the gradient term, a second order linear scheme is used. Laplacian terms are solved using a second order central scheme with non-orthogonal correction. This numerical approach is implemented into OpenFOAM[59,61,62] as MasCavFoam. The Figure 3-1 demonstrates the flowchart of the MasCavFoam.

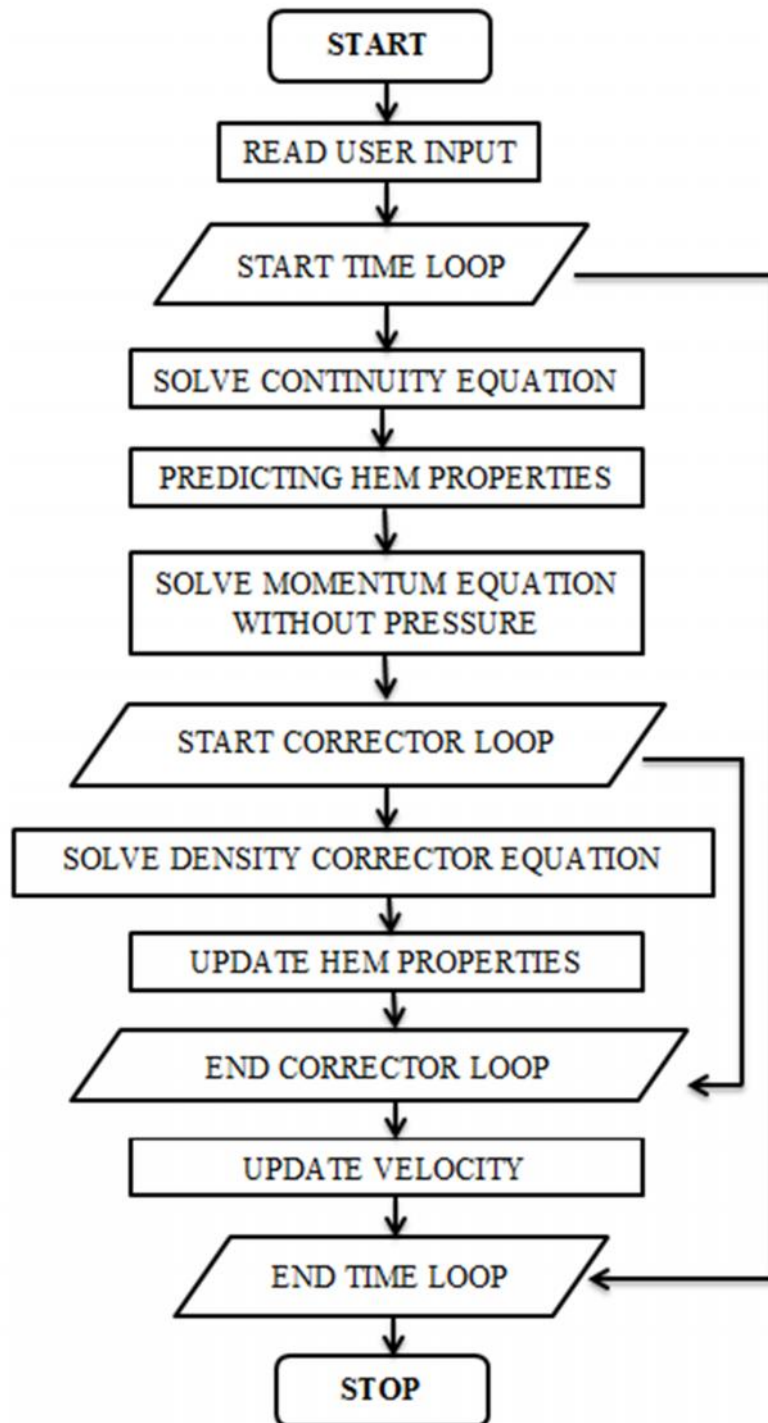


Figure 3-1 Flowchart for the MasCavFoam solver.

Boundary conditions

In numerical methods, different boundary condition may result in distinct solutions. Some of them may introduce non-physical influences on the domain. Arranging a correct set of boundary condition is important for physical stability inside the domain. In a fuel injector nozzle, the upstream condition consists of high-pressure fluid injecting inside the nozzle. The velocity at the far field of the upstream is close to zero. In the downstream of the nozzle, the pressure is very low and the velocity at the exit is almost 0.4 times the supersonic velocity of the fluid. Under cavitating conditions, cavitating bubbles may pass the exit boundary. Defining a boundary for such a region plays an essential role in establishing physical stability of the domain.

The upstream and the downstream velocity boundaries are specified as zero gradients. A floating boundary for velocity helps the flow to stabilize. The solver is designed to simulate high-speed flows in small fuel injector nozzles. The interaction between the solid wall and the fluid has limited viscous effects and is neglected in this simulation. A slip boundary on the wall is applied.

In this approach, the upstream density is defined by a total density boundary condition. This boundary is derived from the total pressure boundary condition and uses the same equation to calculate the pressure. Since the upstream condition is in pure liquid phase, Tait-Kirkwood equation is used to calculate the corresponding density at the boundary. This boundary adjusts with the old density value at the boundary and the current local velocity. In the Equation 3.21, P_0 is the total pressure set at the boundary and pos is a positive sign function which is zero, when the volumetric flux is less than 0 (i.e. the case for an inlet boundary).

$$p = p_0 - \frac{1}{2}(1 - \text{pos}(\xi_v)) \dots_{old} U^2 \quad 3.21$$

For the downstream pressure, a transmissive pressure boundary condition is applied. In this boundary, P and L are specified. P is the pressure at downstream and L is the relaxation length scale. A smaller relaxation length defines a more reflective boundary than the higher value. A non-reflective boundary helps the pressure waves to go out of the domain without creating disturbances to the interior domain. This approach uses the method of characteristics to define the density at the boundary. This is applied by calculating the amplitudes of the characteristic waves. This approach is similar to the Navier-Stokes Characteristic Boundary Conditions (NSCBC) given by Pointsot and Lele [58]. In their approach, the different waves crossing the boundary can be identified as acoustic, vorticity and entropy waves. Dumont et al [49-50] further simplified the NSCBC by neglecting the entropy waves to apply them for cavitating flow. In this approach, vorticity waves are neglected in the NSCBC approach and they are allowed to stabilize by applying a floating boundary condition for velocity at the exit. This means only acoustic wave treatment is performed at the density boundary. Using the similar notations as by Dumont et al, we will define our acoustic wave amplitude as L_1 and L_4 . A time dependent solution is obtained for density by solving the Equation 3.25.

$$L_1 = \frac{1}{2a^2} (u_n - a) \left[\frac{\partial P}{\partial n} + \dots a \frac{\partial u_n}{\partial n} \right] \quad 3.22$$

$$L_4 = \frac{1}{2a^2} (u_n + a) \left[\frac{\partial P}{\partial n} + \dots a \frac{\partial u_n}{\partial n} \right] \quad 3.23$$

$$k = \dagger (1 - M^2) a / L_\infty \quad 3.24$$

where, u_n is the velocity at the exit normal to the boundary, k represents the stiffness constant, β is a constant parameter for the stiffness and M represents the Mach number with respect to the local speed of sound. An optimized value of β by Pointsoot and Lele [63] is specified as 0.25.

$$\frac{\partial \dots}{\partial t} + L_4 - L_1 = 0 \quad 3.25$$

Depending on the nature of flow at the exit, following cases are considered :

Table 3-2 Characteristics based on nature of the flow

Nature of flow	L_1	L_4
Subsonic outflow	$k(-)$	Equation 3.23
Subsonic inflow	$k(-)$	Equation 3.23
Supersonic outflow	Equation 3.22	Equation 3.23
Supersonic inflow	$k(-)$	$k(-)$

L_1 represents the incoming acoustic wave and to avoid a drifting pressure associated with an open boundary condition [64], the equation given in the table is applied. This equation blends the boundary between non-reflective and reflective conditions. A lower value of k , makes the boundary more non-reflective and a higher value makes it more reflective in nature. L_4 represents the outgoing acoustic wave, which is calculated from the Equation 3.23. When the flow is supersonic inflow, which can hardly occur in our case but modeled to make the boundary consistent in all conditions, both the incoming and outgoing waves are computed from the values at the far downstream of the exit.

CHAPTER 4

VALIDATION AND RESULTS: 2D INJECTORS

Fuel is injected in a real fuel injector nozzle at a very high pressure, which makes the velocity inside the nozzle correspondingly large. With the high velocity, the size of the nozzle and the time scale of fluid passing through the nozzle are very small, impeding the experimental work to analyze them. Many experiments were performed in the past with transparent round and planar nozzles [6,27,31,32,33,65-72] to study the internal behavior of the nozzle. Most of the experiments were performed at an atmospheric exit condition and low upstream pressures, which leads to a very low velocity inside the nozzle (around 5-40 m/s).

In the current HEM approach, flow is mainly driven by the pressure difference, and the model is more suitable for high-speed flows. At low velocity conditions, the acoustic velocity is very high compared to the flow velocity. This value is almost 30 times the maximum flow velocity inside the nozzle for the low injection pressure conditions. This means that when the flow velocity moves to the adjacent cell in the direction of the flow, the acoustic wave travels more than 30 times. The boundary condition at the exit is partially non-reflective to maintain the specified outlet condition and bounces a small portion of this acoustic wave inside the nozzle. This means by the time flow moves through a few cells in the flow direction, the acoustic noise fills the outlet domain and affects the nature of the flow. This is true for higher velocities too, but the ratio of the acoustic to flow speed is lower and the noise inside the domain either dissipates over the time or moves out with the flow. Decreasing the inlet pressure further gives a very low flow speed, which creates stiffness in the current approach.

Flow through a venturi nozzle

The validation of the code begins with a non-cavitating flow through a venturi. A higher r/D ratio is selected such that the non-cavitating behavior of a venturi can be studied and the model can be tested for non-cavitating flows. The size of the venturi is very small (in the range of real fuel injector nozzles) and the flow velocity is in the range of 0.15-0.4 Mach. The L/D ratio of the geometry is four to avoid any head loss due to length of the nozzle. The coefficient of discharge in a high r/D ratio nozzle with high Reynolds number is very close to unity, which means head loss due to viscosity is also small. Now applying a slip boundary condition at the wall, the flow velocity at the center should follow the theoretical velocity calculated from the law of conservation of energy. The theory is applied to the geometry shown in the Figure 4-1, where the inlet velocity is assumed zero and the Equation 4.1 is derived. Rearranging this equation, the velocity at the exit can be stated as the Bernoulli velocity and can be calculated using Equation 4.2.

$$\frac{p_1}{\dots_1} + \frac{1}{2} U_1^2 = \frac{p_2}{\dots_2} + \frac{1}{2} U_2^2 \quad 4.1$$

$$U_{Theoretical} = U_2 - U_1 = \sqrt{2 \left(\frac{p_1}{\dots_1} - \frac{p_2}{\dots_2} \right)} \quad 4.2$$

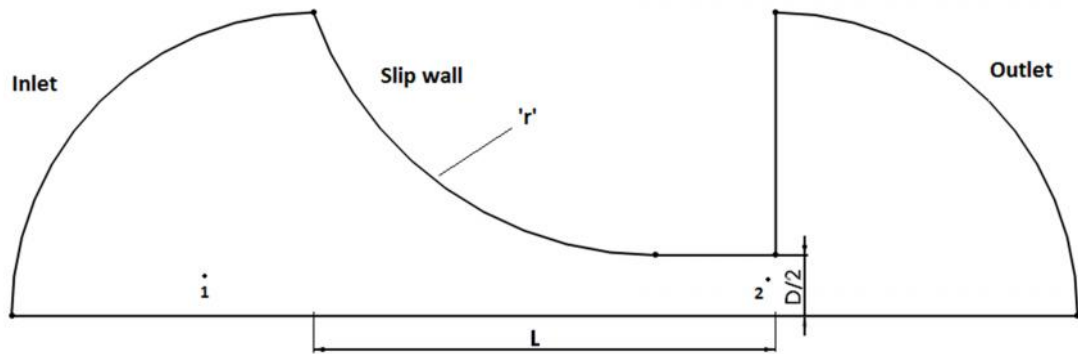


Figure 4-1 The schematic of the 2-D axisymmetric venturi nozzle

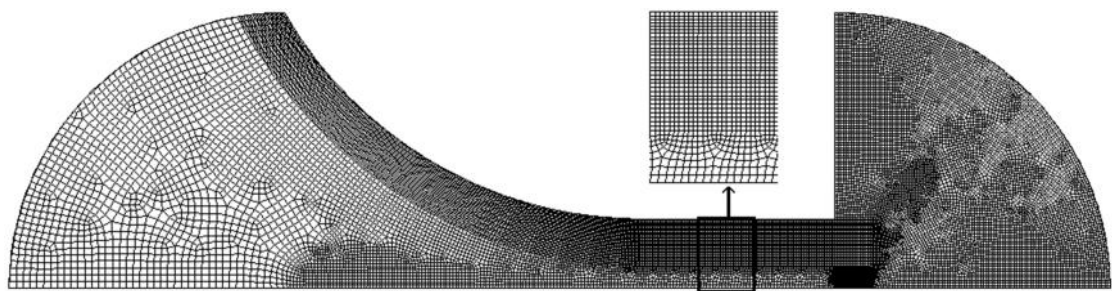


Figure 4-2 The meshed geometry with around 25K cells

In this model, equilibrium properties of a fluid are required to determine the pressure and the compressibility. These properties are easily available for water, which makes it an ideal working fluid for this validation. Moreover, water is also used in many experiments associated with detecting cavitation in injector nozzles, which makes it easy to correlate the simulations with experiments. These properties of water used for the simulation are listed in the Table 4-1. These properties are at 308K and extracted from the NIST website [73].

Table 4-1 Properties of water at 308 K

α_g	$5.59 \times 10^{-6} \text{ s}^2/\text{m}^2$	p_l^{sat}	78134.75 Pa
α_l	$4.55 \times 10^{-7} \text{ s}^2/\text{m}^2$	μ_g	$1.002 \times 10^{-3} \text{ Pa}\cdot\text{s}$
ρ_g	$0.01716 \text{ kg}/\text{m}^3$	μ_l	$1.3 \times 10^{-5} \text{ Pa}\cdot\text{s}$
ρ_l	$998.19 \text{ kg}/\text{m}^3$	N	7
p_v	3070 Pa		1.05

For convenience, axisymmetric nozzles were simulated and the diameter of the nozzle used was kept at a same range as the real fuel injector nozzles i.e. 100 μm . The total number of cells in the mesh is around 25000. The total number of cells along the radial direction is around 40. A series of simulations were performed at various pressure differences. The simulations were performed until a stable mass flow rate at the inlet and the outlet is attained. The Figure 4-3 and Figure 4-4 shows the steady state result at $t=0.1 \text{ ms}$ for the inlet pressure of 200 MPa and the outlet pressure at 100 MPa (a pressure difference of 100 MPa). Using the Equation 4.2, the theoretical value of the velocity calculated as 426.9 m/s, whereas the mean centerline velocity at the exit from the simulation was 420.68 m/s. The value yielded from the simulations is very close the one calculated from theory with an error less than 2%. All simulations were performed with higher order discretization methods. For gradients, a second order central scheme was used whereas for the convective term in the governing equations, a Minmod TVD scheme was used. The pressure and the

density contour clearly displays the outgoing compressible pressure waves exiting the domain. A series of snapshots at various time steps are displayed in the Figure 4-6, showing the compressible waves exiting the domain at an exit pressure of 100 MPa.

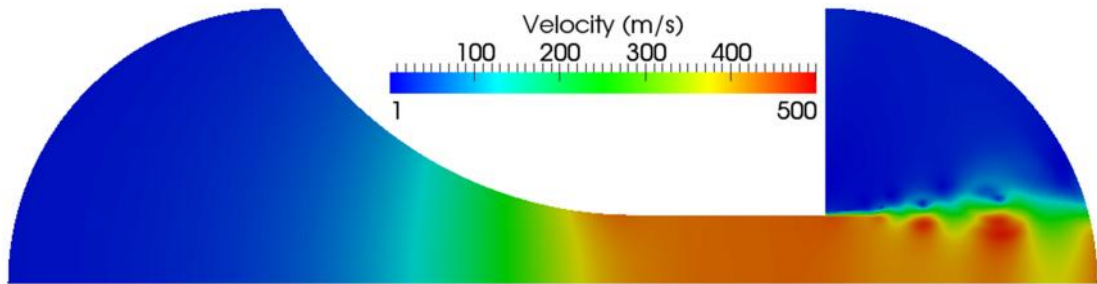


Figure 4-3 Velocity contour at 100 MPa exit pressure for the axisymmetric venturi with Minmod convective scheme.

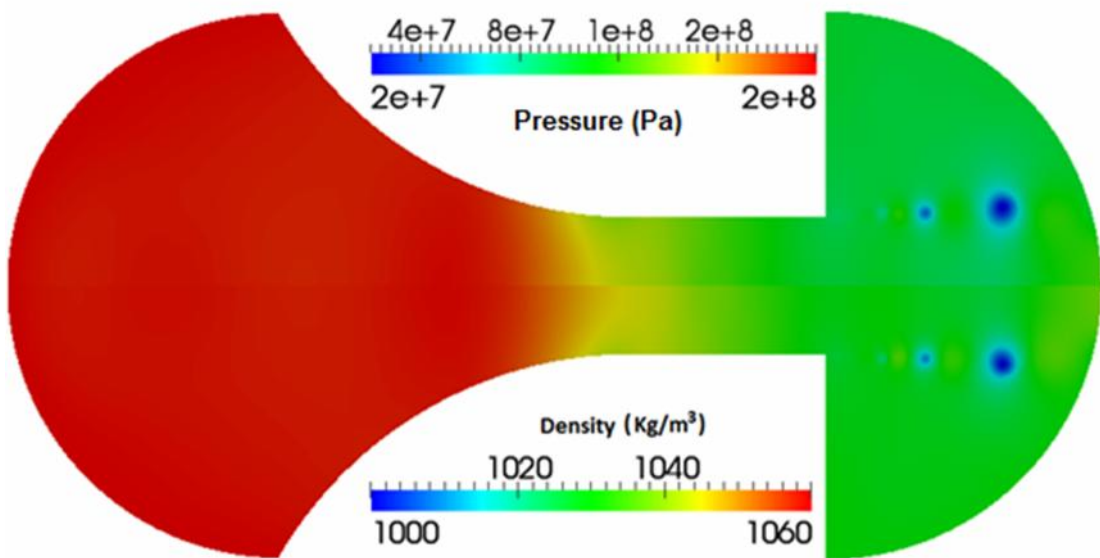


Figure 4-4 Pressure and density variation for the axisymmetric venturi at 100 MPa downstream pressure with Minmod convective scheme

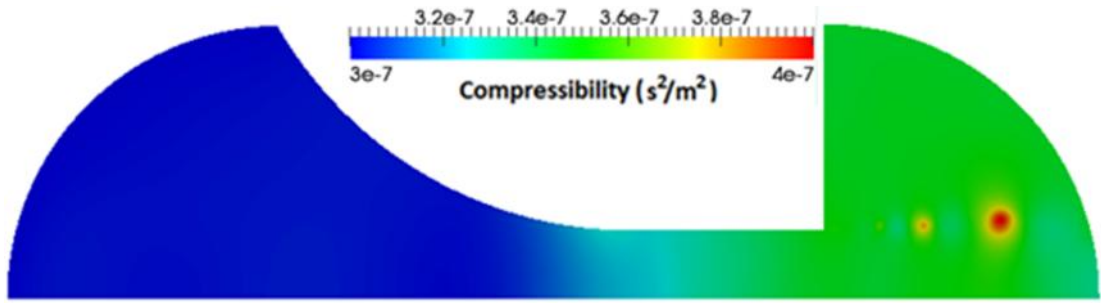


Figure 4-5 Compressibility variation for the axisymmetric venturi at 100 MPa downstream pressure with Minmod convective scheme.

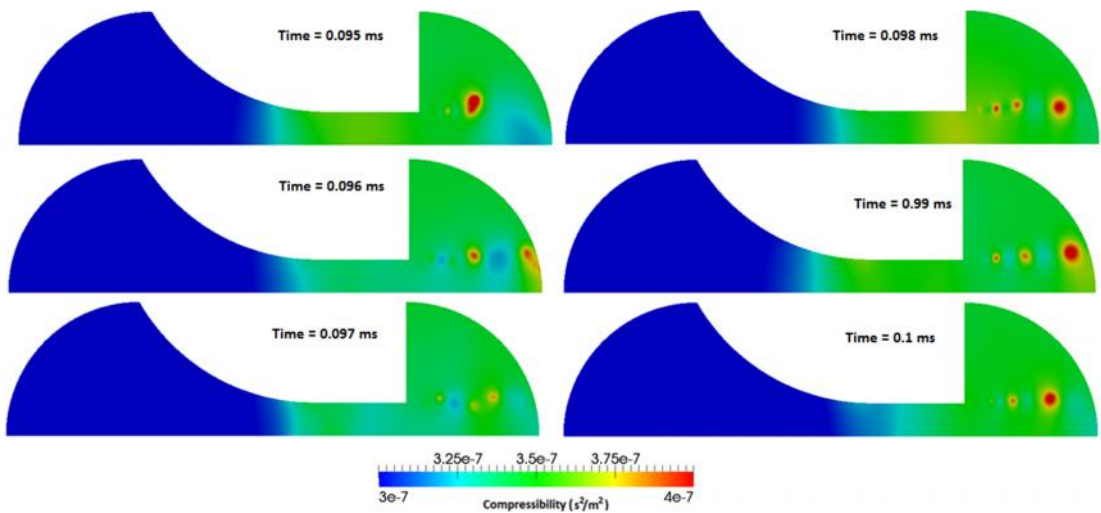


Figure 4-6 Compressible pressure waves exiting the domain at 100 MPa downstream pressure

The exit velocities obtained from the series of simulations were compared with the corresponding theoretical velocities. The results obtained from the simulations, displayed in the Table 4-2, are in close agreement with the theoretical values. The maximum difference calculated for all the results is around 2%. The results were plotted on a graph Figure 4-7 with the mean centerline exit velocity on the y-axis and the pressure difference was plotted on the x-axis. In the graph, the

theoretical velocity is plotted with solid lines and filled gradient symbol whereas filled square symbol represents the simulated results. The comparisons of the simulated cases were shown in the Table 4-2.

Table 4-2 comparisons of the venturi results

Pressure Difference (MPa)	U_{Theory}	$U_{\text{numerical}}$	% difference
25	211.43	209.5	-0.9
75	368.48	365.1	-0.9
100	426.90	420.68	-1.4
125	478.97	470.22	-1.8

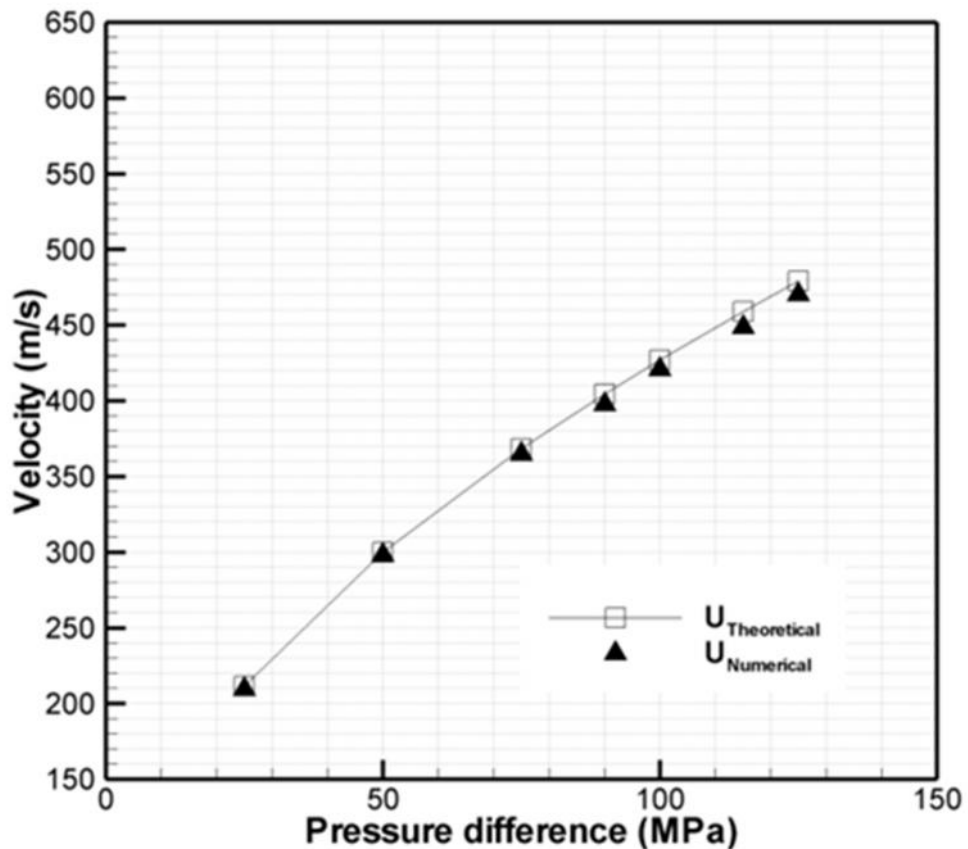


Figure 4-7 Velocity comparisons with the theoretical velocity at various pressure differences.

Simulation of flow in high speed nozzles

The next step was to validate the code for cavitating nozzles. The flow was simulated inside a sharp nozzle with the pressure condition similar to the real size injector nozzles and the results were validated using the Nurick's theory and the experiments performed by various researchers. The Figure 4-9 illustrates the geometry of the nozzle used in the simulation. The diameter of the nozzle is $100\ \mu\text{m}$, which is similar to the real size injector nozzle, and the pressure is injected at 200 MPa. The sharp inlet creates a potential for separated flow, which induces cavitation. At a sharp inlet, the gradients are very high and to avoid imposing a boundary condition at such location, plenums were added at the inlet and the outlet. For convenience, axisymmetric nozzles were simulated for the study. The geometry was meshed with quadrilateral elements and the mesh size is around 25000 cells. The number of cells in the radial direction is around 45. The meshed geometry is shown in the Figure 4-9.

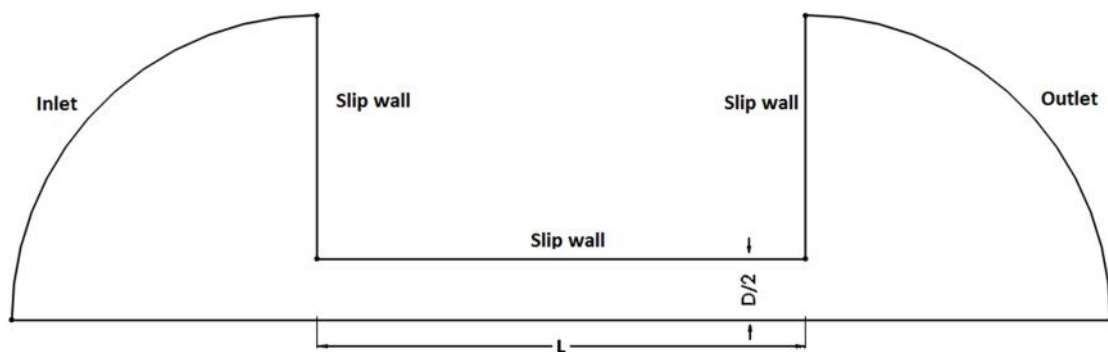


Figure 4-8 Schematic of the 2-D axisymmetric nozzle

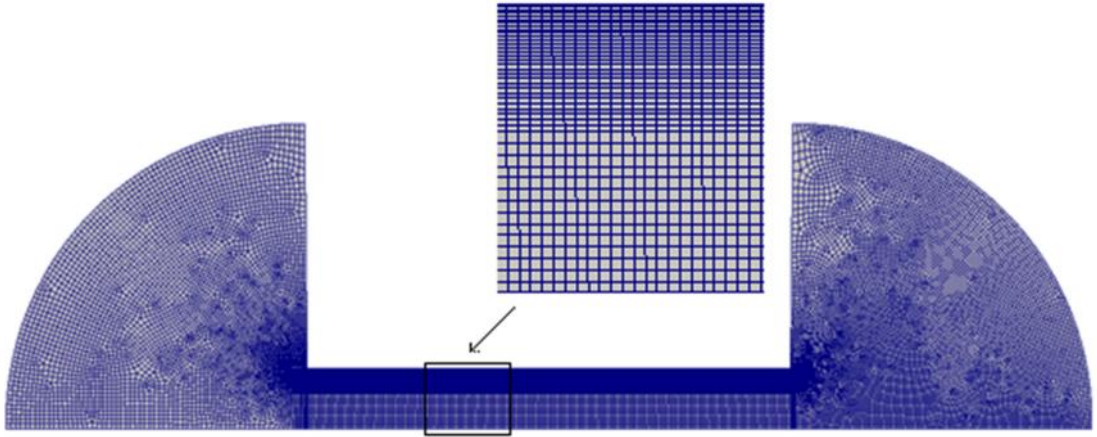


Figure 4-9 Meshed geometry of the 2-D axisymmetric nozzle.

Flow through the axisymmetric nozzle was simulated using water. Properties of water in the Table 4-1 were used. Using the Equation 3.6 and these properties, a variation of the pressure in the two-phase regions is presented in the

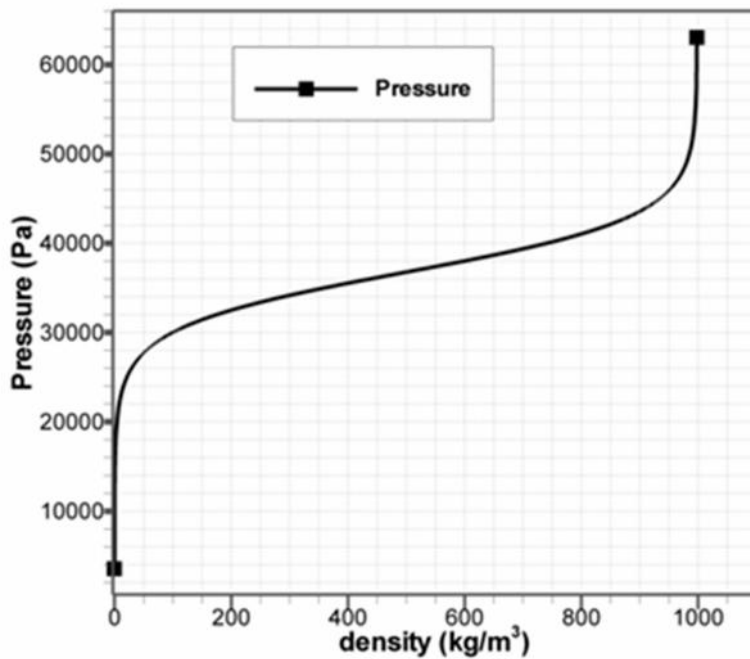


Figure 4-10. Also, the variation of acoustic speed in water is displayed in the Figure 4-11, which is derived from the equation given by Wallis [56] and mentioned in the model description. From the plot we can see that the speed of sound near the pure phase region decreases sharply as it becomes two-phase, where the speed of

sound is very low. If we compare the speed of sound (of both two-phase and the pure liquid phase), it differs by a factor of 1000. Due to such sharp behavior, the flow produces numerical shocks with high gradients. Simulating the flow in such condition is challenging and applying an appropriate convective scheme to capture the shocks as well as provide stability is necessary. Using a second order scheme for the convective terms can increase accuracy but introduces instability due to oscillations produced by such scheme. A first order scheme is stable but tends to add numerical diffusion to the solution. To have a proper blending between accuracy and stability, total variation diminishing (TVD) schemes are used. Minmod is one of the TVD schemes that can produce accurate and stable results, which is more suitable for these simulations. The other terms in the governing equation are dealt with a second order central scheme.

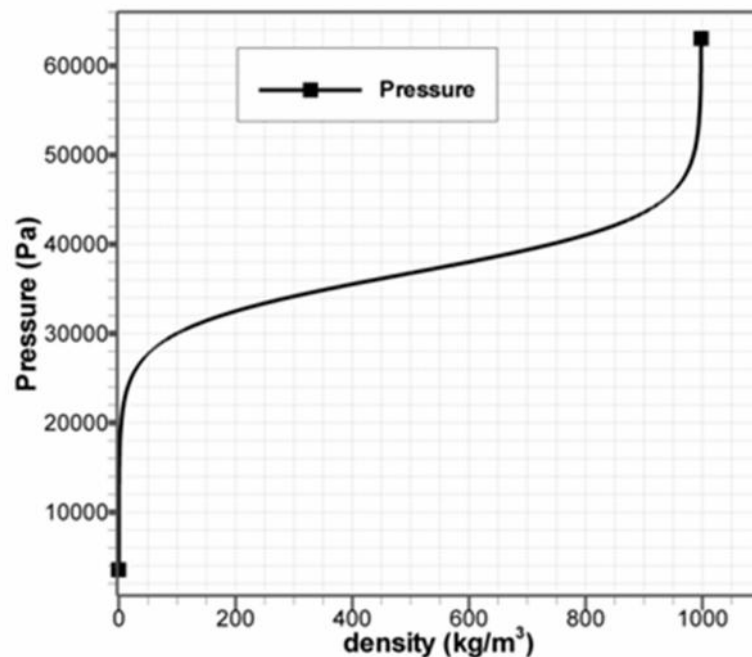


Figure 4-10 Pressure plotted against density in the two phase regions for water

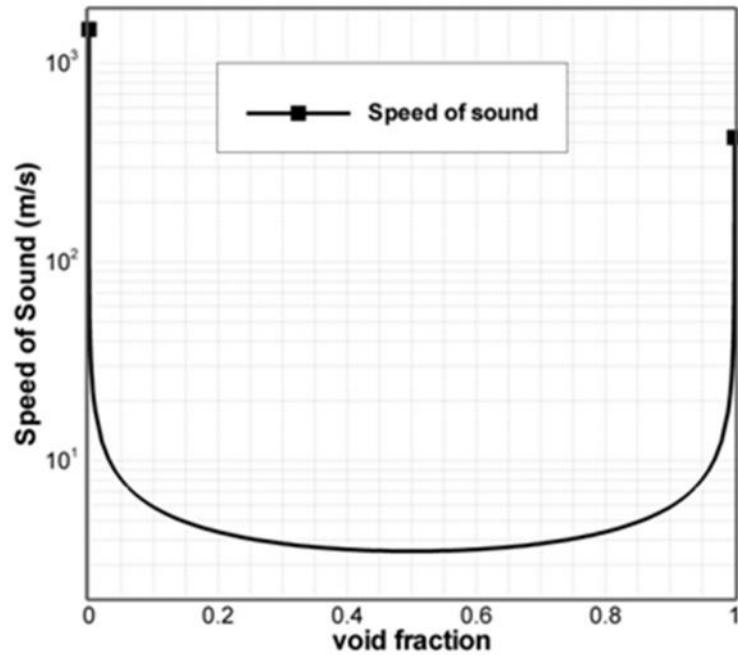


Figure 4-11 Variation of the acoustic speed in water using HEM.

The inlet pressure for all the simulations were kept constant at 200 MPa. The outlet pressure was varied from 1 MPa to 100 MPa. The cavitation number was calculated using Equation 2.2. In the Figure 4-14, the pressure and the density contour for $K=1.05$ is shown. In this case, the outlet pressure was set at 10 MPa. Inside the nozzle, the sharp inlet forms a sudden contraction that causes an instantaneous increase in acceleration. At this point, a boundary layer tends to separate and a re-circulation appears with the fall in pressure. The fall in pressure drops the pressure below the saturated liquid pressure and a two-phase mixture is formed. A vena contracta region can be seen near the sharp inlet in the Figure 4-12 . This leads to the formation of a vapor region along the wall. When the pressure difference between the inlet and the outlet is very large (as in this case), the cavitation bubbles were observed exiting the domain. Chaves et al.[15,16] observed this phenomenon in their experiments and termed it as ‘supercavitation’. Relating this phenomenon with the cavitation number we can say, supercavitation occurs when the cavitation number is

very close to unity. Cavitation number is dependent on the inlet and the outlet pressure condition (while the vapor pressure remains a constant value for a given fluid at a constant temperature). Provided the outlet condition is above the vapor pressure of the liquid, the value of K always remains above unity. Thus, at a very large pressure difference condition, the supercavitation phenomenon may occur.

The velocity and the change in compressibility at $t=0.5$ ms is shown in the Figure 4-16. All these nozzles were simulated as submerged. The flow exits the domain into a fluid filled outlet plenum where the exit pressure is specified. Under cavitating conditions, the pressure inside the nozzle is very low and the exit pressure is very high. Due to the sudden rise in pressure near the exit of the nozzle, a shock is created in this region. The figure shown for the cavitation cases displays these shock area very clearly in all properties. The Figure 4-15 displays the void fraction and the turbulence kinetic energy when the nozzle is undergoing phase change.

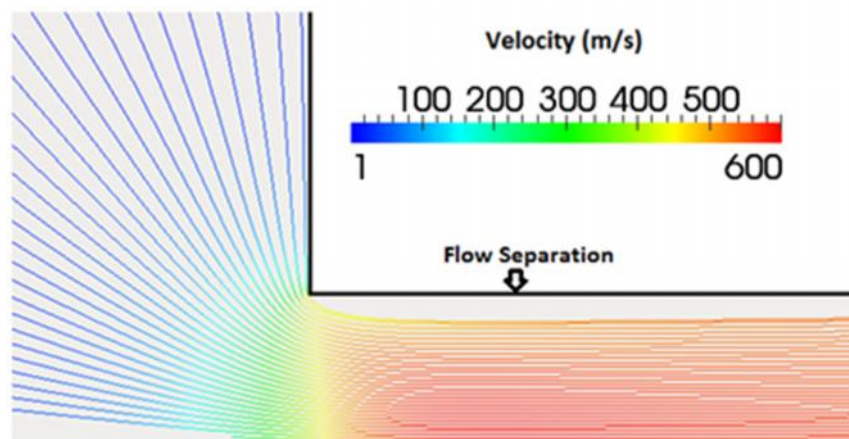


Figure 4-12 Velocity streamlines for $K = 1.05$ at the sharp inlet for the axisymmetric nozzles with Minmod convective scheme and k - turbulence model.

The acceleration of the fluid due to the vena contracta can be seen in Figure 4-12. The blue color represents low velocity and the red color represents high velocity. In the figure, an increase in the velocity due to sudden contraction can be

seen and the streamlines shows a smooth transition in the increase in the velocity at the inlet and the flow separation near the wall is also observed. In the Figure 4-13, the streamlines at the exit is shown and the shock in the transition is observed near the exit. The separated flow at the inlet is seen stretched out of the exit showing the ‘supercavitation’ flow.

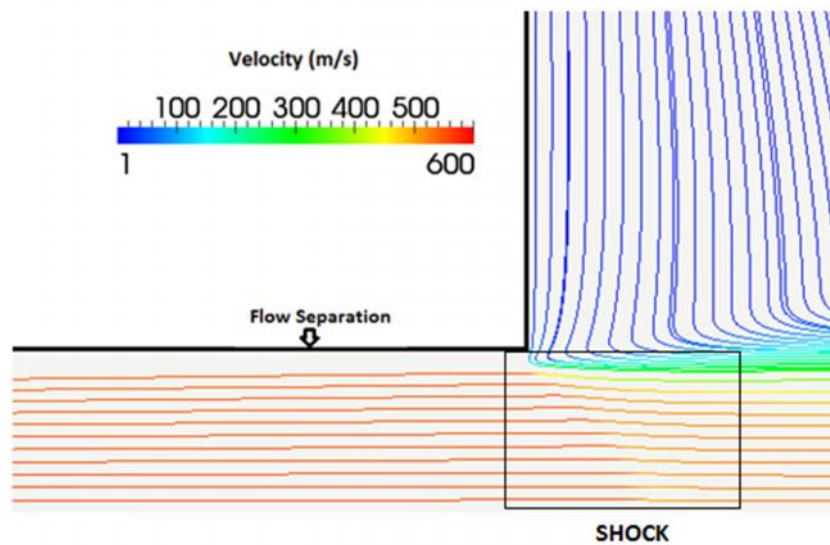


Figure 4-13 Velocity streamlines for $K = 1.05$ at the exit for the axisymmetric nozzles with Minmod convective scheme and k - turbulence model.

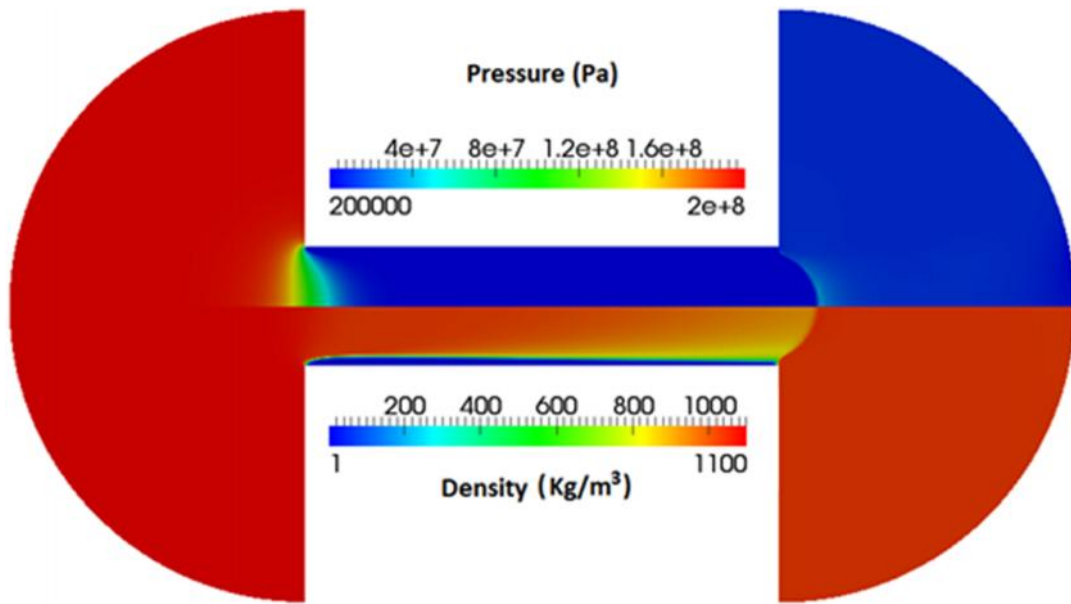


Figure 4-14 pressure and density contours at $K=1.05$ for the axisymmetric nozzle with Minmod convective scheme and $k-$ turbulence model.

The Figure 4-14 shows the density and the pressure contour for a supercavitating case. A shock near the exit is visible near the exit. This shock is due to a rapid transition from low pressure region to high pressure outlet plenum. The Minmod scheme is used for the convective terms. A stable calculation in the presence of shock waves requires a certain amount of numerical dissipation. Using a first order upwind scheme tends to add more numerical dissipation and preserving the shock is difficult. On the other hand, a second order linear scheme is oscillatory in the presence of shock and makes the solution unstable. Using a TVD scheme for the solution preserves the monotonicity in the solution without affecting the stability. The presence of the shock near the exit is consistent with the cavitating cases and the solver.

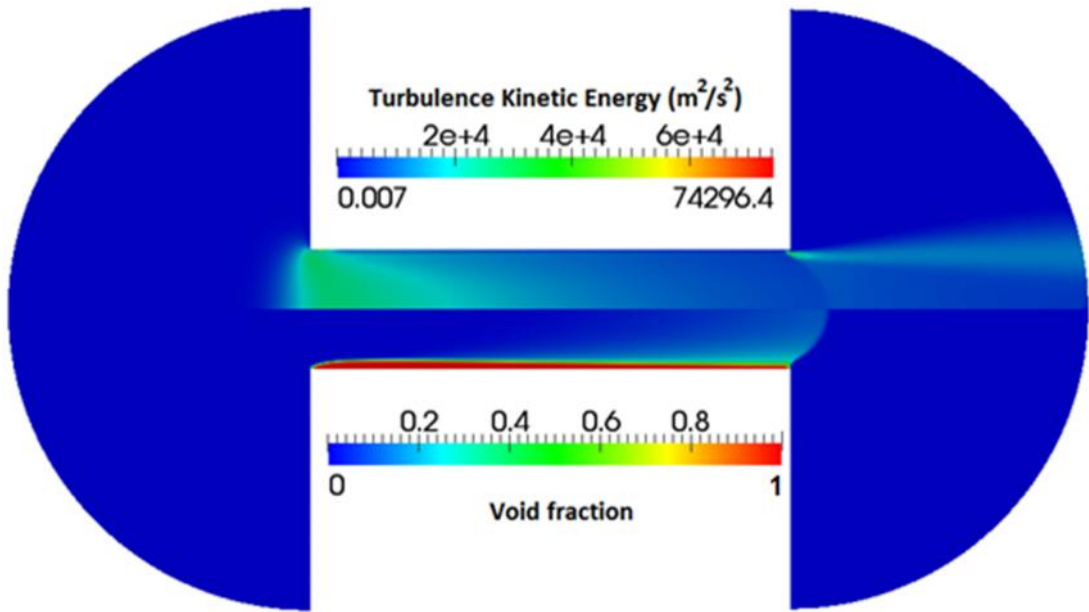


Figure 4-15 Turbulent kinetic energy and void fraction contours at $K = 1.05$ for the axisymmetric nozzle with Minmod convective scheme and $k-$ turbulence model.

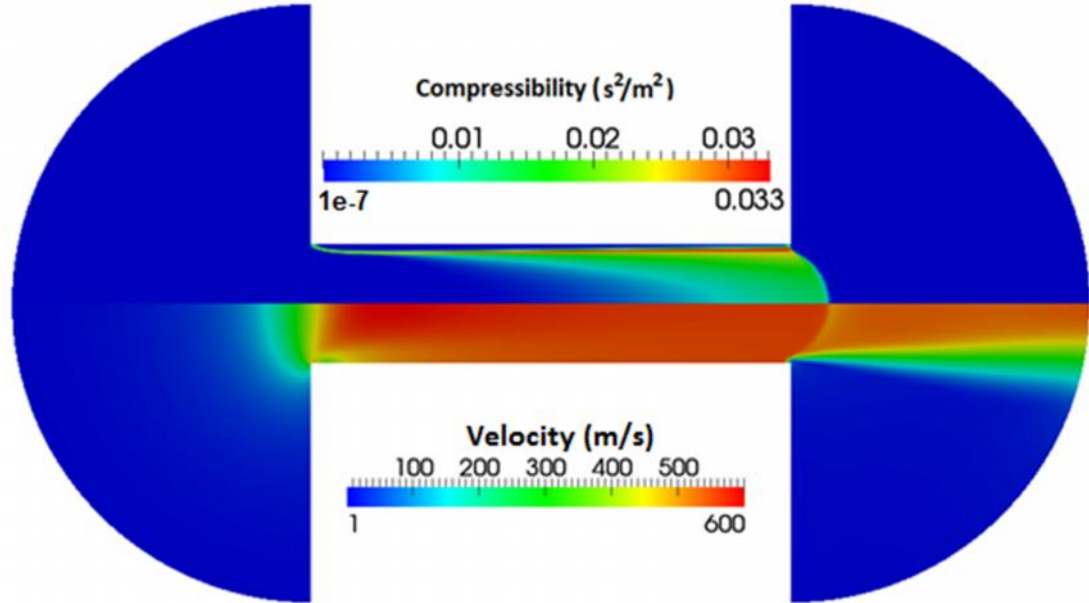


Figure 4-16 Velocity and compressibility at $K=1.05$ for the axisymmetric nozzles with Minmod convective scheme and $k-$ turbulence model.

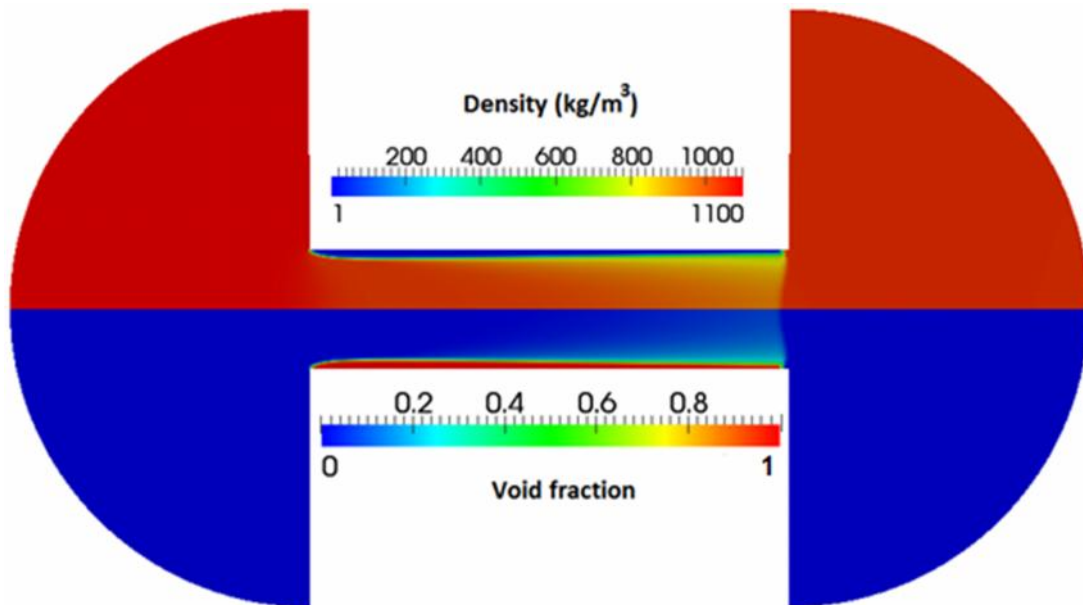


Figure 4-17 densities and void fraction at $K=1.25$ for the axisymmetric nozzle with Minmod convective scheme and k - turbulence model.

During cavitation, the flow inside the nozzle was observed as ‘choked’ in the simulations. In such a condition, the mass flow rate remains constant even though the outlet pressure was changed. In another case, with slightly higher value of K , the cavitation was observed and it is shown in the Figure 4-17. In this case, the pressure at the outlet was set to 40 MPa. A decrease in pressure difference results in a slight decrease in the cavity length. In this case, the mass flow rate obtained is same as in the earlier case. This observation is consistent with the idea of choked flow inside the nozzle under cavitation. The importance of a choked flow is that the mass flow rate is not affected by the downstream attributes. The upstream characteristics control the mass flow rate at such conditions.

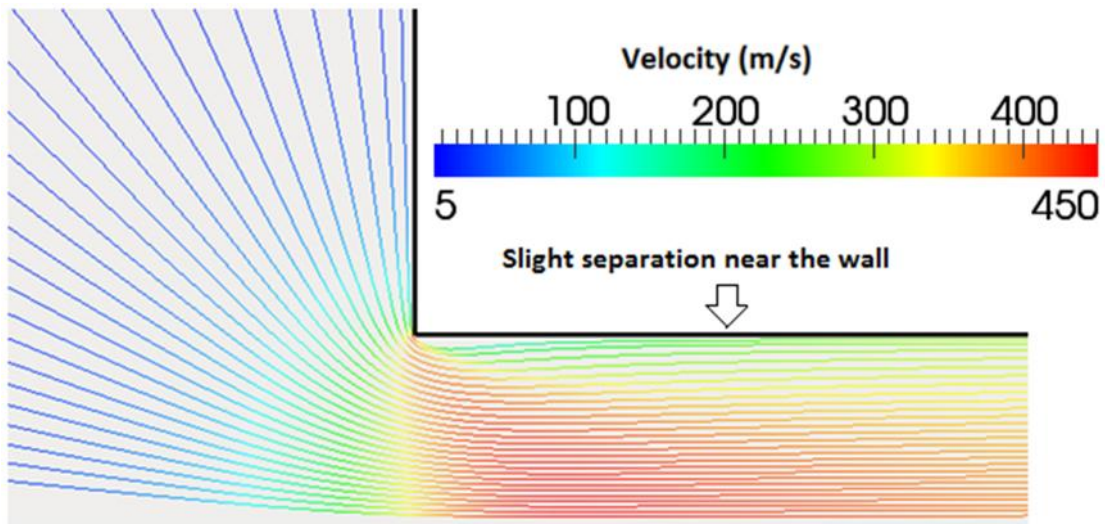


Figure 4-18 Streamlines for non-cavitating nozzle flow at $K = 2$ showing no separation at near the wall

The outlet pressure was further increase and after a few increments, a change in mass flow rate was observed. This was because of the transition to a non-cavitating flow inside the nozzle. Observations with $K=2$ are shown in the Figure 4-19. The downstream pressure was set at 100 MPa (half the pressure on the upstream). It was observed that pressure inside the nozzle remains well above the saturated vapor pressure. This indicates a non-cavitating flow inside the nozzle at higher values of K . In this condition, the flow separation (due to a fall in local pressure below the saturation pressure) was diminished (visible in the Figure 4-18) and now the complete area was available for the flow. This explains that the choked flow in the nozzle exists only for a cavitating conditions. Once the pressure difference is decreased (or the cavitation number is increased), a non-cavitating flow in the nozzle was observed.

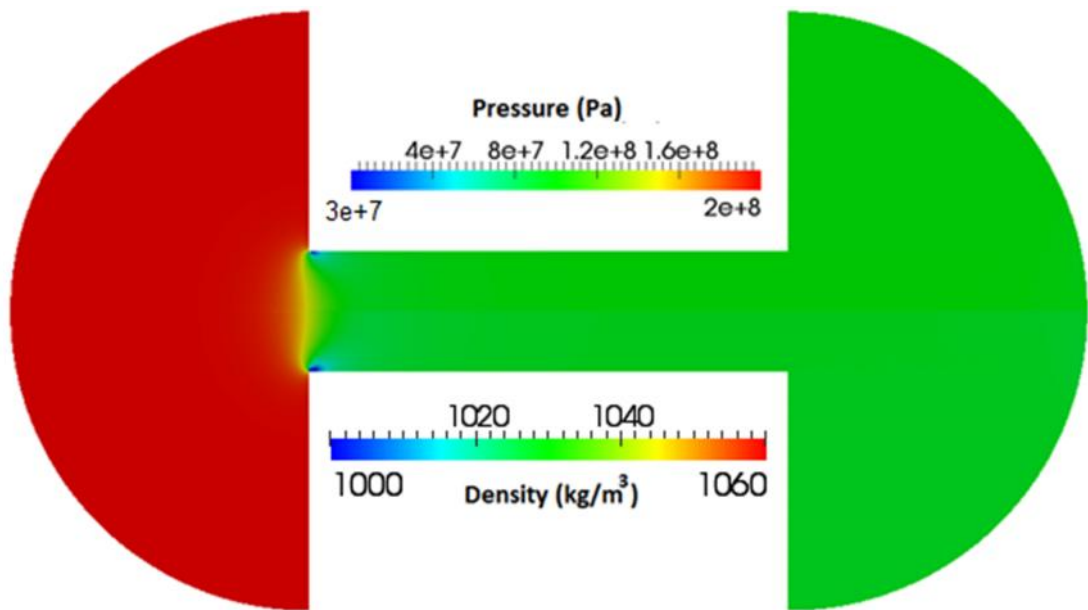


Figure 4-19 Pressure and density contour at $K=2$ for the axisymmetric nozzles with Minmod convective scheme and k - turbulence model.

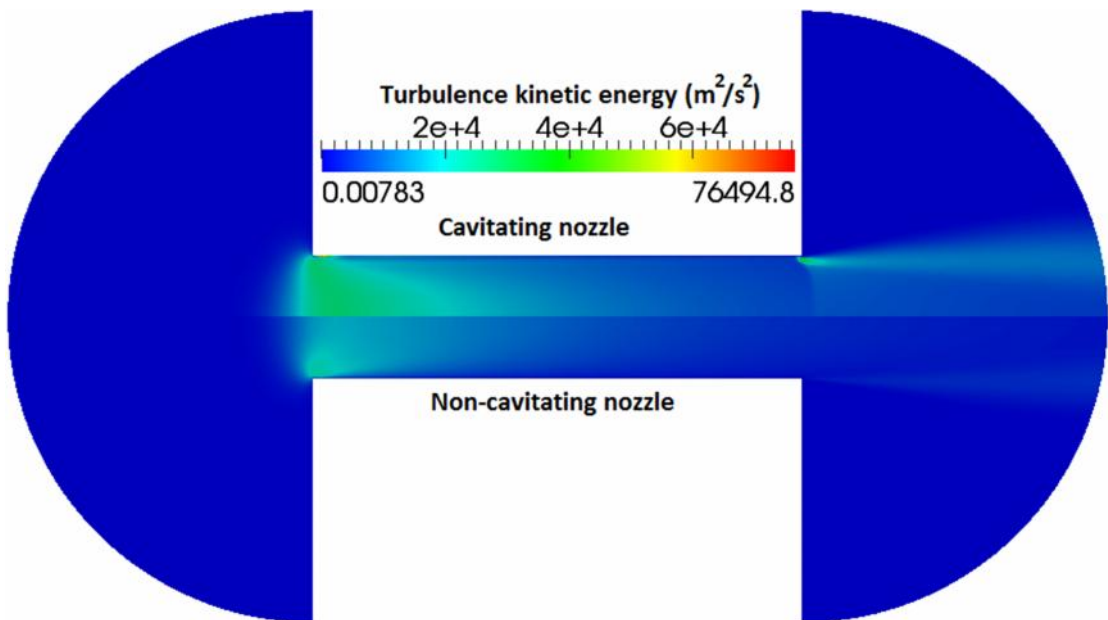


Figure 4-20 The turbulence kinetic energy for the cavitating ($K=1.1$) and non-the cavitating nozzle ($K=2$) for the axisymmetric nozzles with Minmod convective scheme and k - turbulence model.

The Figure 4-19 shows the difference in turbulence kinetic energy between a non-cavitating and cavitating nozzle. The cavitating nozzle shown is at a high-pressure difference, and the flow speed is higher than the non-cavitating nozzle. Higher acceleration in the nozzle in the cavitating nozzle results in predictions of higher turbulence kinetic energy. In a non-cavitating nozzle, the pressure inside the nozzle is within the range of the outlet pressure. As there is a smooth transition at the exit of the nozzle, the shock observed in a cavitating case is absent in case of the non-cavitating nozzle.

Outlet pressure was varied and more simulations were performed at different cavitation numbers. The mass flow rates obtained from the simulations were used to calculate the coefficient of discharge of the nozzle. These results were then compared with the relations provided by Nurick[26]. According to Nurick, the coefficient of discharge is directly proportional to the square root of the cavitation number when nozzle is cavitating. This means C_d obtained from the simulations should follow the relation 2.2. To calculate the C_d , the equation 4.3 is used.

$$C_d = \frac{\dot{m}_{numerical}}{\dot{m}_{theoretical}} = \frac{\dot{m}_{numerical}}{A\sqrt{2(P_1 - P_2) \dots l}} \quad 4.3$$

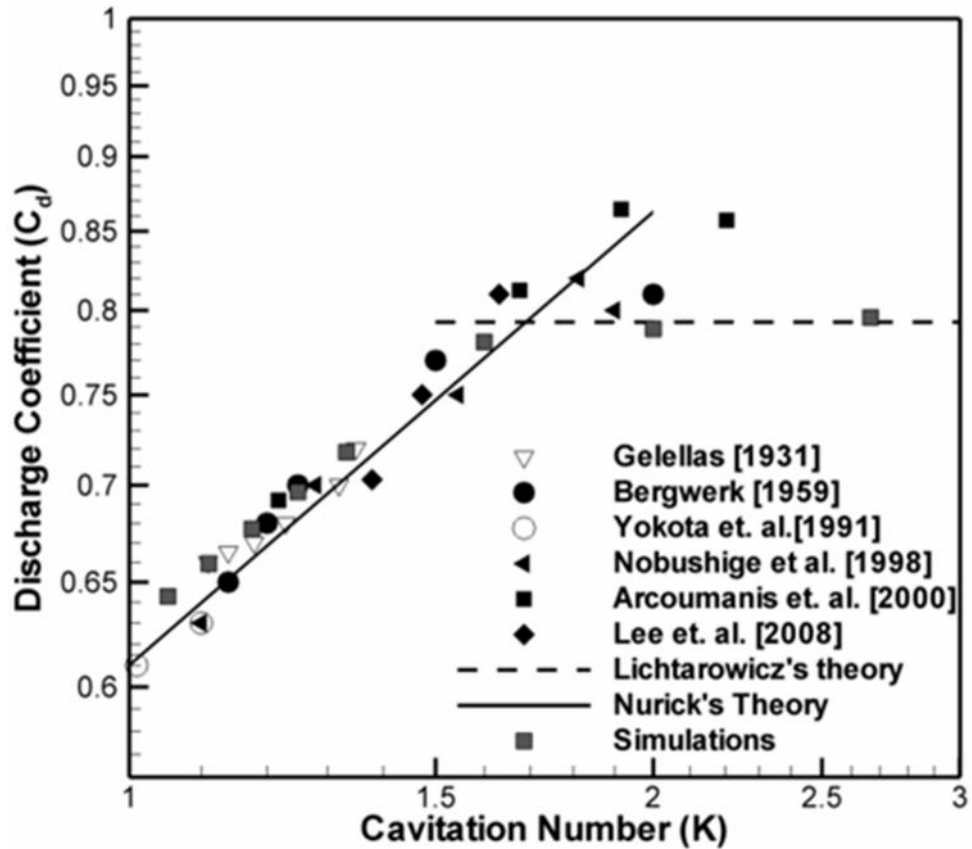


Figure 4-21 Cavitation number (K) vs. discharge coefficient (C_d)

The computed coefficient of discharge was compared with the cavitation number in the Figure 4-21. The figure shows that the data taken from simulation results agree extremely well with the theory given by Nurick. The critical cavitation number is recorded near $K=1.6$, where cavitation inception is observed. The value of critical cavitation number is dependent on the Reynolds number and changes with the different fluid conditions and fluid properties. The solid vertical line separates flow regimes observed in the nozzle. The right hand side to this line represents cases with non-cavitating flow. Cavitation confined at the inlet may appear at the sharp inlet due transient nature of the flow and the pressure may fall during this process. The result from the non-cavitating cases were not in agreement with Nurick's cavitation model and the coefficient of discharge is governed by the fluid properties. The results

obtained for the non-cavitation were in agreement with the relation given by Lichtarowicz et al. [27] given by the Equation 4.4.

$$C_d = 0.827 - 0.0034(l/D) \quad 4.4$$

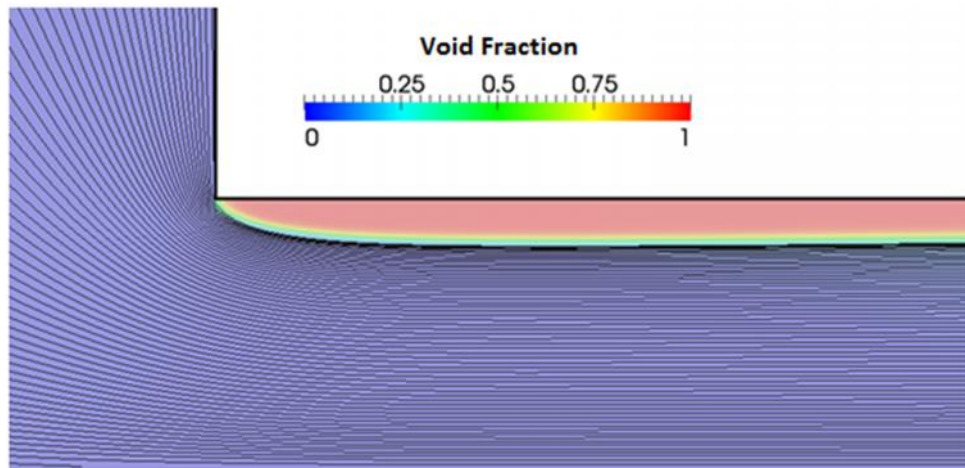


Figure 4-22 Velocity streamlines superimposed over the void fraction

The black velocity streamlines are superimposed over the void fraction contour to show the effective area available for the flow in the Figure 4-22. The separation in the streamlines is very close to the start of the interface between the two-phase and pure phase flow.

The contraction coefficient for a sharp nozzle from theory of potential flow is calculated by Von Mises [74] as 0.611. Estimating the value of the contraction coefficient of the results obtained in the Figure 4-14 will be interesting to investigate. To do this, the void fraction is plotted against the non-dimensional radial distance for the nozzle simulation with $K=1.1$ in the Figure 4-23 **Error! Reference source not found.** A transition in phase is observed at $r/R=0.78$. This implies the radius available for the flow is 0.78 times the actual radius. Comparing it to the area we can calculate A_{eff}/A by simply squaring the radius. The estimated value of C_c comes out to

be 0.6084, which is very close to the theoretical value. The estimated value of the effective area (A_{eff}) also corresponds to the analytical analysis performed by Schmidt et al. [70] and given by the Equation 4.4.

$$A_{eff} = \frac{2C_c^2(p_1 - p_2)}{2C_c p_1 - p_2 + (1 - 2C_c)p_v} A \quad 4.4$$

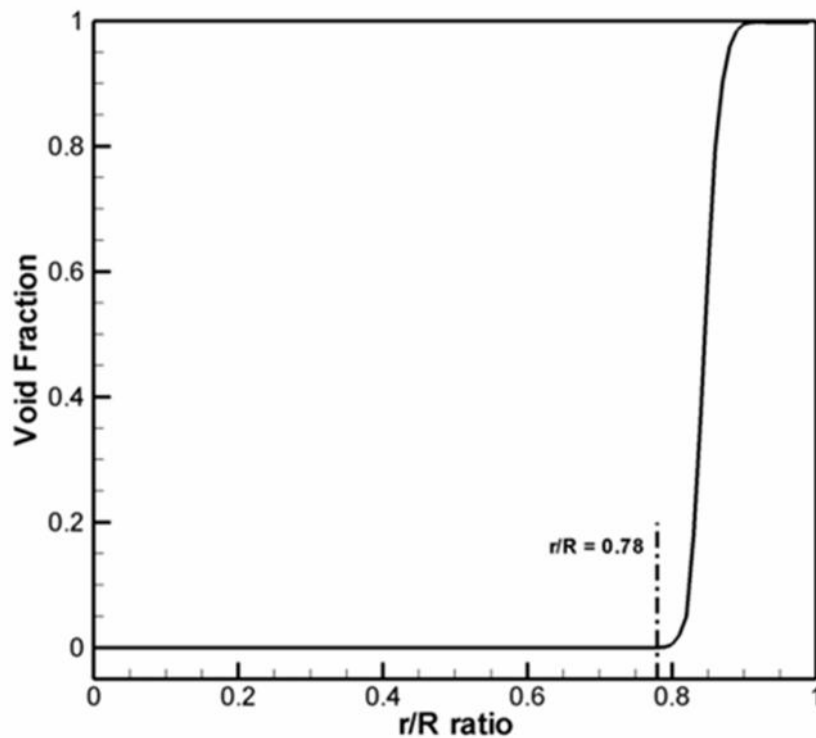


Figure 4-23 Void fraction vs. radial distance at $K=1.1$ for the axisymmetric nozzle with Minmod convective scheme and $k-$ turbulence model at $x=50 \mu\text{m}$.

Winklhofer experiments

The next step to validate the model is simulating the flow in an experimental throttle. These experiments were performed by Winklhofer et al [3,76] to study the flow and the cavitation in a transparent, quasi 2-dimensional throttle at a 10 MPa inlet pressure with varying the outlet pressure. Though, these experiments were performed

at lower injection conditions than real fuel injectors, they provided useful information in terms of mass flow rates and velocity distributions for validating numerical results. They also measured the vapor field distribution and the pressure field distribution inside the nozzle, where the former is measured directly by a CCD camera and for the latter a Mach Zehnder interferometer arrangement is used. They used diesel fuel for their experiments. To match the test conditions, diesel properties at 313K are used for the simulation [53,83]. The Table 4.3 represents the properties used for this simulation.

Table 4-3 Properties of diesel used for the simulations.

\mathcal{E}_g	$6.53 \times 10^{-7} \text{ s}^2/\text{m}^2$	p_l^{sat}	113499 Pa
\mathcal{E}_l	$6.1 \times 10^{-7} \text{ s}^2/\text{m}^2$	\sim_g	$5.953 \times 10^{-6} \text{ Pa-s}$
\dots_g	0.35 kg/m^3	\sim_l	$2.372 \times 10^{-3} \text{ Pa-s}$
\dots_l	818 kg/m^3	N	11.1
p_v	5400 Pa		1.05

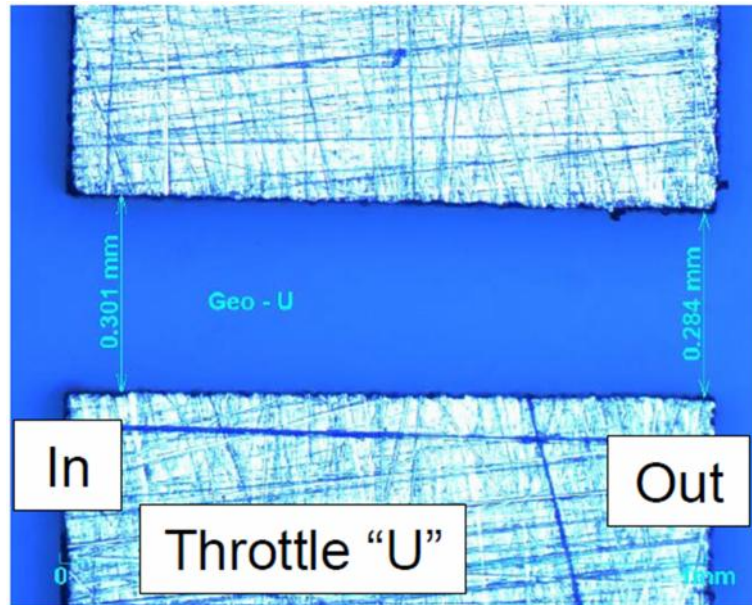


Figure 4-24 Experimental Geometry from Winklhofer et al. [55]

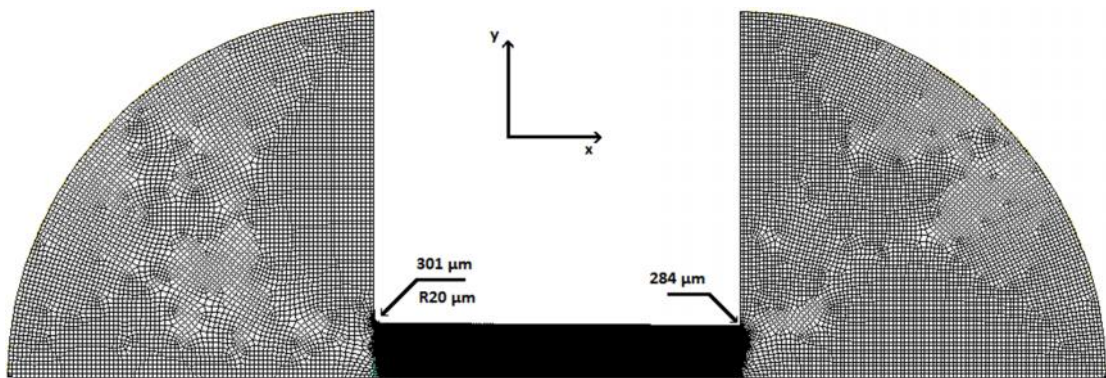


Figure 4-25 The meshed geometry with 76000 quad cells.

In this study, the flow is simulated in a 2D domain. The mesh geometry is shown in the Figure 4-25 with 76000 hexahedral cells in the XY plane and was assumed one cell thick in the Z direction. It consists of 75 cells across the radial direction of the nozzle, which is visible as a dense region in the Figure 4-25. The nozzle is simulated with 10 MPa injection pressure and the downstream pressure was varied from 1.5 MPa to 4.5 MPa. A standard k- turbulence model is used for all the cases. The convective terms in the governing equation are discretized using the

Minmod (TVD) limiter. For gradient and interpolation terms, a second-order central scheme is used. The mass flow rates obtained from the simulation are plotted in the Figure 4-26 along with the experimental observations. The numerical results obtained from the simulation are in very close agreement with the experimental results. In the cavitation region, the deviation is less than 1% whereas in the non-cavitation region the maximum deviation is 4.4% from the experimental mass flow rates. The influence of pressure difference with cavitation is also quite visible in the plot where the critical cavitation incidence closely follows with the experimental results. The experimentalist observed the critical cavitation pressure at 7 MPa differential pressure, which is accurately observed in the simulations.

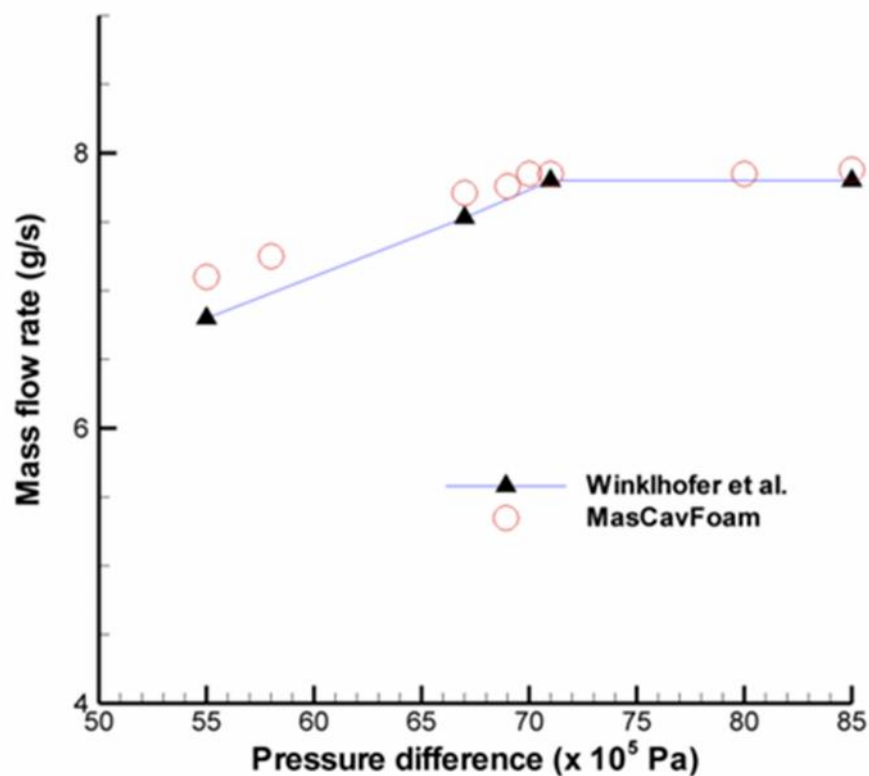


Figure 4-26 Comparison of numerical mass flow rate with experiments

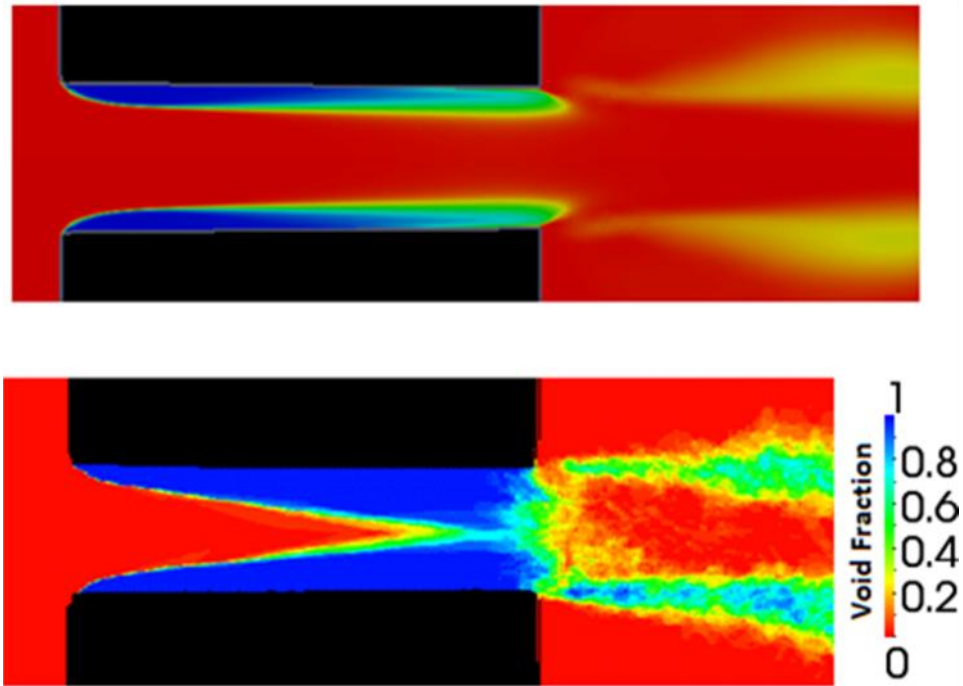


Figure 4-27 Comparison of vapor generation at 8.5 MPa

The void fraction contour obtained from the simulation is compared with the cavitation probability distribution obtained from the experiments and shown in the Figure 4-27. The vapor prediction is close but experimental measurements have shown a greater amount of vapor. One of the reasons for the lower vapor prediction can be due to the difference in fuel temperature and properties. The properties of diesel used in this study are at 313K as the operating temperature is not mentioned in the experimental investigation. The vapor generation at the critical cavitation pressure is shown in the Figure 4-28. In these cases, the vapor formation is less inside the nozzle, though the length of the cavity is very close to experiments.

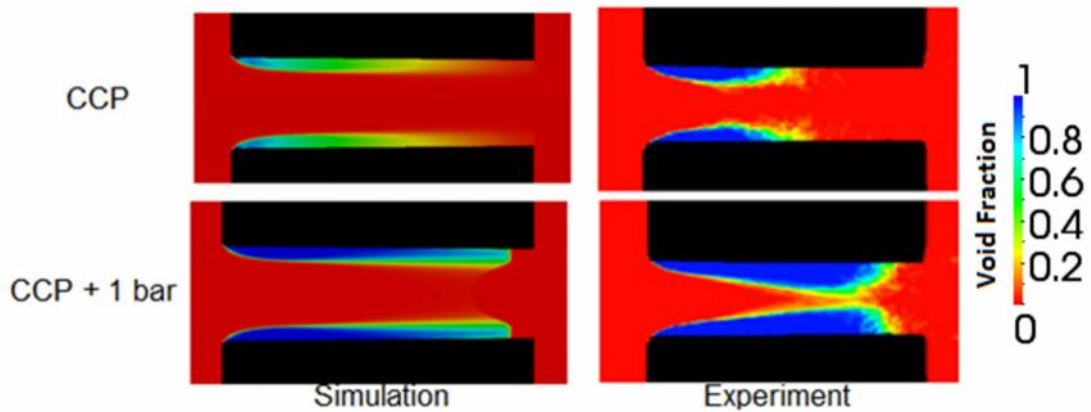


Figure 4-28 Cavitation prediction at the critical cavitation pressure

In the experimental investigation, the velocity profile at a location of 53 μm from the inlet of the nozzle was presented. The experimental data and simulation data for the velocity profile are presented in the Figure 4-29. In these profiles, the near wall velocity is closely simulated, but at the central region the velocity is over-predicted. Overall in this figure, the velocity profile from the simulation closely follows the trend obtained in the experiments. Over-prediction in velocity can be due to differences in fuel properties. An increase or decrease in temperature decreases and increases the viscosity respectively, which also affects the mass flow rate during the non-cavitating or cavitating inception condition. Over-prediction in the velocity can be due to a higher temperature fuel used in the simulation that also explains the higher mass flow rate obtained during the non-cavitating conditions in this simulation.

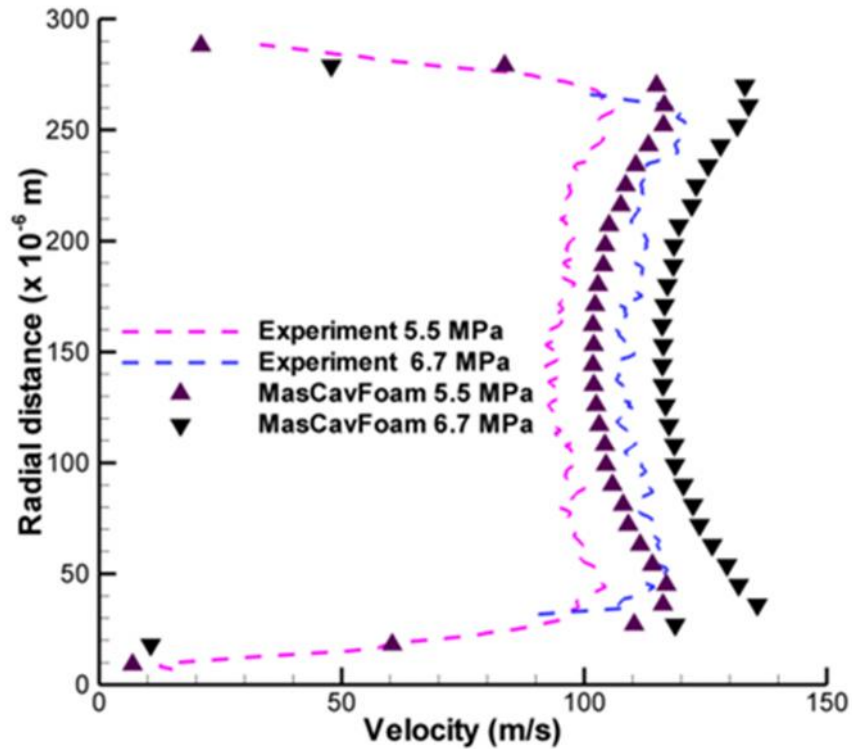


Figure 4-29 Comparison of velocity at 53 um from the nozzle inlet

The Figure 4-30 describes the cavitation inception and fully developed cavitation cases. In the top figure, formation of a low-pressure region near the inlet is visible and limited to the inlet of the nozzle. This region creates a recirculation zone near the wall due to the drop in pressure inside the nozzle. This drop in pressure below the saturated liquid pressure generates a two-phase cloud near the wall and is termed cavitation inception. At this point, the cavitation is limited to the inlet area of the nozzle and the cavity length is minimal. With a further decrease in downstream pressure, the recirculation zone extends to the outlet of the nozzle and creates a cloud of cavitation attached to the wall. In the bottom part of the Figure 4-30, the low pressure region is visible and extends along the nozzle showing a fully developed cavitation region. The pressure contours obtained from the simulations are in good agreement with the experimental images.

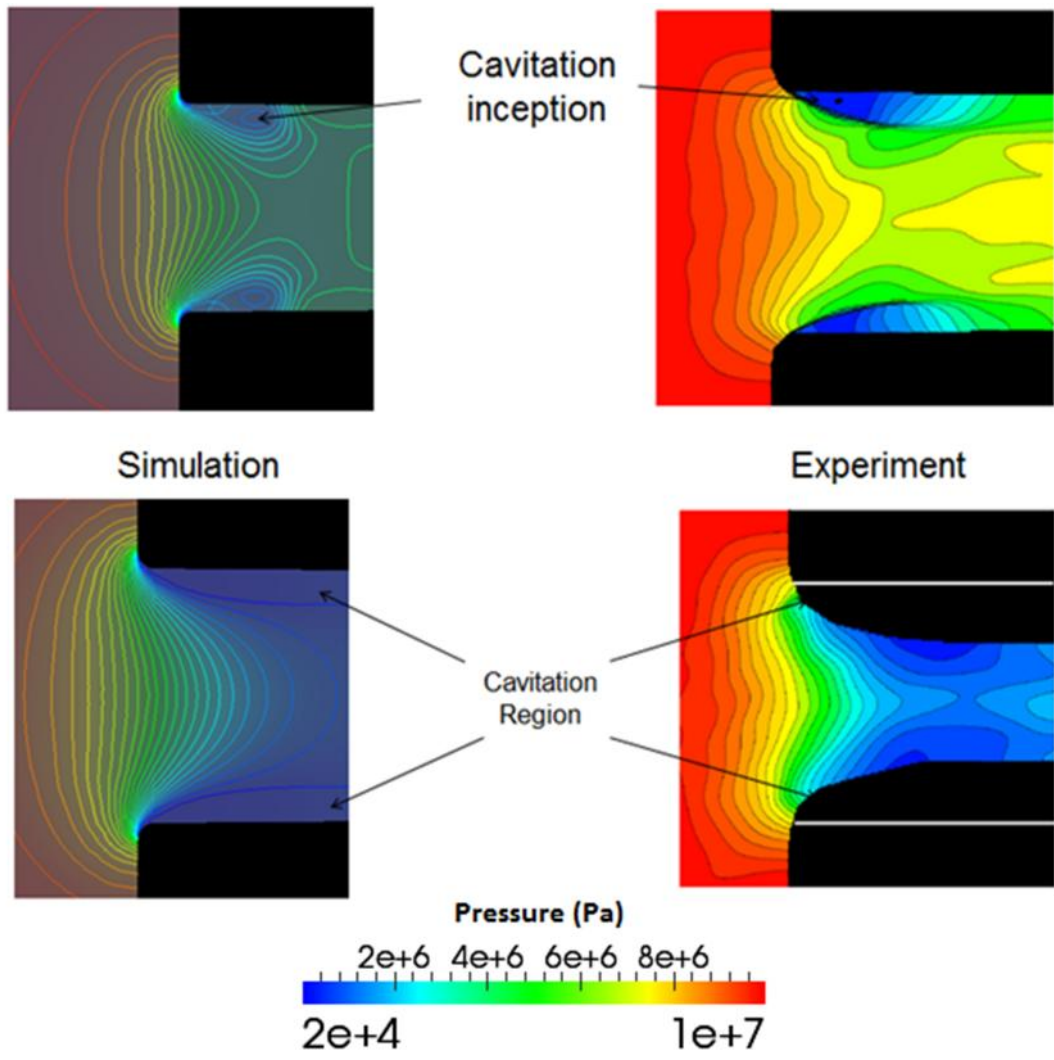


Figure 4-30 Comparison of pressure contour at 3.1 MPa (top) and 4.2 MPa (bottom)

downstream pressure

CHAPTER 5

VALIDATIONS AND RESULTS : ECN INJECTORS

The two-dimensional validations for the solver agree with the theoretical and experimental results. The next step for validating the solver is to simulate flow in three-dimensional injector nozzles. In this work, injectors from Engine Combustion Network (ECN) at 'spray A' and 'spray H' condition are used. The ECN is an open forum for international collaboration among experimental and computational researchers in engine combustion. Typical fuel injectors are very small and accurately measuring them requires lots of resource and precision. The ECN has provided nozzle geometry data for various injector nozzles, and experimental flow data on these nozzles are available for validation.

Spray A Injector simulation

A single hole fuel injector nozzle is selected for the simulation. The Figure 5-2 shows the X-ray tomography image of the injector serial number 210675. From the image, it can be seen that the nozzle is off-centered to the needle axis. The effect of nozzle imperfection on the nature of flow will be an interesting investigation from the simulation. Various nozzle geometries are listed in the Figure 5-3. The inlet diameter is measured around 107 μm and the exit diameter is measured around 89.4 μm from the curve fit shown in the Figure 5-1. The inlet radius is 25 μm and the nozzle length is 1030 μm . The sac and needle dimension are extracted from the images with a precision upto 5 decimals. The nozzle is conical and the conicity factor of the nozzle is around 1.8. The nozzle conicity factor is given by the Equation 5.1.

$$K_f = \left(\frac{D_{inlet} - D_{outlet}}{10} \right) \sim m \quad 5.1$$

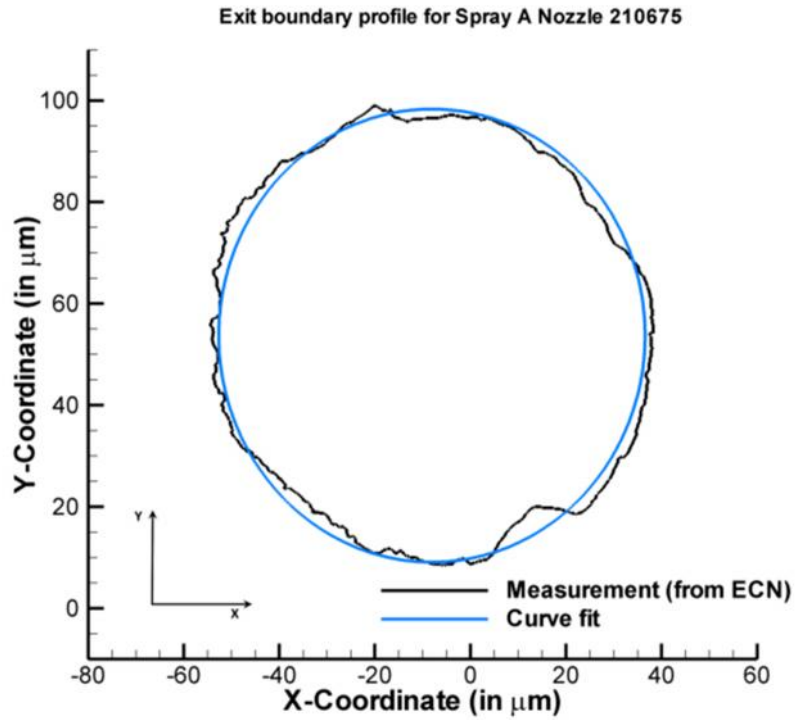


Figure 5-1 Exit profile of the Injector 210675 matched with the measurement from ECN [4]

The exit profile of the nozzle is shown in the Figure 5-1 and to use the exact profile for simulation is extremely difficult. To make things simpler for the simulations, a curve fit to the exit profile is extracted, and an approximate diameter at the exit is calculated (89μm). The nozzle axis is off-center by 56 μm from the needle axis.

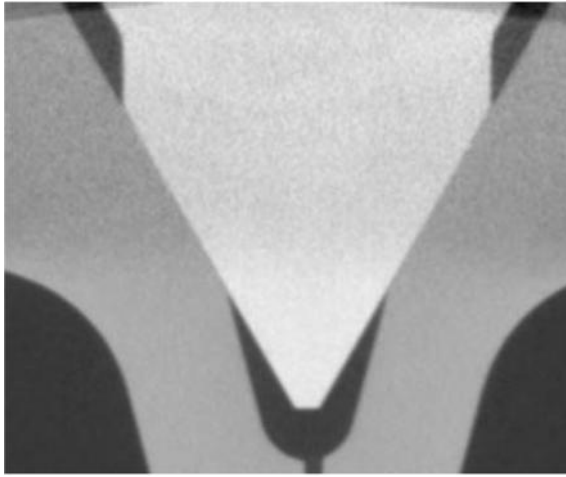


Figure 5-2 X-ray tomography image of Injector 210675 obtained from the ECN website [4].

In this work, the injector needle is static at a distance of 75 μ m from the closed position. The inlet diameter, the outlet diameter and the length of the nozzle were provided by the ECN. Using the inlet diameter of the in the Figure 5-2 and the digitizing software called Engauge, the layout of the sac area is extracted. The precision of this software is upto 6 decimal places and useful in extracting data from images. A CAD model is generated from all the geometry data in SOLIDWORKS, and the geometry is meshed in the ICEM CFD mesh generation software. The sac volume is verified with the CAD model as 0.2 mm³. A blocked mesh strategy is used for generating a hexahedral mesh for the simulation. Hexahedral cells provide better convergence and accuracy than tetrahedral cells. The current solver is used for compressible flow and deals with a high density ratio, where inaccuracy due to mesh non-orthogonality and skewness may lead to instability. To achieve stable and accurate results, a hexahedral mesh is generated for the nozzle. The section view of the CAD model with respective boundary is shown in the

Figure 5-5. The mesh consists of 686K cells. A section view of the inlet of the mesh in the YZ plane is shown in the Figure 5-4. The sectional view of the nozzle in the XY plane is shown in the Figure 5-6.

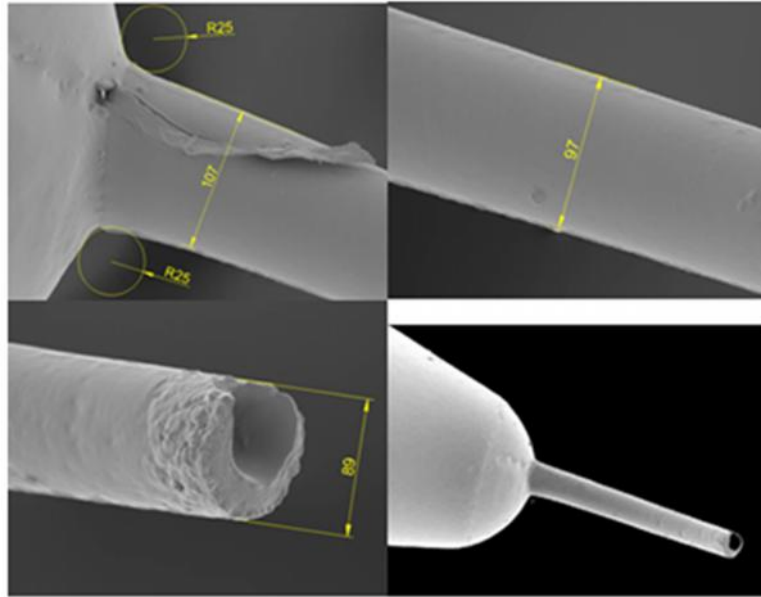


Figure 5-3 Internal shape of the nozzle has been extracted through silicone molds and SEM imaging from Macian et al [77].

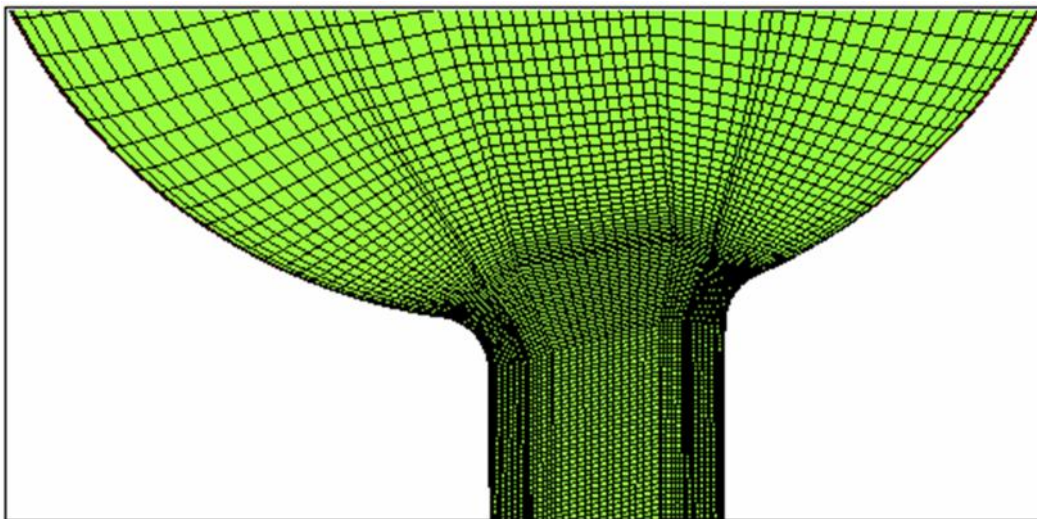


Figure 5-4 Sectional view of the inlet of the nozzle in the YZ plane

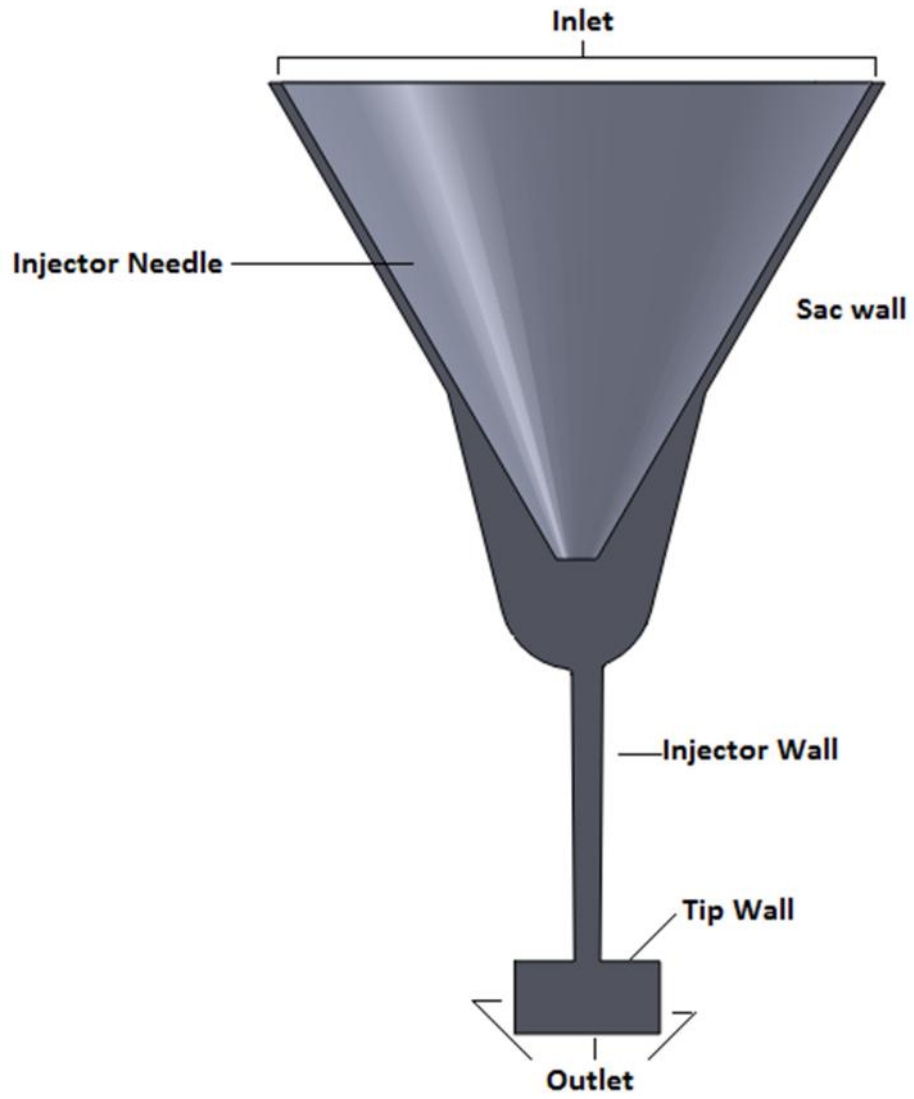


Figure 5-5 Sectional view of the CAD model generated in the YZ Plane.

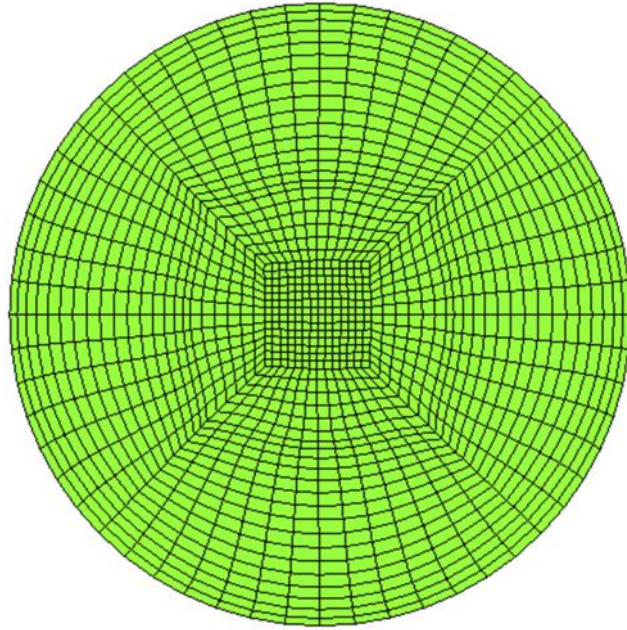


Figure 5-6 Sectional view of the nozzle in XY Plane.

The needle in a fuel injector nozzle is required to simulate the effect due to the off centered axis. Near the injector wall region the cell, width is around 1 micron in radial direction, it increases upto 2 microns in the buffer region and again drops to 1 micron at the center. Total number of cells in the radial direction is around 65, which is around 1.76 microns on average in the radial direction.

The fuel used for the simulation is n-dodecane at 373K temperature [73]. The properties of the fuel used for the simulation are shown in the Table 5-1. The injection pressure at ‘spray A’ condition is specified as 150 MPa and the exit pressure is specified as 6 MPa. A standard k- turbulence model is used for the simulation. The exit boundary condition for pressure used in this simulation is the existing wave transmissive boundary from OpenFOAM. For the velocity, floating boundary condition is used. The simulation is performed for 0.1 ms and the results are characterized into C_d , C_v and C_a as performed by Payri et al [78].

$$C_v = \frac{u_{eff}}{u_{th}} \quad 5.2$$

$$C_a = \frac{A_{eff}}{A_{geo}} \quad 5.3$$

where, u_{eff} and A_{eff} is the effective velocity and area calculated from the Equation 5.4 and 5.5 respectively.

$$u_{eff} = \frac{M_f}{m_f} \quad 5.4$$

$$A_{eff} = \frac{m_f^2}{\dots_f M_f} \quad 5.5$$

where, m_f and M_f represents the mass and momentum flux at the exit.

Table 5-1 Properties of n-dodecane at 363K used for Spray A simulations [73]

\mathbb{E}_g	$5.53 \times 10^{-5} \text{ s}^2/\text{m}^2$	p_l^{sat}	29649 Pa
\mathbb{E}_l	$9.25 \times 10^{-7} \text{ s}^2/\text{m}^2$	\sim_g	$1.207 \times 10^{-4} \text{ Pa-s}$
\dots_g	0.069 kg/m^3	\sim_l	$3.877 \times 10^{-3} \text{ Pa-s}$
\dots_l	697.54 kg/m^3	N	11.1
p_v	1261 Pa		1.05

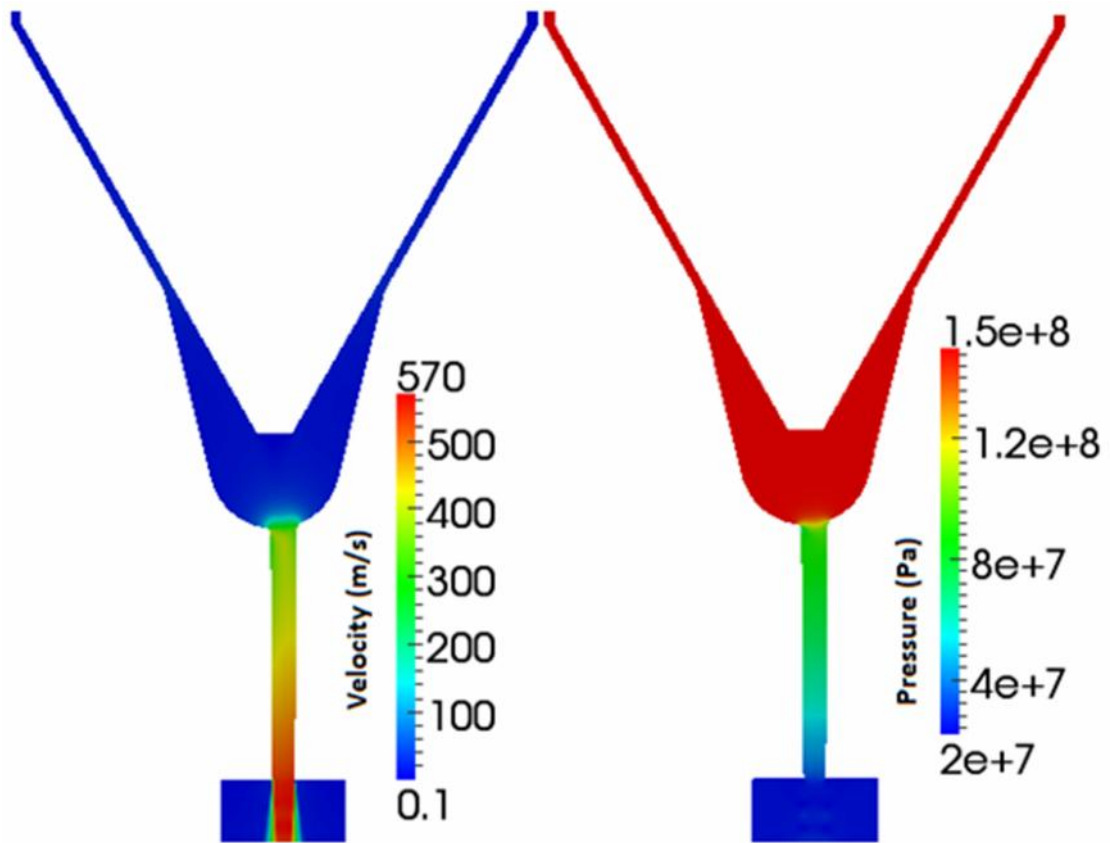


Figure 5-7 Velocity and pressure contour for spray A simulation with Minmod convective scheme and k- turbulence model.

The Figure 5-7 represents the velocity and pressure contours. The injector 21075 has high conicity and it leads to a gradually uniform pressure drop along the nozzle, which prohibits cavitation even at the low cavitation number. Payri et al. [79] have shown how the conicity in the nozzle affects the nature of the flow in injector nozzles. The result obtained from the simulation showed no cavitation inside the nozzle and the pressure drop inside the nozzle is gradual. Another interesting thing to notice in the simulation is the gradual increase in the velocity due to local pressure drop in the radial direction. In a cylindrical nozzle, there is acceleration at the inlet that increases the velocity and the attained velocity remains the same along the nozzle. In this nozzle, the acceleration is maintained by the uniform pressure gradient

along the injector axis. As the pressure drops gradually along the nozzle, a steady rise in the velocity is observed.

Table 5-2 Comparison of results for Spray A Nozzle 210675

	Experiment	Simulation	% error	Units
Mass flux	2.62	2.56	2.3	g/s
Momentum flux	1.52	1.58	3.9	N
C_d	0.9	0.89	2.2	
C_v	0.92	0.96	4.34	
C_a	0.98	0.93	5	

The results obtained from the simulation are tabulated with the experimental result from Payri et al. [80] in the Table 5-2. The mass flux and momentum flux are obtained at the exit of the nozzle. The result shows around 2.3% and 3.9% error in mass and momentum result respectively. The discharge coefficient obtained is around 0.89, which is close to the experimental discharge. Also, the area coefficient is very close to the experiments. The velocity coefficient error is around 4% and due to the difference in momentum flux between experiments and simulation. This model usually yields errors around 2-3% for non-cavitating case and the larger differences in mass and momentum can be due to the surface roughness and the irregular nozzle geometry. The cavitation number of the simulation, defined by the Equation 2.1, is very close to unity and the flow was expected to cavitate at this regime. However, due to a high conicity in the nozzle, the pressure inside the nozzle falls gradually instead of a sudden fall as observed in the two-dimensional injectors.

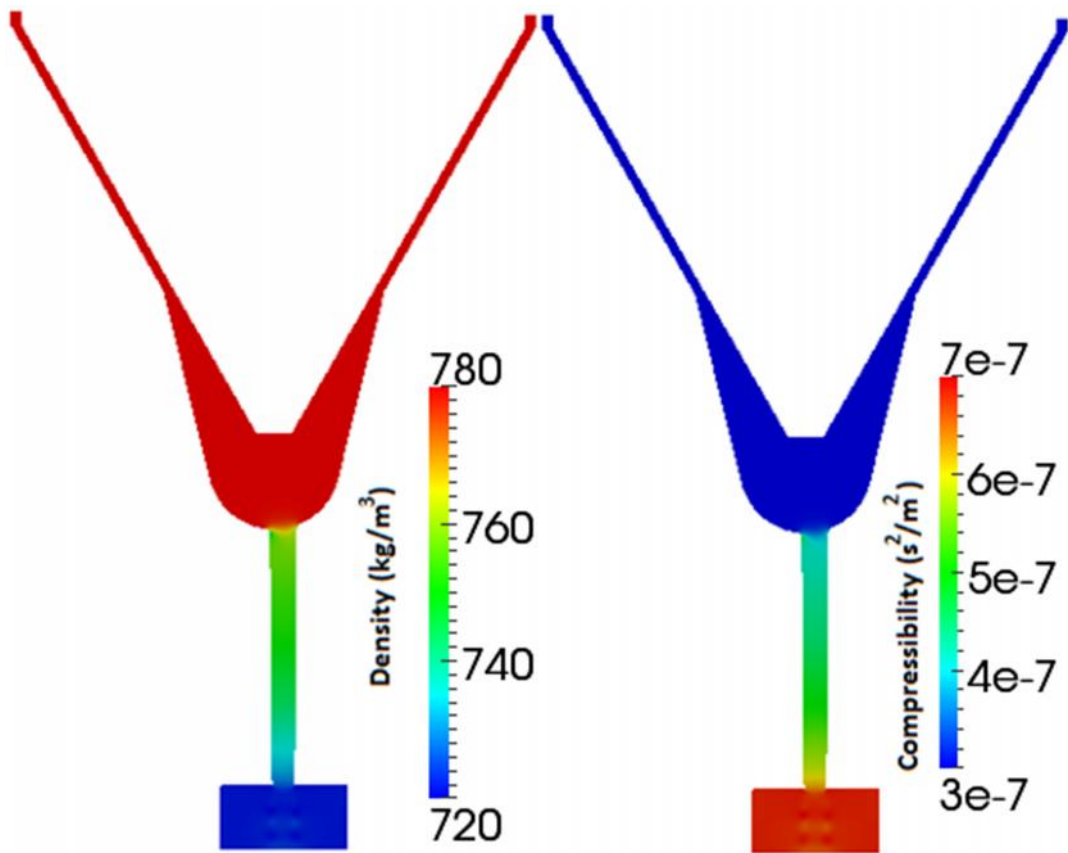


Figure 5-8 Density and compressibility contours at spray A condition with Minmod convective scheme and k- turbulence model.

The Figure 5-8 represents the density and the compressibility variation inside the nozzle. The solver is modeled with variable compressibility for pure phase flows, which is displayed in the compressibility contour. Outgoing compressible waves are also visible at the exit of the nozzle. The Minmod TVD scheme is used for the convective terms and able to capture the compressible waves in three-dimensional simulations.

Spray H Injector simulation

The 'Spray H' condition was initially set up as 'baseline n-heptane' cases. The Figure 5-9 shows an x-ray image of the nozzle over a graph plot showing the dimensions of the nozzle. This nozzle is also conical but the conicity of this nozzle is around 0.5, which is very small compared to the spray A nozzle.

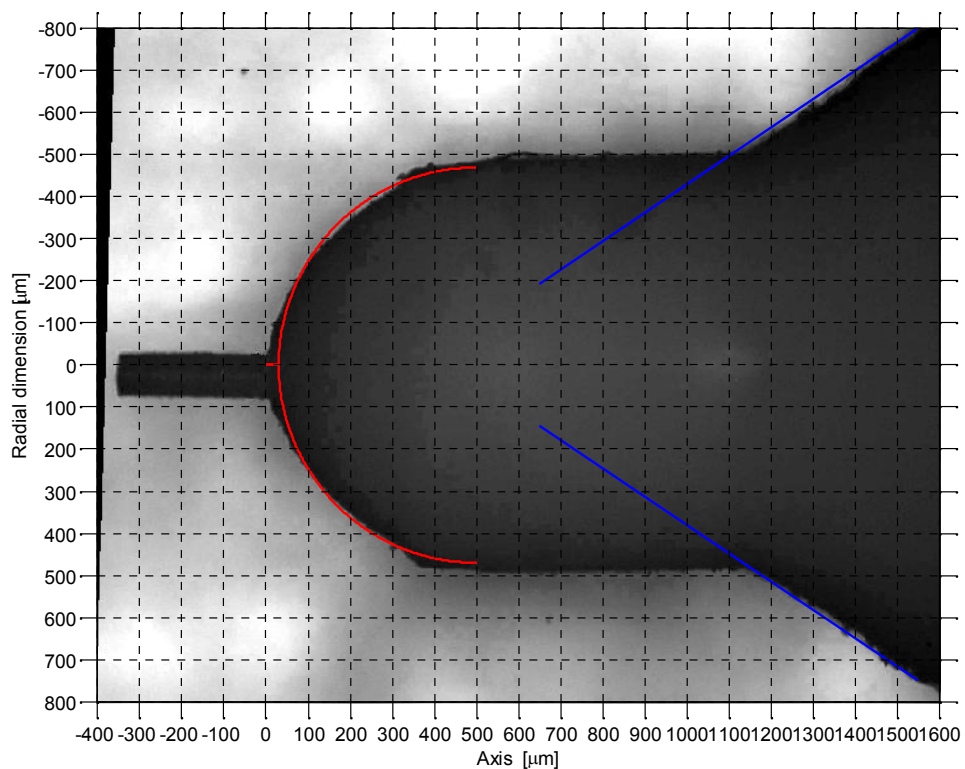


Figure 5-9 Geometry of the nozzle for spray H case from ECN Website [81]

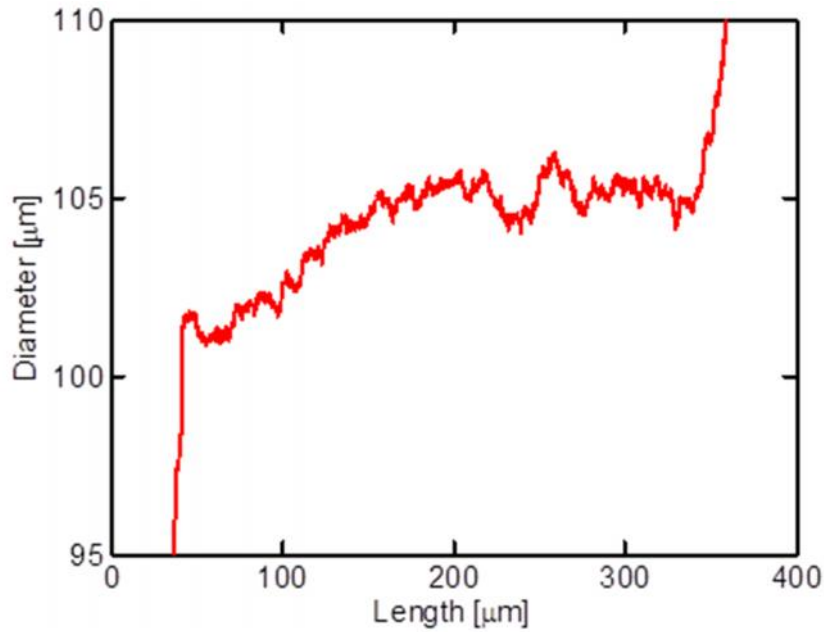


Figure 5-10 Variation of diameter along the length of the nozzle shown by Pickett et al [81].

The inlet diameter of this nozzle is 105 μm and the outlet diameter is around 100 μm . The variation of the diameter along the nozzle is non-linear as shown in the Figure 5-10. The length of the nozzle is around 350 μm (i.e. L/D almost equals to 3.5). The dimensions of the sac are extracted from the Figure 5-9. The sac-volume for this injector is 0.5 mm^3 . The outline of this geometry is simple and generated in Gambit. The geometry is imported into ICEM CFD mesh generation software from Gambit in parasolid format. An outline of the nozzle is shown in the Figure 5-11. A blocked mesh strategy is used for generating a hexahedral mesh for the simulation. This nozzle is expected to cavitate as it is modeled as hydro ground and the K factor is very small. The operating conditions for the experiments are also in the cavitation flow regime. A hexahedral mesh gives better convergence and accuracy, especially for this nozzle where density ratio is close to 600. The mesh consists of around 0.9 million cells. The near nozzle wall cells in the x-direction are very close to 0.7 μm to

capture the cavitation near the wall. Total number of cells along the diameter of the nozzle is 96. The Figure 5-12 shows the sectional view of the nozzle in the YZ plane. The needle is static in the simulations and at a distance of 100 μm from the closed position.

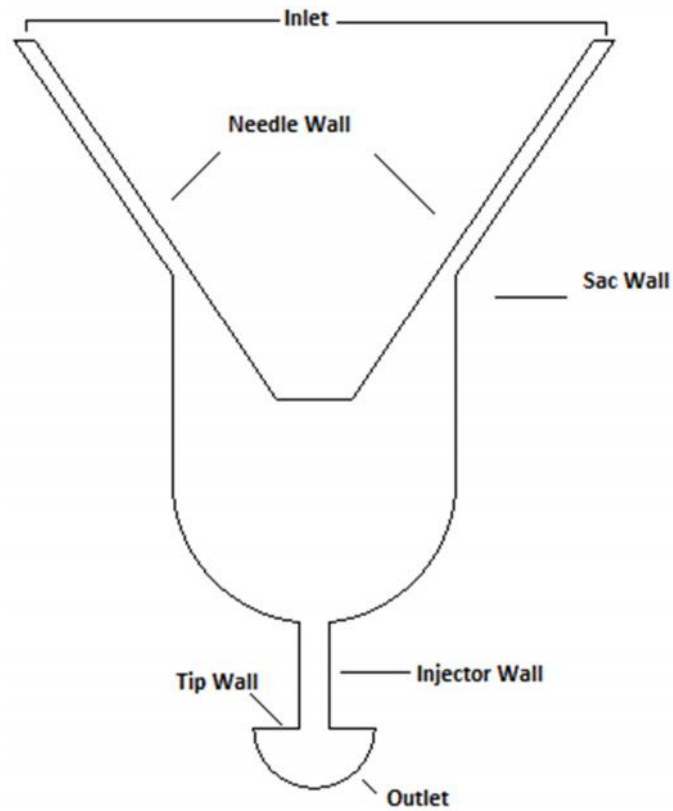


Figure 5-11 Outline of the spray H nozzle with boundaries

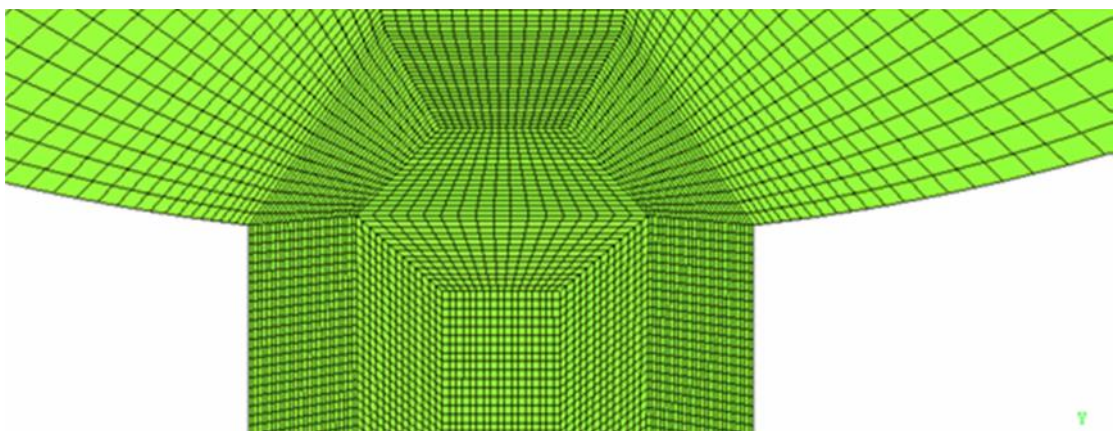


Figure 5-12 Sectional view of the inlet of the nozzle in the YZ plane

The nozzle is simulated using n-heptane fuel at 373K temperature [73]. The inlet pressure is specified as 154.33 MPa and the exit pressure is specified as 4.33 MPa. A Navier-Stokes characteristic based boundary approach, explained in the boundary condition section of the numerical methodology, is used for the exit. The fluid properties of n-heptane are shown in the Table 5-3.

Table 5-3 The fluid properties of n-Heptane at 373K for Spray H simulation [73]

\mathcal{E}_g	$3.428 \times 10^{-5} \text{ s}^2/\text{m}^2$	p_l^{sat}	1.5e6 Pa
\mathcal{E}_l	$1.459 \times 10^{-6} \text{ s}^2/\text{m}^2$	\sim_g	$7.63 \times 10^{-6} \text{ Pa-s}$
\dots_g	3.6150 kg/m^3	\sim_l	$1.923 \times 10^{-4} \text{ Pa-s}$
\dots_l	612.82 kg/m^3	N	11
p_v	105455 Pa		1.05

A standard k- turbulence model is used for the simulations. For the convective terms, a Minmod TVD scheme is used. All other terms are discretized using a second order central scheme. The Figure 5-13 displays the streamlines from the simulations, showing the flow separation near the inlet of the nozzle.

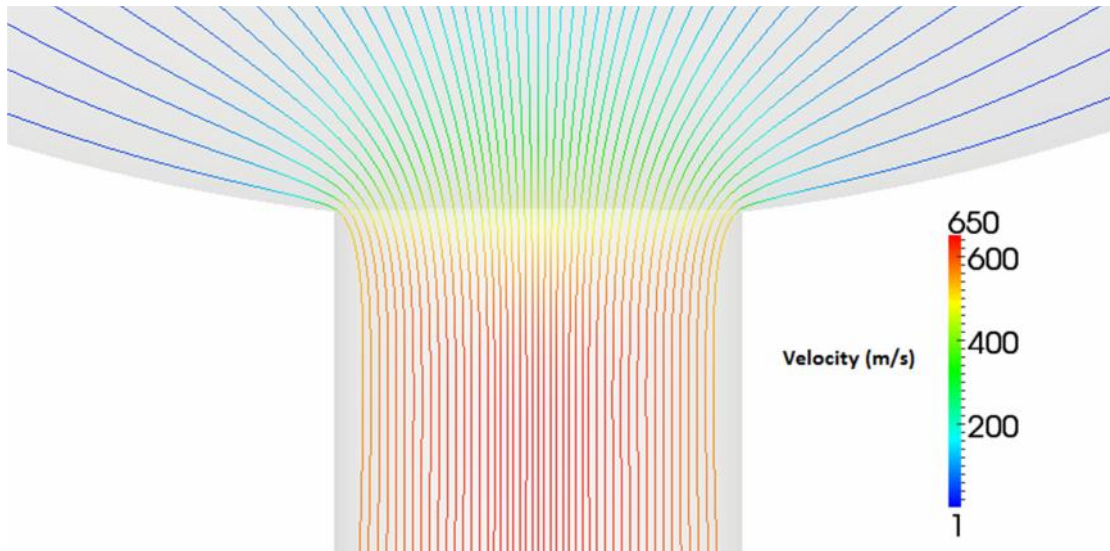


Figure 5-13 Streamlines showing the formation of separation at the inlet.

The simulation is performed for 0.1 ms. The Figure 5-14 displays sectional view of the velocity and density contour of the nozzle. In the nozzle, a shock region is visible near the exit. Inside the nozzle, pressure is below the saturated liquid pressure, whereas at the exit pressure is at 4.33 MPa. Due to this sudden change of the pressure near the exit, the shock is formed. The Figure 5-15 displays the sectional view of the pressure and the compressibility. In the pressure contour, the shock in the path of flow is visible. The cavitation incidence captured by the simulation is similar to the one captured in the two-dimensional nozzles. Though the amount of vapor in the spray H simulation is more as the fluid is set at temperature higher than two-dimensional simulations. The density ratio for this simulation is lower than the density ratio of water at room temperature. Therefore, the fluid in this simulation is more likely to cavitate easily compared to the simulations shown with the two-dimensional sharp nozzles.

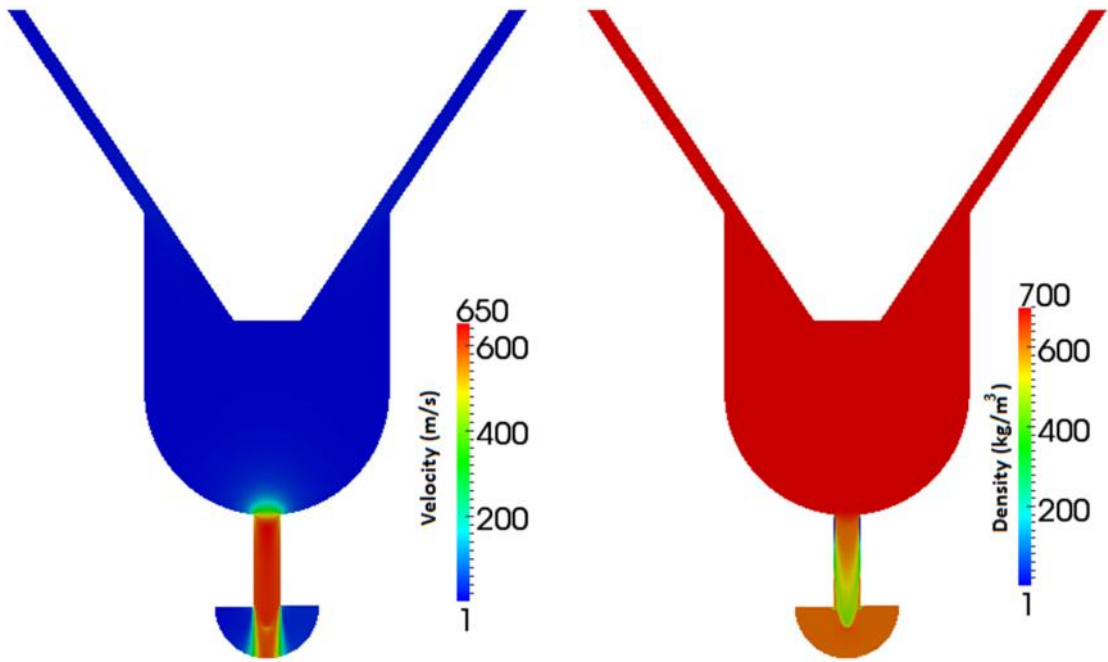


Figure 5-14 Sectional view of the velocity and the density contour for spray H nozzle with Minmod convective scheme and k- turbulence model.

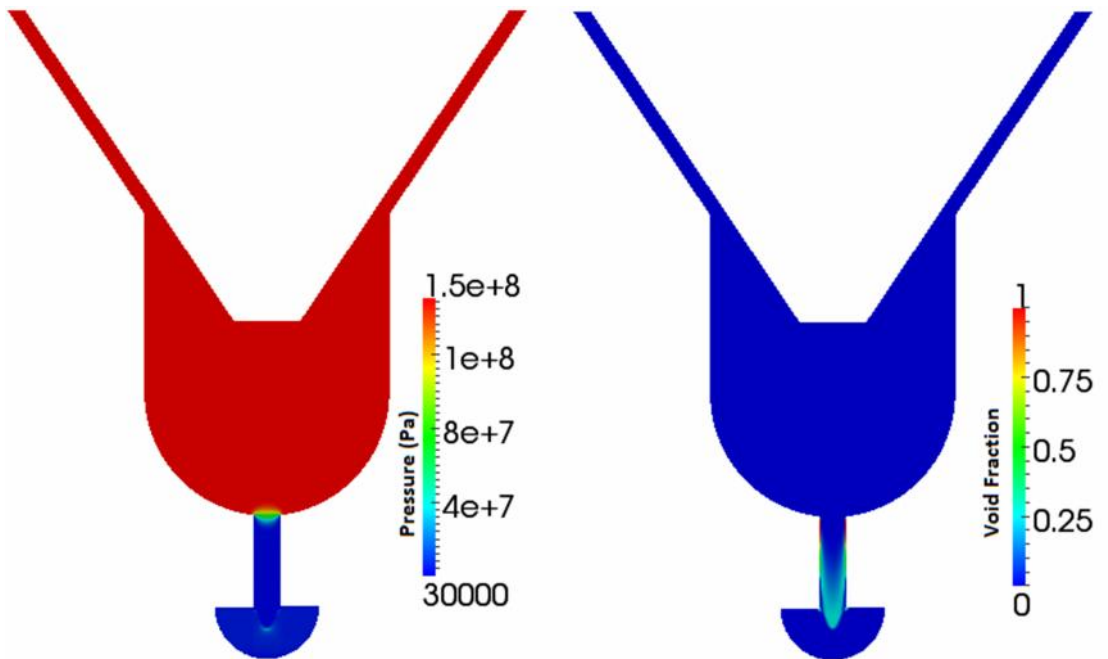


Figure 5-15 The pressure and the compressibility contour for spray H nozzle with Minmod convective scheme and k- turbulence model.

Table 5-4 Mass flow rate and momentum flux comparison for Spray H Nozzle.

	Experiments [4]	Numerical r = 0	Numerical r = 10 μm	Numerical r = 20 μm	
Mass flow	-	2.48	2.8	2.9	g/s
Momentum	-	1.5	1.72	1.783	N
C_d	0.8	0.74	0.84	0.87	
C_a	0.86	0.846	0.94	0.974	

The numerical coefficient of discharge obtained from the three-dimensional simulation is obtained as 0.74 whereas the experimental value is 0.8, which seems to be on the higher side for a sharp nozzle. The cavitation number for this simulation is close to unity and we expected the C_d to be close to 0.62-0.65 range for a perfectly sharp, untapered nozzle. as shown in the Figure 2-5. Since this nozzle is slightly tapered, we can expect the C_d to be slightly above 0.7. The inlet radius is one factor that can increase the C_d significantly and the higher experimental C_d can be due to the presence of inlet curvature. To analyze this nozzle with a slight inlet radius, two-dimensional simulations were performed with 10 μm and 20 μm inlet radii. The results obtained from these simulations showed an increase in the coefficient of discharge with the increase in the inlet radius. The experimental C_d is between the results obtained with the sharp nozzle and the 10 μm inlet radius. The significance of the inlet radius also appears towards the cavitation incidence at the same conditions. The comparison of the density contour in the Figure 5-16 is shown, where the left part is the axisymmetric simulation with an inlet radius of 20 μm and the left side of the figure represents the axisymmetric simulation with an inlet radius of 10 μm . The

difference in cavitation incidence is visible in the figure. Both the simulations are performed with a good mesh resolution. The number of cells in along the radii is around 70 cells for both the cases. The Minmod TVD scheme is used for the convective terms and second order linear scheme is used for the rest of the terms.

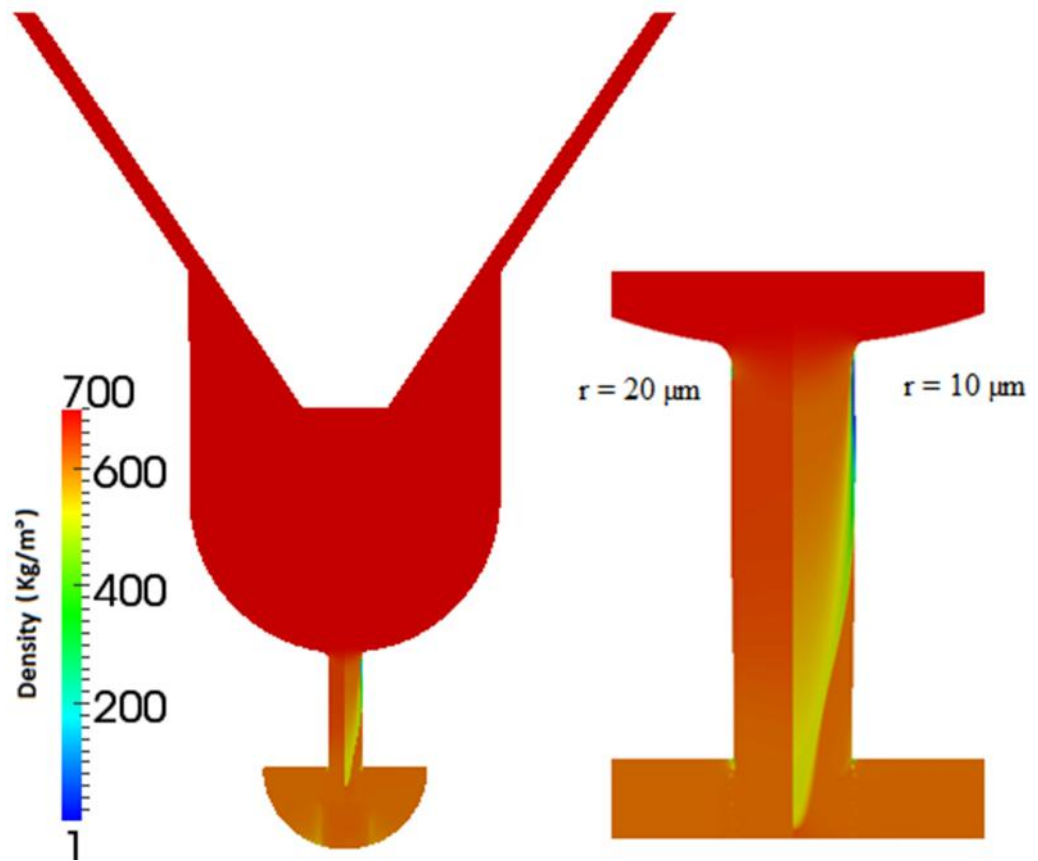


Figure 5-16 Comparison of the density contour with $r = 20 \mu\text{m}$ on left half and $r = 10 \mu\text{m}$ on the right half of the axisymmetric analysis.

CHAPTER 6

CONCLUSIONS

A new solver to simulate cavitation for internal nozzle flows was constructed in OpenFOAM, an object-oriented framework that supports a variety of discretization schemes and polyhedral meshes and is parallelized using MPI. The existing cavitation solver in OpenFOAM works well with a linear compressibility model but is unstable with the more realistic compressibility models given by Wallis [32] and Chung [82] whereas this new solver performs well with the Wallis compressibility model. Besides, the new solver is capable to simulate the non-linearity in compressibility in a single-phase flow, which is not present in the existing solver. The model was validated with several experiments from the open literature.

The flow simulations for the non-cavitating venturi and the sharp nozzle were consistent with the theory. The velocities obtained from the simulations of the venturi were in very close agreement with the velocity obtained from conservation of energy. The mass flow rates obtained from the simulations of the sharp edged nozzles also correspond to the theory given by Nurick [26]. In addition, the analysis on the effective area through the nozzle during cavitation corresponds to the analytical prediction performed by Schmidt et al. [66]. The two-dimensional results displayed a shock near the exit for the submerged simulations and the Minmod TVD scheme does a good job in capturing it consistently for all the cavitation results.

The two-dimensional simulations performed with the nozzle given by Winklhofer et al. were in close agreement with the experiments. The pressure contours and cavitation probability distributions from the numerical results were in close agreement with the experiments. The comparison of the velocity profiles were

slightly over predicted in simulation but the nature of the flow was closely captured. The mass flow rate from the simulations was very close to the experimental values and the incidence pattern of cavitation is accurately captured in the simulations.

The three dimensional analysis using the ECN injectors also showed fidelity to the experiments. The 'spray A' injector at a cavitation number close to unity was expected to cavitate but the presence of high conicity in the nozzle discourages the sudden drop in pressure inside the nozzle. Instead of this, the pressure drops gradually and the velocity was seen rising gradually. The spray H injectors also showed good agreement to the experimental results and the two-dimensional analysis with increasing inlet radius showed the importance of measuring the inlet radius in fuel injector nozzles. The coefficient of discharge can vary with a small change in the inlet radius and measuring them accurately in experiments is important.

The simulations performed in this study obtained grid independent and accurate results. A higher order scheme used in the simulations was able to capture the shock behavior inside the nozzle. The two-dimensional simulations were in close agreement with the theory and the experiments. The three dimensional study of the ECN injectors showed agreement with the experiments. These simulations were close to capturing the behavior inside the real size injectors and can be useful in developing future fuel injectors.

Suggestions for future work

1. The meshes used in these simulations were constructed from hexahedral cells. The hexahedral mesh is difficult to generate for complex domain as compared to tetrahedral mesh but they converge faster and produce more stable results. The

current solver issues with high-density ratio and compressibility and instability due to poor mesh was evident. Improvement in stability with a wide range of meshes can be significant in producing efficient results.

2. The thermo physical properties for a single component fuel at equilibrium are easily available from the NIST online resources but the multicomponent fuels like diesel and gasoline are not present in open literatures. Adding thermo physical database for multicomponent fuels will enable further investigations of effects due to temperature and transport properties in internal nozzle flows.
3. Most of the second order schemes are unstable due to the presence of high gradients and shock in the flow. The Minmod scheme does well with stability and capturing shock but an implementation of ENO/WENO schemes or higher order non-oscillatory schemes in OpenFOAM can be useful addition to the performance of the solver.
4. A needle motion adds significant turbulence to the incoming flow and can produce string cavitation. Implementing needle motion to the existing study could add significant value to the solver and can be used more closely to develop fuel injectors for future diesel engines and GDI injectors.

REFERENCES

- [1] Schmidt, D. P. "Cavitation in diesel fuel injector nozzles" *PhD Thesis, University of Wisconsin Madison*. (1997).
- [2] Schmidt, D. P., C. J. Rutland, and M. L. Corradini. "A fully compressible, two-dimensional model of small, high-speed, cavitating nozzles." *Atomization and Sprays*. vol. 9, issue 3, pp. 255-276. (1999).
- [3] Winklhofer, E., E. Kull, E. Kelz, A. Morozov, "Comprehensive hydraulic and flow field documentation in model throttle experiments under cavitation conditions", ILASS-Europe (2001).
- [4] Engine combustion network, <http://www.sandia.gov/ecn>
- [5] U.S. EPA. "Emission standards and supplemental requirements for 2007 and later model year diesel heavy-duty engines and vehicles." Paper No. 40 CFR, (2005).
- [6] Payri, R., F. J. Salvador, J. Gimeno, and J. De la Morena. "Study of cavitation phenomena based on a technique for visualizing bubbles in a liquid pressurized chamber." *International Journal of Heat and Fluid Flow*. vol. 30, issue 4, pp. 768-777. (2009).
- [7] Baumgarten, C. "Mixture formation in internal combustion engines." *Springer*. (2006).
- [8] Kashiwaya, M., T. Kosuge, K. Nakagawa, and Y. Okamoto. "The effect of atomization of fuel injectors on engine performance." *SAE transactions*. vol. 99, issue 3, pp. 699-705. (1990).
- [9] Montgomery, D. T., M. Chan, C. T. Chang, P. V. Farrell, and R. D. Reitz. "Effect of injector nozzle hole size and number on spray characteristics and the performance of a heavy duty D. I. diesel engine." *SAE paper 962002*. vol. 1205, pp. 1-18. (1996).

- [10] Kato, T., T. Koyama, K. Sasaki, K. Mori, and K. Mori. "Common rail fuel injection system for improvement of engine performance on heavy duty diesel engine." *SAE Paper 980806*, pp. 39-48. (1998).
- [11] Hiroyasu, H. "Spray breakup mechanism from the hole-type nozzle and its applications." *Atomization and Sprays*. vol. 10, issue 3-5, pp. 511. (2000) cited by [84].
- [12] Schmidt, D. P., Rakshit, S., and Neroorkar, K., "Thermal and Inertial Equilibrium in Small, High-Speed, Cavitating Nozzle Simulations," 11th Triennial International Conference on Liquid Atomization and Spray Systems, Vail, Colorado USA, July 2009.
- [13] Bergwerk, W. "Flow pattern in diesel nozzle spray holes." *Proceedings of the Institution of Mechanical Engineers*. vol. 173, pp. 655-660. (1959).
- [14] Bode, J., H. Chaves, F. Obermeier, and T. Schneider. "Influence of cavitation in turbulent nozzle flow on atomization and spray formation of a liquid jet." *Proc. Sprays and Aerosols, ILASS Europe*. (1991).
- [15] Chaves, H., M. Knapp, A. Kubitzek, and F. Obermeier. "High-speed flow measurements within an injection nozzle" *SPIE*. vol. 2052, pp. 265-272. (1993).
- [16] Chaves, H.; Knapp, M.; Kubitzek, A.; Obermeier, F. "Experimental study of cavitation in the nozzle hole of diesel injectors using transparent nozzles." *SAE paper 950290*. vol. 104, issue 3, pp. 645-657. (1995).
- [17] Soteriou, C., R. Andrews, M. Smith, N. Torres, and S. Sankhalpara. "The flow patterns and sprays of variable orifice nozzle geometries for diesel injection." *SAE transactions*. vol. 109, issue 3, pp. 1007-1029. (2000).
- [18] Soteriou, C., R. J. Andrews, and M. Smith. "Direct injection diesel sprays and the effect of cavitation hydraulic flip on atomization." *SAE paper 950080*. vol. 104, issue 3, pp. 128-153. (1995).

- [19] Soteriou, C., R. Andrews, N. Torres, M. Smith, and R. Kunkulagunta. "Through the diesel nozzle hole—a journey of discovery." *ILASS-Europe, Zurich*. (2001).
- [20] Badock, C., R. Wirth, and A. Fath. "Investigation of cavitation in real size diesel injection nozzles." *International Journal of Heat and Fluid Flow*. vol. 20, issue 5, pp. 538-544. (1999).
- [21] Arcoumanis, C., M. Gavaises, H. Flora, and H. Roth. "Visualisation of cavitation in diesel engine injectors." *Mécanique & Industries*. vol. 2, issue 5, pp. 375-381. (2001).
- [22] Arcoumanis, C., H. Roth, and M. Gavaises. "Cavitation initiation, its development and link with flow turbulence in diesel injector nozzles" *SAE paper 2002-01-0214*. (2002).
- [23] Arcoumanis, C., M. Badami, H. Flora, and M. Gavaises. "Cavitation in real-size, multi-hole diesel injector nozzles." *SAE paper 2000-01-1249*. vol. 109, issue 3, pp. 1485-1500. (2000).
- [24] Chaves, H., R. Miranda, and F. Obermeier. "Imaging of cavitation, hollow jets and jet branching at low lift in a real size VCO nozzle" *ILASS-Europe, Zaragoza*. vol. 9, pp. 11-16. (2002).
- [25] Chaves, H., R. Miranda, U. Martin, and F. Obermeier. "Cavitation in a transparent real size VCO injection nozzle" *Proceedings of ICLASS, Sorrento Italy*. (2003).
- [26] Nurick, W. H. "Orifice cavitation and its effect on spray mixing" *Journal of Fluids Engineering*, vol. 98, pp. 681. (1976).
- [27] Lichtarowicz, A., and I. D. Pearce. "Discharge performance of long orifices with cavitating flow" *Proceedings of the 2nd Fluid Power Symposium*, vol. 2, pp. 13-35. (1971).

- [28] Stanley, C., G. Rosengarten, B. Milton, and T. Barber. "Investigation of cavitation in a large-scale transparent nozzle" *FISITA 2008 Student Congress*. (2008).
- [29] Baz, I., J. C. Champoussin, M. Lance, and J. L. Marié. "Investigation of the cavitation in high pressure diesel injection nozzles" *ASME*. (2002).
- [30] Kobayashi, R. "Effect of cavitation on the discharge coefficient of standard flow nozzles" *ASME Journal of Basic Engineering*. vol. 89, issue 3, pp. 677-685. (1967).
- [31] Hiroyasu, H., M. Arai, and M. Shimizu. "Break-up length of a liquid jet and internal flow in a nozzle" *ICLASS-91, USA*. pp. 275-282. (1991).
- [32] Sou, A., M. I. Maulana, K. Isozaki, S. Hosokawa, and A. Tomiyama. "Effects of nozzle geometry on cavitation in nozzles of pressure atomizers" *Journal of Fluid Science and Technology*. vol. 3, issue 5, pp. 622-632. (2008).
- [33] Lee, C. S., and H. K. Suh. "Effect of cavitation in nozzle orifice on the diesel fuel atomization characteristics" *International Journal of Heat and Fluid Flow*. vol. 29, issue 4, pp. 1001-1009. (2008).
- [34] Kim, S. R., K. W. Ku, J. G. Hong, and C. W. Lee. "An experimental investigation of discharge coefficient and cavitation length in the elliptical nozzles" *ILASS-Europe, Czech Republic*. (2010).
- [35] Yokota, M., Y. Ito, and T. Shinohe. "High speed photographic observations of cavitation arising in a high speed oil flow through a very small orifice" *Japan Society of Mechanical Engineers. B series*. vol. 55, issue 515, pp. 1817-1822. (1989).
- [36] Yokota, M., Y. Ito, and H. Aoki. "Cavitation characteristic of multi-hole diesel fuel nozzles in high speed oil flows" *Japan Society of Mechanical Engineers. B series*. vol. 57, issue 539, pp. 2428-2433. (1991).

- [37] Tamaki, N., M. Shimizu, K. Nishida, and H. Hiroyasu. "Effects of cavitation and internal flow on atomization of a liquid jet" *Atomization and Sprays*. vol. 8, issue 2, pp. 179-198. (1998).
- [38] Gelalles, A. G. "Coefficients of discharge of fuel injection nozzles for compression-ignition engines" *NACA report*. (1931).
- [39] Kubota, A., H. Kato, and H. Yamaguchi. "Finite difference analysis of unsteady cavitation on a two-dimensional hydrofoil" *Proc. of the 5th International Conference. on Numerical Ship Hydrodynamics, Hiroshima*. pp. 667-683. (1989).
- [40] Chen, Y., and S. D. Heister. "Modeling hydrodynamic non-equilibrium in bubbly and cavitating flows" *Journal of Fluids Engineering*, vol. 118, issue 1, (1995).
- [41] Gavaises, M., and C. Arcoumanis. "Linking nozzle flow with spray characteristics in a diesel fuel injection system" *Atomization and Sprays*. vol. 8, issue 3, pp. 307-348. (1998).
- [42] Gavaises, M., E. Giannadakis, and C. Arcoumanis. "Modelling of cavitation in diesel injector nozzles" *Journal of Fluid Mechanics*. vol. 616, issue 1, pp. 153-193. (2008).
- [43] Alajbegovic, A., and H. A. Grogger. "Calculation of the cavitating flow in venturi geometries using two fluid model" *ASME paper FEDSM*. pp. 98. (1998).
- [44] Singhal, A. K., M. M. Athavale, H. Li, and Y. Jiang. "Mathematical basis and validation of the full cavitation model." *Journal of Fluids Engineering*. 124, 617. (2002).
- [45] Chen, Y., and S. D. Heister. "Two-phase modeling of cavitating flows" *Computers & Fluids*. vol. 24, issue 7, pp. 799-809. (1995).
- [46] Yuan, W., J. Sauer, and G. H. Schnerr. "Modeling and computation of unsteady cavitation flows in injection nozzles." *Mécanique & Industries*. 2, 5, 383-394. (2001).

- [47] Avva, R. K., A. K. Singhal, and D. H. Gibson. "An enthalpy based model of cavitation"*ASME-PUBLICATIONS-FED*. vol. 226, pp. 63-70. (1995).
- [48] Delannoy, Y., and J. L. Kueny. "Two phase flow approach in unsteady cavitation modelling"*Cavitation and Multiphase Flow Forum, ASME-FED*. vol. 98, pp. 153-158. (1990).
- [49] Dumont, N., O. Simonin, and C. Habchi. "Numerical simulation of cavitating flows in diesel injectors by a homogeneous equilibrium modeling approach"*4th Int. Symposium on Cavitation: CAV2001*. (2001).
- [50] Habchi, C., N. Dumont, and O. Simonin. "CAVIF: A 3D code for the modeling of cavitating flows in diesel injectors", *ICLASS Europe*. (2003).
- [51] Lee, W. G., and R. D. Reitz. "A numerical investigation of transient flow and cavitation within minisac and valve-covered orifice diesel injector nozzles."*Journal of Engineering for Gas Turbines and Power*. 132, (2010).
- [52] Kärrholm, F. P., H. Weller, and N. Nordin. "Modelling injector flow including cavitation effects for diesel applications.", ASME/JSME 2007 5th Joint Fluids Engineering Conference. (2007).
- [53] Kärrholm, F. P. "*Numerical modelling of diesel spray injection, turbulence interaction and combustion*", *PhD Thesis*, Chalmers Univ. of Technology (2008).
- [54] Catania A.E., Ferrari A., Manno M., Spessa E. Thermal effect simulation in high-pressure injection system transient flows. SAE paper 2004-01-0532, 2004.
- [55] Neroorkar, K., B. Shields, and D. Schmidt. "Cavitation as rapid flash boiling."*ILASS-americas 23rd Annual Conference on Liquid Atomization and Spray Systems, Ventura, CA*. (2011).
- [56] Wallis, G. B. "*One-dimensional two-phase flow*" McGraw-Hill New York (1969).
- [57] XIE WENFENG "A numerical simulation of underwater shock-cavitation-structure interaction", *PhD Thesis*, National University of Singapore (2005).

- [58] Shapiro, A. H. "Compressible Fluid Flow" New York, Ronald Press Co (1953).
- [59] H. Weller, G. Tabor, H. Jasak, and C. Fureby, "A tensorial approach to computational continuum mechanics using object-oriented techniques," *Computers in Physics*, vol. 12, no. 6, pp. 620–631, 1998.
- [60] Ferziger, J. H., and M. Peric. "*Computational methods for fluid dynamics*.". 3rd edition ed.Springer, Berlin (2002).
- [61] OpenCFD. 2009. *OpenFOAM - the open source CFD toolbox - programmer's guide*. 1.6 edition ed.OpenCFD ltd., United Kingdom.
- [62] Jasak, H. "Error analysis and estimation for the finite volume method with applications to fluid flows", *PhD Thesis, Imperial College, London*. (1996).
- [63] Poinso TJ, Lele SK. 1992. Boundary conditions for direct simulations of compressible viscous flows. *J. Comput. Phys.* 101:104-139.
- [64] Polifke, W., Wall, C. & Moin, P. 2006 Partially reflecting and non-reacting boundary conditions for simulation of compressible viscous flow. *J. of Comp. Phys.* 213 (1),437{449.
- [65] Tamaki, N., M. Shimizu, and H. Hiroyasu. "Enhancement of the atomization of a liquid jet by cavitation in a nozzle hole"*Atomization and Sprays*. vol. 11, issue 2, pp. 125-138. (2001).
- [66] Daikoku, M., H. Furudate, H. Noda, and T. Inamura. "Effect of cavitation in the two-dimensional nozzle on liquid breakup process"*Proc.ICLASS 2003*. vol. 17, issue 6, (2003).
- [67] Tamaki, N., M. Shimizu, and H. Hiroyasu. "Atomization of high-viscous liquid jet by cavitation in the nozzle hole" *Transactions of the Japan Society of Mechanical Engineers, series B*. vol. 71, issue 702, pp. 632-640. (2005).
- [68] Park, S. H., H. K. Suh, and C. S. Lee. "Effect of cavitating flow on the flow and fuel atomization characteristics of biodiesel and diesel fuels"*Energy & Fuels*. vol. 22, issue 1, pp. 605-613. (2007).

- [69] Sou, A., S. Hosokawa, and A. Tomiyama. "Effects of cavitation in a nozzle on liquid jet atomization"*International Journal of Heat and Mass Transfer*. vol. 50, 3575-3582. (2007).
- [70] Sou, A., M. I. Maulana, S. Hosokawa, and A. Tomiyama. "Ligament formation induced by cavitation in a cylindrical nozzle"*Journal of Fluid Science and Technology*. vol. 3, issue 5, pp. 633-644. (2008).
- [71] Suh, H. K., S. H. Park, and C. S. Lee. "Experimental investigation of nozzle cavitating flow characteristics for diesel and biodiesel fuels"*International Journal of Automotive Technology*. vol. 9, issue 2, pp. 217-224. (2008).
- [72] Sou, A., S. Hosokawa, and A. Tomiyama. "Cavitation in nozzles of plain orifice atomizers with various length-to-diameter ratios"*Atomization and Sprays*. vol. 20, issue 6, (2010).
- [73] NIST fluid properties, <http://webbook.nist.gov/chemistry/fluid/>
- [74] Von Mises, R. "Berechnung von ausfluss und ueberfallzahlen"*Zeitschrift des vereins deutscher ingenieure*. 61, (1917).
- [75] Schmidt, D. P., and M. L. Corradini. "Analytical prediction of the exit flow of cavitating orifices"*Atomization and Sprays*. 7, 6, 603-616. (1997).
- [76] Winklhofer, E., E. Kull, E. Kelz, A. Morozov, "Comprehensive hydraulic and flow field documentation in model throttle experiments under cavitation conditions", ILASS-Europe (2001).
- [77] V. Macian, V. Bermúdez, R. Payri, J. Gimeno, New technique for the determination of the internal geometry of Diesel nozzle with the use of the silicone methodology, *Experimental Techniques*, Vol 27 (2), pp. 39-43, 2003.
- [78] Payri R, Garcí'a JM, Salvador FJ, Gimeno J. "Using spray momentum flux measurements to understand the influence of Diesel nozzle geometry on spray characteristics" *Fuel* 84:551–61(2005).

- [79] Payri F, Bermudez V, Payri R, Salvador FJ "The influence of cavitation on the internal flow and the spray characteristics in diesel injection nozzles". *Fuel* 83:419–431 (2004).
- [80] Payri, R., Manin, J., " ECN Workshop: Injector's hydraulic charecterization" <http://www.sandia.gov/ecn/workshop/ECN1/HydraulicCharacterization.pdf>
- [81] Pickett, L., " Silicone mold analysis of internal nozzle geometry for baseline n-heptane "Spray H" condition" <http://www.sandia.gov/ecn/cvdata/assets/datafiles/nozgeom/sacVolumeDimensions.pdf>
- [82] Chung, M.S., Park, S.B., and Lee, H.K., "Sound speed criterion for two-phase critical ow". *Journal of Sound and Vibration*, 276,pp. 13-26 (2004).
- [83] Kolev, N.I., "Multiphase Flow Dynamics 4: Turbulence, Gas Adsorption and Release, Diesel Fuel Properties" Springer; 2nd Edition, (2011).
- [84] Martynov, S. "Numerical simulation of the cavitation process in diesel fuel injectors", PhD Thesis *University of Brighton, England*. (2005).